UNIVERSITY OF CALIFORNIA, SAN DIEGO

Identifying Two Steps in the Internal Wave Energy Cascade

A dissertation submitted in partial satisfaction of the
requirements for the degree
Doctor of Philosophy

in

Oceanography

by

Oliver Ming-Teh Sun

Committee in charge:

Professor Robert Pinkel, Chair
Professor Peter J. S. Franks
Professor Jennifer A. MacKinnon
Professor Daniel L. Rudnick
Professor Sutanu Sarkar
Professor William R. Young

2010

The dissertation of Oliver Ming-Teh Sun is approved, and it is acceptable in quality and form for publication on microfilm and electronically:

_____

_____

_____

_____

_____

_____
Chair

University of California, San Diego

2010

DEDICATION

To my parents, Wen-Yih and Rueen-Yuh, and to my loving wife, Sophia.

TABLE OF CONTENTS

LIST OF FIGURES

ACKNOWLEDGEMENTS

Thanks to everyone on the OPG team: Mike Goldin, Tony Aja, Mai Bui, Tyler Hugher, Eric Slater, and to fellow former and current students: Luc Rainville, Jon Pompa, San Nguyen.

VITA

1997	B. S. in Mathematics, Purdue University.
2004	M. A. in Applied Mathematics, Indiana University
2010	Ph. D. in Oceanography, University of California, San Diego

ABSTRACT OF THE DISSERTATION

Identifying Two Steps in the Internal Wave Energy Cascade

by

Oliver Ming-Teh Sun

Doctor of Philosophy in Oceanography

University of California, San Diego, 2010

Professor Robert Pinkel, Chair

In addition to their own convective breaking, the energetic baroclinic tides at a generation site stimulate the weaker non-linear interactions that might comprise the more-typical open ocean energy cascade. Observations of two classes of nonlinear interactions are presented. The first transfers energy from the semidiurnal tide to near-diurnal subharmonics. The second transfers energy from low-frequency, high-shear waves to high frequencies.

Evidence is shown for wave-wave interactions between the low-mode, semidiurnal tide and high-mode, near-inertial motions. Profiles of velocity and density were collected aboard the Research Platform *FLIP*, at two sites during the Hawaii Ocean Mixing Experiment (HOME). In HOME Nearfield, significant bicoherences are observed between the dominant low-mode semidiurnal tide and opposing pairs

of near-diurnal waves of vertical scale $\approx$ 100 m. Growth rates of diurnal waves during each fortnightly cycle agree with theoretical predictions for the Parametric Subharmonic Instability (PSI) mechanism. At the Farfield location, 430 km from the generation site, near-diurnal waves are also observed but are not significantly bicoherent with the semidiurnal tide.

Triple correlations between low frequency vertical shears and high frequency Reynolds stresses, $-\langle u_i w\, dU_i/dz\rangle$, are used at both HOME sites to estimate energy transfers from low frequencies, including both wind-generated motions and PSI subharmonics, to high frequencies. Energy bispectra show significant energy transfers to pairs of waves with nearly identical frequency. However, wavenumber resonances do not fit either the Induced Diffusion (ID) or eikonal models of interaction.

Peak transfer rates in the Nearfield are of order 1×10^{-7} W kg^{-1}, while transfer rates in the Farfield are 3–4$\times$ smaller. Nearfield energy transfers are larger than local turbulence dissipation, but fall within an order of magnitude. Farfield energy transfers and turbulence dissipation agree within a factor of 3 throughout the measurement profile.

The suggestion is that the HOME observations of energy transfer from the semidiurnal tide to near-diurnal waves via PSI, and subsequently from low to high frequency waves, represent a skeleton of the open-ocean energy cascade.

Chapter 1

Introduction

> "Without deep mixing, the ocean would turn, within a few thousand years, into a stagnant pool of cold salty water with equilibrium maintained locally by near-surface mixing and with very weak convectively driven surface-intensified circulation." –Munk and Wunsch [1998].

The meridional overturning circulation (MOC) in the world oceans is often envisioned as a sort of conveyor belt, in a view popularized by an illustration appearing in Broecker [1987]. Warm water flows poleward from the tropics, depositing its heat at high latitudes, mostly in the North Atlantic and Southern Oceans, and becomes cold (and salty) in the process. The cold water sinks to the ocean bottom and returns to the tropics, where it rises once more to complete the loop. The heat and freshwater fluxes associated downward convection give rise to the concept of a "thermohaline circulation."

Discussions in the literature emphasize the point that the popular picture is oversimplified. In reality, tracers could not be expected to follow well-confined paths as implied by the famous illustration [Broecker, 1991]. Wunsch [2002] takes the position that, since mechanical forcing by wind and tide actually "drive" the general circulation of the ocean, the term "thermohaline" should be used only to describe transports of heat and salt. On the other hand, Rahmstorf [2003] maintains that the concept of a separate thermohaline branch remains useful, even if buoyancy and heat fluxes are confined only to the top of the ocean. Model studies of climate sensitivity are cited as an important area where changes in regional heat

and freshwater forcing may influence the ocean circulations, detectable apart from changes due to wind forcing.

1.1 Mixing recipes

The central role of mechanical forcing to ocean circulation has long been understood. In a classic paper, Munk [1966] set the problem as a global mean balance between advection and diffusion, the former associated with upwelling of cold, dense deep water, and the latter with turbulent mixing. In this way, the stratification of the oceans could be maintained. The inferred velocity and eddy diffusiviy were the canonical values $w \approx 1$ cm day^{-1} and $\kappa \approx 1$ cm^2 sec^{-1} in the abyssal ocean. Mechanical energy to support the mixing rate was estimated at 2 TW.

In the intervening decades, it has become clear that mixing in the ocean interior is strongly associated with boundaries and rough topography. From measurements taken in the Brazil Basin, Polzin et al. [1997] inferred elevated mixing rates near the Mid-Atlantic Ridge which were 20–30 times larger than the background $\kappa_{\rm PE}$ measured above flat topography. High dissipation rates were not confined to the turbulent boundary layer, but extended for hundreds of meters above the bottom. They concluded that enhanced mixing was due to internal waves, generated or scattered by the rough bottom topography, propagating upward before decaying to turbulence.

Satellite altimetry has also became capable of tracking barotropic tidal fluxes [Egbert, 1997, Egbert and Ray, 2001]. "Hotspots" of barotropic loss were identified at bathymetric features such as the Mid-Atlantic Ridge and Hawaii. Detection of a faint surface signature near Hawaii suggested that the tidal losses were, at least in part, due to the generation of propagating low-mode internal tides [Ray and Mitchum, 1997].

In revisiting the problem some four decades later, Munk and Wunsch [1998] retained the original [Munk, 1966] estimates of both turbulent diffusivity and advection. However, these global averages are now interpreted as proxies for "patchy"

turbulent mixing concentrated at boundaries, topography, and other potential hotspots such as fronts and mesoscale eddies. The only two viable sources for this amount of energy remain the winds and the astronomical tides [Munk and Wunsch, 1998, Wunsch and Ferrari, 2004].

1.1.1 The internal wave energy cascade

Most diapycnal mixing in the ocean is attributed to turbulence caused by breaking internal waves [Garrett and Munk, 1972, Gregg, 1987]. The mechanic energy required support Munk [1966] inferred a global average mixing rate, balancing the rate of deep water formation against this turbulent mixing. He reported an implied eddy diffusivity of 10^{-4} m^2 s^{-1} = 1 cm^2 s^{-1}, sufficient to balance the sinking of $\approx$ 25 Sv of deep water.

Turbulent mixing occurs at scales of order 1 cm and smaller. In contrast, most of the mechanical energy input to the ocean, due to winds and tides, occurs at scales of tens to hundreds of kilometers. Spanning the extremes between winds and tides and turbulence are internal waves, which are envisioned to form an energy cascade from the largest scales to the smallest scales in the oceans. The statistical view of oceanic internal waves is summarized in the Garrett-Munk (GM) spectrum [Garrett and Munk, 1972, Munk, 1980], which hypothesizes a universal spectral shape for a continuum of waves. Much work during the past few decades has gone into studying nonlinear interactions which could transport energy across scales in a GM spectrum [Hasselmann, 1966, Olbers, 1976, McComas and Bretherton, 1977, McComas and Müller, 1981b]. An review is given in Müller et al. [1986].

McComas and Bretherton [1977] found three dominant interactions occurring within the GM spectrum: Induced Diffusion (ID), Elastic Scattering (ES), and Parametric Subharmonic Instability (PSI). Each interaction involves a triad of waves which are highly scale separated, in the sense that one wave has very different spatial scale or frequency from the other two. As a result, energy is transferred across wide jumps in the internal wave spectrum.

The names were chosen by analogy to familiar physical systems: ID involves transfer between two small-scale, high-frequency waves, mediated by a third, ener-

getic wave at low frequency and much larger scales. In a field of many waves, the net result is diffusion in wavenumber space. ES is analogous to Bragg scattering: a wave is scattered to a near-mirror-image of itself by passing through a background wave with half its vertical wavelength. Finally, PSI transfers energy between a large-scale wave and a pair of nearly opposed, small-scale waves. The classical description involves exciting a pendulum by vertically translating its support at twice the pendulum frequency.

Evaluation of the energy transfer integrals found that the GM spectrum is in near-equilibrium at high frequencies with respect to ID; and in the $2f$–$4f$ band with respect to PSI [Olbers, 1976, McComas and Müller, 1981b, Müller et al., 1986]. Energy transfer by PSI is found to create an excess of energy in subharmonic frequencies f–$2f$, implying that there is an unknown sink for low frequency energy. Notably, the GM spectrum includes no tides, so that frequencies between $2f$–$4f$ and f–$2f$ may be significantly out of balance with respect to PSI where tides are present. The GM model also assumes vertical symmetry in the internal wave spectrum, so that ES produces no net energy transfer. This symmetry does not hold for wind-generated near-inertial waves or for internal tides near generation sites, hence ES may also play a role in the real ocean.

Resonant interaction theory is exact only in the limit of small nonlinearity. As ID moves energy to high wavenumbers the nonlinearity grows, and the validity of the approximation is becomes uncertain. To address this concern, eikonal approaches have also been used to model the interaction between low frequency, large scale waves and waves in the high frequency, small scale region of the spectrum [Henyey et al., 1986, Broutman and Young, 1986]. This "ray-tracing" method tracks small-scale "test waves" as they propagate through the large scale, slowly-varying "background field." Wave triads do not appear in this model; instead, test waves are assumed not to interact with one another as they pass through and are refracted by the background field.

1.1.2 Connecting winds and tidal forcing to the continuum

An outstanding question remains: how do the main energy sources for internal waves, the winds and the tides, which vary by location and time, support a near-universal continuum of internal waves? Nonlinear wave interactions that transfer energy between scales in the internal wavefield have been studied primarily in the context of a GM spectrum. If enhanced mixing is confined around areas of strong internal tidal or near-inertial wave generation, then are energy transfers in a near-GM spectrum the appropriate model for the turbulent energy cascade, or does a different energy cascade exist for strongly non-GM wavefields?

The PSI interaction, in particular, has attracted recent attention as a possible first step in the the tidal energy cascade [Hibiya et al., 2002, MacKinnon and Winters, 2005, Carter and Gregg, 2006, Alford et al., 2007, Young et al., 2008]. The results suggest that PSI of the internal tide can transfer energy from a coherent internal tide to subharmonic waves of near-diurnal frequency on timescales an order of magnitude shorter than PSI timescales in the GM spectrum.

1.2 Outline of the thesis

The purpose of this thesis is to investigate, in observational data, nonlinear interactions which transfer energy from the low-mode internal tide and wind-generated near-inertial waves into the internal wave continuum. Novel spectral techniques are used to identify interacting waves and their resonant configurations. The results are compared to existing theories of wave-wave interactions.

Data were taken from the Research Platform *FLIP* in 2001–2002, during the Hawaii Ocean Mixing Experiment (HOME), which intensively surveyed the tidal energy cascade near the Hawaiian Ridge. Both the 2002 Nearfield location, on the southwest shoulder of Kaena Ridge and the 2001 Farfield, located 430 km to the southwest, are located in a propagating semidiurnal tidal beam. In the Nearfield, 11,000 profiles of density and velocity, to a depth of 800 m, were collected at 4 minute intervals over a period of 30 days. At the Farfield, 9000 profiles were obtained. The duration of the records, each spanning 2 complete spring-neap

cycles, allows statistically significant observation of nonlinear interactions.

Chapter 2 presents evidence for nonlinear interaction between the low-mode, semidiurnal tide and high-mode, diurnal motions in the Nearfield of Kaena Ridge. Bispectral analysis is used to show phase coupling between the dominant M_2 frequency, long-vertical-scale internal tide and waves with frequency near $\frac{1}{2}M_2$ and vertical scale $\approx$ 100 m. A novel prefiltering separates upward-propagating from downward-propagating subharmonic waves, resulting in increased statistical significance of the bicoherence and supporting the wave triad configuration predicted by parametric subharmonic instability (PSI).

Subharmonic energy is also found to vary with the fortnightly cycle. A view of the bicoherence in the time domain shows that resonant interaction "events" are visible during peak spring tide. Growth timescales are found to be 4–7 days, in good agreement with theoretical predictions.

Chapter 3 investigates further nonlinear interactions which transfer energy from low frequency shears, which include both the tidal subharmonic and wind-generated, near-inertial shears, to high frequencies. Both the HOME Nearfield and Farfield data are examined, with the Farfield taken as the more representative view of the open ocean spectrum. Stress-shear covariances $-\left\langle u_i' w' \frac{dU_i}{dz} \right\rangle$ are introduced as a method of estimating energy transfer rates. The energy bispectrum is used to demonstrate that significant energy transfers are confined to pairs of high frequency waves with nearly equal frequency. This finding is consistent with both ID and eikonal models of nonlinear interaction. However, wavenumber analysis shows while a wide variety of triads are active, they do not generally satisfy the scale assumptions of either model.

Estimates of turbulent dissipation are made from overturns analysis at both locations. The Nearfield energy transfer rate of order 1×10^{-7} W kg^{-1} is somewhat higher than the dissipation estimates, but agrees within an order of magnitude. The Farfield transfer rate is about 3 times smaller, and agrees with the dissipation rate within a factor of 3 throughout the water column.

The results are summarized in Chapter 4. Taken together, the tidal-subharmonic and low frequency–high frequency transfers outline a significant energy pathway

from internal tidal and wind forcing into the internal wave continuum.

Chapter 2

Subharmonic energy transfer from the semidiurnal internal tide at Kaena Ridge

2.1 Introduction

An estimated 2 TW energy for diapycnal mixing, equivalent to a globally-averaged diffusivity of order $10^{-4}\mathrm{m}^2\,\mathrm{s}^{-1}$, is needed to balance deep water formation and maintain the abyssal stratification of the world ocean [Munk and Wunsch, 1998, Wunsch and Ferrari, 2004]. Tidally-driven dissipation remains one of the viable candidates for producing this mixing rate in the deep ocean. A downscale energy cascade is hypothesized, wherein energy at large spatial scales is transferred from the tides through ever-smaller-scale internal waves, until it is lost to turbulent dissipation. Nonlinear wave-wave interactions are thought to play a key role in this process [Müller and Olbers, 1975, McComas and Bretherton, 1977, McComas and Müller, 1981b, Müller et al., 1986].

Resonant nonlinear interactions were first considered for discrete sets of ocean waves by Phillips [1960]. The analysis was subsequently extended to continuous-spectrum wavefields [Phillips, 1961, Hasselmann, 1962, 1963a,b, Bretherton, 1964, Benney and Saffman, 1966]. McComas and Bretherton [1977] examined energy

transfers in a Garrett-Munk (GM) model spectrum and found three distinct mechanisms, which they named Induced Diffusion, Elastic Scattering, and Parametric Subharmonic Instability.

Each named interaction involves a resonant triad of waves which is highly scale-separated in at least one of frequency and wavenumber. Induced Diffusion (ID) transfers energy between two similar-scale waves and a third wave with much lower frequency but much larger wavenumber. Elastic Scattering (ES) involves a pair of waves with nearly identical horizontal wavenumbers but opposite vertical wavenumbers, and a third wave with very small horizontal wavenumber but nearly double the vertical wavenumber.

The focus of this study is Parametric Subharmonic Instability (PSI), in which a large-vertical-scale wave interacts with a pair of much smaller-vertical-scale waves which have nearly opposed wavenumbers. Equatorward of $\sim 28.9°$ latitude), the subharmonic of the semidiurnal M_2 tide can exist as a free wave. There, PSI enables a nonlinear energy transfer between the low-mode semidiurnal tide and pairs of high-mode subharmonic waves.

Bispectral analysis has been used to successfully observe nonlinear coupling in turbulence [Kim and Powers, 1979] and surface gravity waves [Elgar and Guza, 1985a,b, Elgar et al., 1995]. Initial estimates of the PSI interaction timescale were very long, suggesting that the interaction could not be detected experimentally under general open ocean conditions [McComas and Müller, 1981a, Olbers and Pomphrey, 1981, Müller et al., 1986]. Early bicoherences reported by Neshyba and Sobey [1975] have been attributed to kinematic effects rather than nonlinear resonance and energy transfer.

Shorter interaction timescales are not ruled out for non-independent, non-Garrett-Munk wavefields, such as one dominated by a strong, coherent internal tide [Olbers and Pomphrey, 1981, McComas and Müller, 1981a]. Theoretical studies which include an internal tide suggest a "fast" PSI with a timescale of a few days, rather than a hundred days [Hibiya et al., 1998, 2002, MacKinnon and Winters, 2005, Frajka-Williams et al., 2006, Young et al., 2008].

The Hawaiian Ridge presents nearly ideal conditions for observing nonlin-

ear interactions between the internal tide and existing wavefield. Barotropic tidal flow is essentially perpendicular to the (2000-km long) ridge [Rudnick et al., 2003] , with an M_2 barotropic loss estimated at 18 ± 6GW [Egbert and Ray, 2000]. During the Hawaii Ocean Mixing Experiment (HOME), the structure and propagation of the internal tide were intensively studied at the Hawaiian Ridge. In the HOME Nearfield program, the Research Platform *FLIP* was moored on the shoulder of Kaena Ridge in a six-week deployment. Using a combination of Doppler sonars and profiling CTDs from *FLIP*, Rainville and Pinkel [2006] observed a coherent, principally low-mode semidiurnal tide which dominated the velocity and displacement fields. They also found a significant diurnal energy flux accompanied by strong vertical shears.

Frajka-Williams et al. [2006] calculated wavenumber bicoherences from AVP profiles taken during HOME. The results were inconclusive due to the small number of profiles, unknown spatial variability between profiling stations, and absence of frequency information. Meanwhile, Carter and Gregg [2006] found persistent near-diurnal waves coupled to the semidiurnal tide during their shipboard survey in HOME Nearfield. They reported a strong bicoherence within a depth range 525 m–595 m, consistent with an observed M_2 tidal beam.

The present study attempts to document PSI at Kaena Ridge, using the month-long profiling timeseries collected aboard the R/P *FLIP* during HOME Nearfield. Section 2.2 begins with a brief overview of resonant nonlinear interaction theory. In Section 2.3, the *FLIP* observations are presented. They show apparent growth of diurnal shears during successive fortnightly cycles. Section 2.4 examines the principal spectral components in the data. Section 2.5 discusses bispectral analysis and its application to near-inertial PSI. Significant bicoherences are presented as evidence of nonlinear energy transfer. In Section 2.6 we demonstrate how prefiltering in wavenumber-frequency space improves bicoherence observations and helps identify the resonant interactions. In Section 2.7 we compute triple products of interacting waves in the depth-time domain, showing interaction "events" as they occur. Section 2.8 compares theoretical and observed timescales for subharmonic growth. Finally in Section 2.9 we compare the findings in the

Nearfield to the Farfield and summarize our results.

2.2 Background

The theory of weak resonant interactions describes systems of waves in which each member approximately satisfies the linear dispersion relationship. For internal waves,

$$\omega^2(\mathbf{k}) = \frac{f^2 m^2 + N^2(k^2 + l^2)}{k^2 + l^2 + m^2}, \quad \mathbf{k} = (k, l, m). \tag{2.1}$$

When the waves also satisfy the resonance conditions for wavenumber and frequency, e.g., a triad of waves with some numbering convention $(1, 2, 3)$, such that

$$\mathbf{k}_1 + \mathbf{k}_2 = \mathbf{k}_3, \tag{2.2}$$

$$\omega_1 + \omega_2 = \omega_3, \tag{2.3}$$

then a weak exchange of energy will take place between the members.

The amplitudes a_1, a_2, a_3 of the waves are approximately related by

$$\dot{a}_3 = -\epsilon i \omega_3 \Gamma_{123} a_1 a_2, \tag{2.4}$$

where the interaction coefficient Γ_{123} is a function of the member wavenumbers [Phillips, 1960, Hasselmann, 1962]. The ϵ is a reminder that the interaction must remain small, a restriction that will eventually be exceeded if the exponential growth continues for an appreciable time.

Young et al. [2008], hereafter referred to as *YTB08*, consider a special case of PSI when the subharmonic waves are near-inertial. The finite amplitude tidal "pump" field has frequency $\omega = 2f_0 + \sigma$, where f is the local inertial frequency and σ is a "small" detuning parameter. Exactly-resonant pairs of near-inertial waves ($\sigma = 0$) will grow exponentially with a rate $\gamma_{\max}$, which depends upon the pump amplitude and the wavenumbers of the participating waves.

$$\gamma_{\max} = \frac{1}{2}\sqrt{\upsilon^2 - \left(\frac{N^2}{2f_0}\right)^2 \left(\frac{k_1^2}{m_1^2} + \frac{k_2^2}{m_2^2} - 2\frac{\sigma f_0}{N^2}\right)^2}, \tag{2.5}$$

where

$$\upsilon = \frac{ak^2}{4(\omega - f_0)}. \tag{2.6}$$

If $\sigma \geq 0$ and hence $\omega \geq 2f_0$, pairs of near-inertial waves can still grow exponentially with a rate near $\gamma_{\max}$, provided that the pump strength υ^2 dominates the detuning represented by the second term under the square root. *YTB08* note that the dominant term, among the many that affect the M_2 instability, quantifies the lateral advection of horizontal subharmonic Reynolds stress.

2.3 Observations

2.3.1 Site and instruments

Kaena Ridge is an energetic generation site for the internal tide [Egbert and Ray, 2001, St. Laurent and Garrett, 2002, Rudnick et al., 2003]. During the 2001 HOME Nearfield experiment, the Research Platform *FLIP* was moored in the Kauai Channel at (21.68° N, 158.63° W), in 1100 m of water. The location on the southwest shoulder of Kaena Ridge allowed the observation of a upward- and southward-propagating M_2 tidal beam emanating from the northeast edge of the ridge [Rainville and Pinkel, 2006]. The previous year, the HOME Farfield component was deployed 430 km to the south-southwest, in the approximate path of a propagating M_2 tide. Both locations are shown in Figure 2.1.

The Nearfield data comprise 11,768 profiles of velocity and density, collected at 4 min intervals during the 6-week *FLIP* deployment. Over a similar period of time, about 9400 profiles were collected in the Farfield. Temperature and salinity data were recorded by tandem SeaBird SBE11 CTDs with a vertical resolution of approximately 2 m. The *Deep-8*, a combination up/down-looking Doppler sonar with 4 beams per direction, measured horizontal velocities with a 4 m resolution. Vertical velocities were inferred from isopycnal motions derived from the CTD data. Figure 2.2 shows a diagram of *FLIP* and its instruments. A detailed discussion of the instruments and deployment site is found in Rainville and Pinkel [2006].

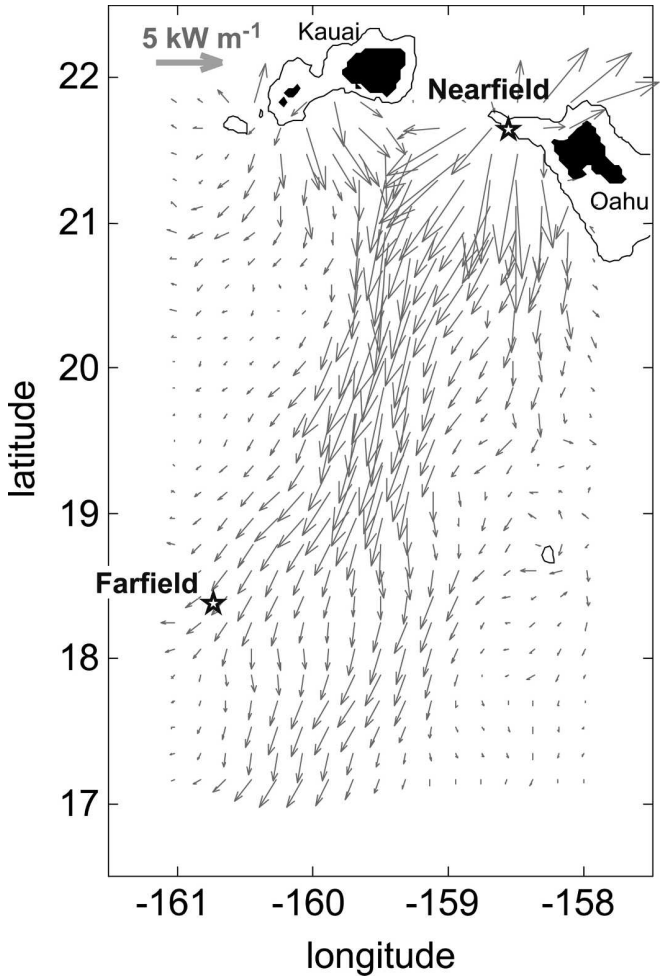

Figure 2.1: Deployment of the Research Platform *FLIP* in 2001–2002 [Rainville and Pinkel, 2006]. As part of the Hawaii Ocean Mixing Experiment, *FLIP* was moored at two locations near Kaena Ridge, Hawaii. During the 2002 Farfield component, the measurement location was approximately 430 km to the southwest of the the ridge crest, in the approximate path of an M_2 tidal beam (model fluxes are shown by the arrows). The 2002 Nearfield component placed *FLIP* on the shoulder of Kaena Ridge in approximately 1100 m of water, in a location intersecting the southward-propagating ray emanating from the north ridge.

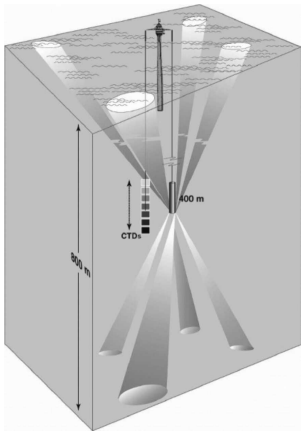

Figure 2.2: Schematic of R/P *FLIP* Instrumentation during HOME, 2001–2002. Tandem Seabird SBE11 CTDs profiled down to approximately 800 m once every 4 minutes with approximately 2 m resolution. The *Deep-8* Doppler sonar recorded horizontal velocities with approximately 4 m vertical resolution. Vertical velocities were inferred from the motion of isopycnals as measured by the CTDs. More than 11000 profiles were collected during the Nearfield and more than 9000 during the Farfield.

2.3.2 Coordinate systems

In an Eulerian frame of reference, the mutual advection of finite amplitude waves is a non-linear process that is reversible. In an attempt to minimize the signature of reversible distortion in the bispectral estimates, we carried out the analysis in semi-Lagrangian coordinates. Here, the vertical coordinate is fixed to isopycnals, thereby reducing Doppler spreading of high-vertical-wavenumber motions [Pinkel, 2008]. Subharmonic motions with high shear more nearly resemble linear plane waves in the semi-Lagrangian frame. Reference isopycnals are chosen at two-meter mean separation, using the cruise-averaged density profile $\rho_0(z)$. This discussion focuses on the semi-Lagrangian analysis.

A WKB-stretched vertical coordinate $z_{\rm wkb}$ was also defined from the averaged buoyancy profile $N(z)$. The stretched coordinate preserves straight phase lines for linear internal waves and is useful for comparing vertical scales as $N(z)$ changes [Gill, 1982]:

$$z_{\rm wkb}(z) = \frac{1}{N_0}\int_0^z N(z)dz. \tag{2.7}$$

The reference buoyancy frequency N_0 was chosen such that the total profiling depth

is the same after WKB stretching.

2.3.3 Displacement, velocity, shear

Isopycnal displacements η (Fig. 2.3) and baroclinic horizontal velocities u, v (Fig. 2.4) show a semidiurnal tide with a clear fortnightly cycle and long vertical scales. Barotropic velocities were removed from the velocity record using estimates from the TPXO.5.1 model [Egbert, 1997]. Baroclinic vertical displacements are of order 100 m at depths below 500 m. Horizontal velocities approach 0.5 m s^{-1} in the upper thermocline. Predominantly downward propagation of the phase lines indicates upward energy propagation, consistent with an upward-southward beam emanating from the north rim of the ridge crest [Rainville and Pinkel, 2006] .

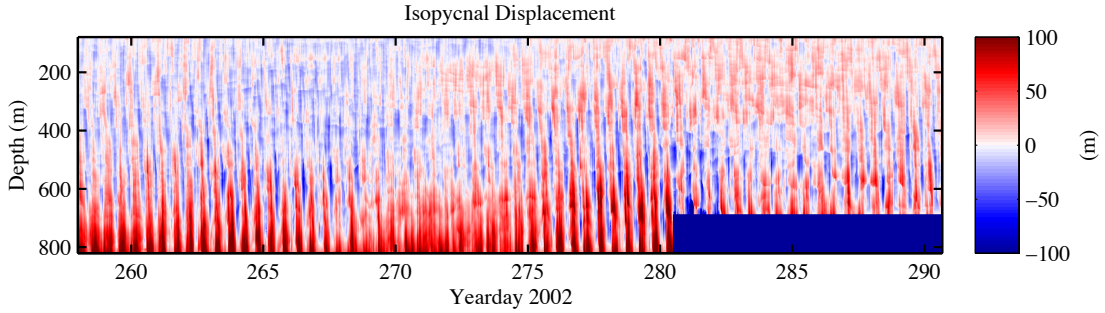

Figure 2.3: Isopycnal Displacement. Baroclinic vertical displacements are of order 100 m at depths below 500 m. Long vertical scales dominate the record. Peak spring tides appears on days 265 and 279. The maximum depth of the CTD profiles was reduced to 710 m after day 280.

Semi-Lagrangian vertical velocity w was computed as the centered difference of displacement. Tidally bandpassed w_{tide} was integrated to show the displacement η_{tide} due to tidal motions only (Fig. 2.5). The downward phase propagation and coherent vertical structure are more clearly seen after WKB-scaling and normalization.

Velocities (u, v, w) and isopycnal displacement η were WKB-scaled to normalize variances across depths,

$$\eta = \eta_0 \sqrt{\frac{N}{N_0}}, \quad w = w_0 \sqrt{\frac{N}{N_0}}, \quad (u, v) = (u_0, v_0) \sqrt{\frac{N_0}{N}}. \tag{2.8}$$

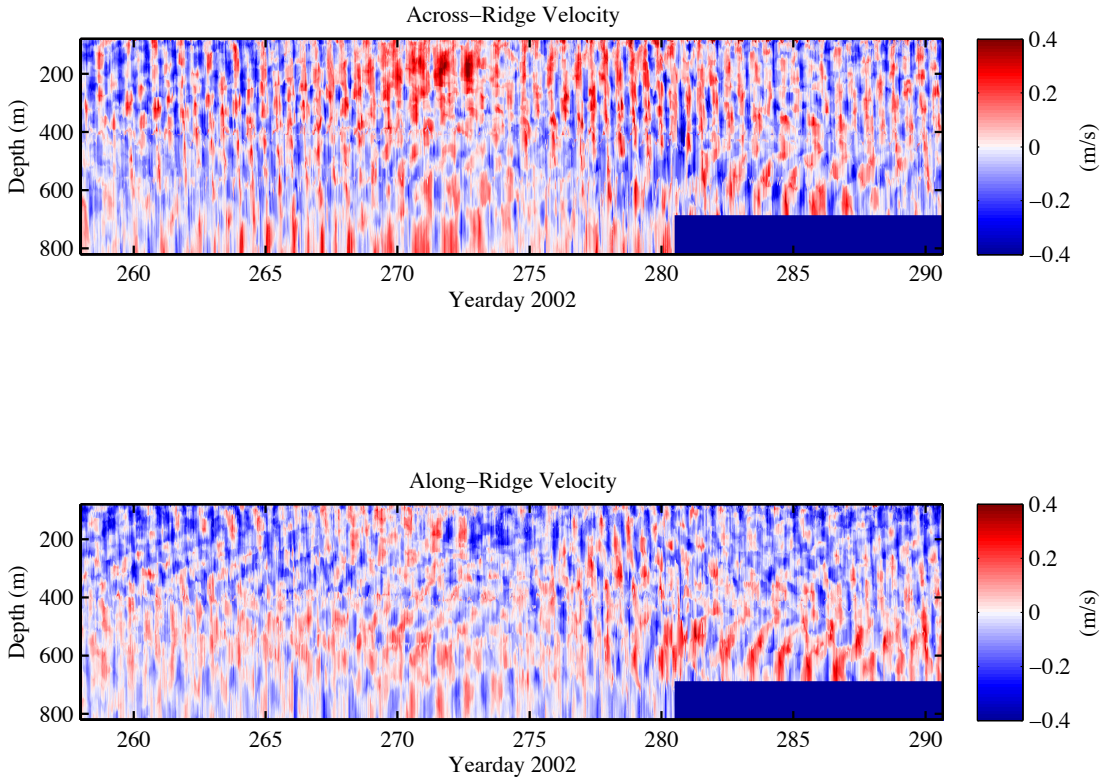

Figure 2.4: Velocity, Semi-Lagrangian (Isopycnal) Coordinates. The record contains a superposition of large vertical scale, semidiurnal motions and lower-frequency, shorter vertical scale motions. The reduced depth of the CTD profiles after day 280 affects the semi-Lagrangian velocities, which depend upon isopycnal depth information.

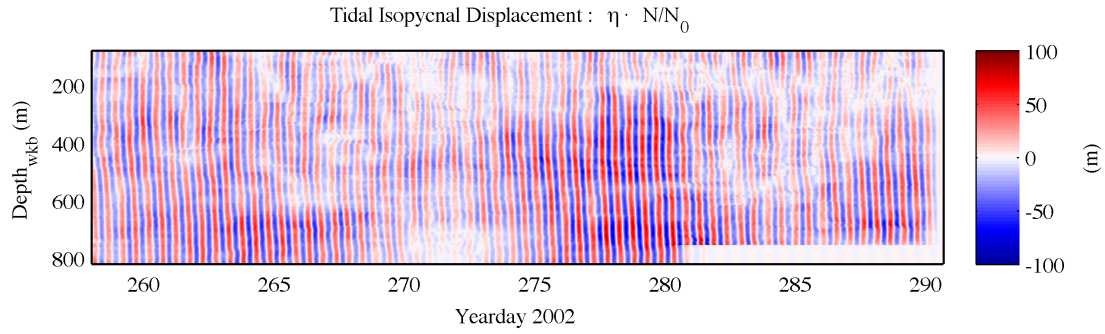

Figure 2.5: Semidiurnal-Bandpass Displacement (Semi-Lagrangian). Depth and variance are WKB-scaled. Coherent vertical structure and predominantly downward phase propagation are visible.

Semi-Lagrangian shears were computed as centered differences of velocity divided by the instantaneous separation of isopycnals (with mean separation 4 m). Shear variance varied more closely as N than the $N^{3/2}$ predicted by WKB theory. Therefore, wherever scaled shears are presented, they have been normalized by

$$(u_z, v_z) = \left(\frac{N_0}{N}\right)(u_{z0}, v_{z0}). \tag{2.9}$$

The shear record, shown in Figure 2.6, is dominated by waves of approximately 100 m vertical wavelength. There is a suggestion of a spring-neap cycle in the shear variance. Upward- and downward-propagating waves of comparable magnitude form an overlapping chevron or 'X' pattern which is most apparent below 400 m (Fig. 2.7). The pattern resembles that observed near the during the Internal Waves Across the Pacific (IWAP) experiment, near the M_2 critical latitude of 28.9° N [MacKinnon and Winters, 2005, Alford et al., 2007]. The D_1 waves below 300 m depth grow with each spring tide, exceeding the amplitude change predicted by WKB theory for waves propagating vertically through a slowly varying N^2 profile.

Several discontinuities in the data require special attention. Velocity artifacts from boundary reflections and the transition from upward-looking to downward-looking modes of the Deep-8 are visible in narrow depth bands 150–156 m, 412–424 m, and 526–552 m. The change to semi-Lagrangian coordinates spreads the disruptions over a 10–20 m range. An interruption in data collection occurs on day 280, after the 8099th profile; afterward, the depth coverage of the CTD is reduced to 700 m. The change is evident in the displacement and semi-Lagrangian velocity records.

2.4 Depth-frequency spectra

Depth-frequency power spectra were computed using the multitaper method, using a sequence of 7 prolate spheroidal tapers. Due to the interruption at day 280, only the first 8099 profiles were used for spectral estimation.

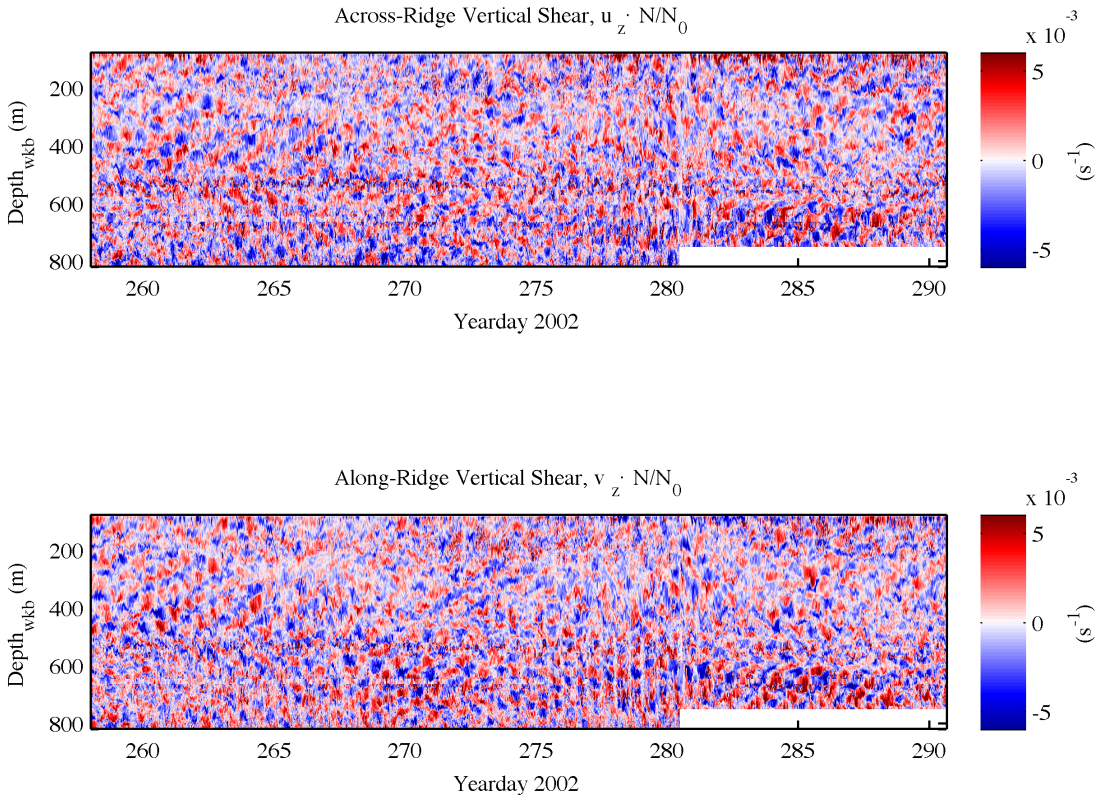

Figure 2.6: Vertical Shear, Semi-Lagrangian (Isopycnal) Coordinates. Depth is WKB-stretched, while variance is scaled by N/N_0 instead of the $(N/N_0)^{3/2}$ of WKB theory. Waves with short vertical scales and approximately diurnal period are seen propagating both upward and downward. Due to the use of semi-Lagrangian coordinates and WKB-stretching, wave crests appear as nearly straight lines. A hint of a fornightly cycle can be seen in the variance, which peaks around days 271 and 285, or about 5–7 days after peak spring tides (days 265 and 279).

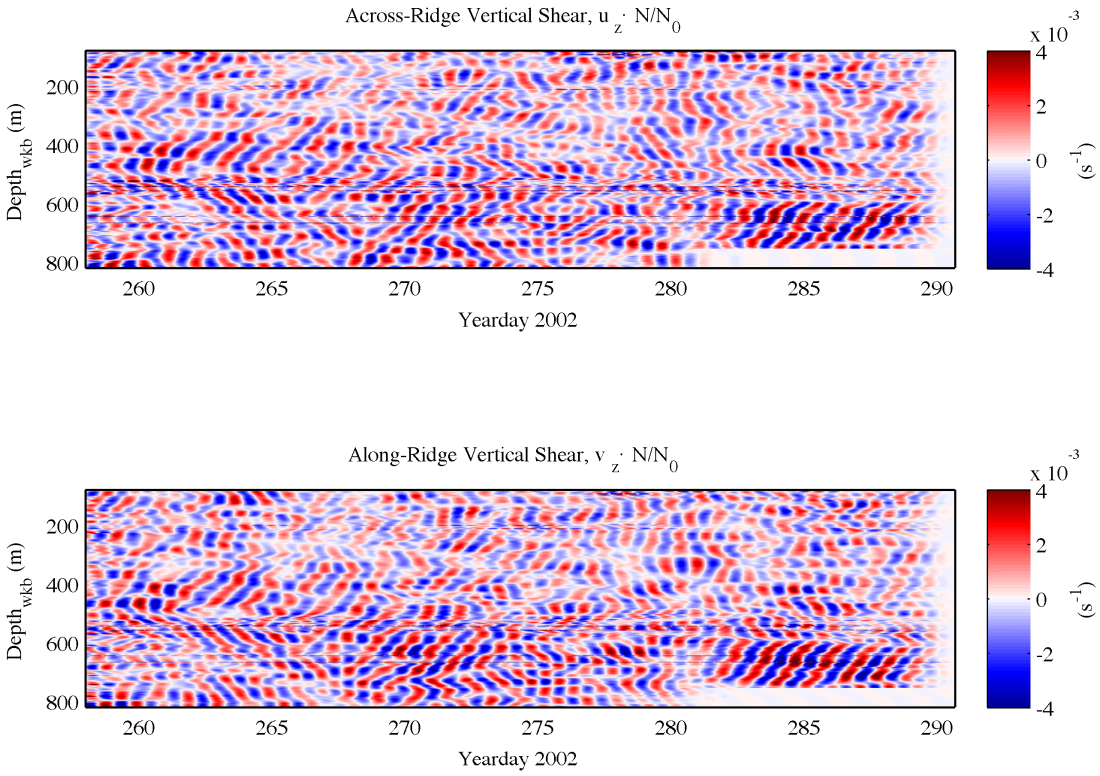

Figure 2.7: Diurnal-Bandpass Shear (Semi-Lagrangian). Depth and variance are WKB-scaled. Diurnal waves seen in Fig. 2.6 are brought out by bandpass filtering. The chevron or 'X' pattern of waves propagating in opposing vertical directions is evident during days 269–272 and 278–285, following peak spring tides (days 265 and 279).

2.4.1 Displacement and velocity spectra

The isopycnal displacement spectrum (Figure 2.8a) is dominated by an M_2 line which extends through the entire water column, peaking at around 360 m depth and again, more strongly, at about 550 m. Also evident is peak near the $\frac{1}{2}M_2$ frequency, with variance within an order of magnitude of the M_2 line. This subharmonic signal is clearly distinguishable from the local inertial frequency $f = 1/32.7$ h. Interaction lines are visible at a series of sum frequencies $M_2 + \frac{1}{2}M_2, 2M_2, \ldots$

Eulerian and semi-Lagrangian two-sided spectral estimates for complex velocity $\mathcal{U} = (u + iv)$ are shown for comparison in Fig. 2.9. Both estimates (a) and (b) display the expected M_2 line with predominantly cyclonic motions. Some anticyclonic content is present at mid depths. The near-inertial line, which we will tentatively call D_1 here, is ambiguously positioned between $\frac{1}{2}M_2$ and f. The Eulerian velocities (2.9b) show clear interaction lines at frequencies $-2D_2$, $-(D_2+D_1)$, and $(D_2 - D_1)$ due to vertical mutual advection. These lines are almost absent in the semi-Lagrangian spectrum (Fig. 2.9a).

2.4.2 Shear and strain

The near-inertial line seen in the velocity spectra is mirrored in the shears. When variances is normalized by N/N_0, the peak near-inertial shear is found in a broad band betweeen 480 and 600 meters. Smaller bursts of activity are seen near the 300 m and 340 m depths.

It is more difficult here to discriminate between f and $\frac{1}{2}M_2$; the peak between 250 and 450 m is more f-like, while it is more $\frac{1}{2}M_2$-like below 500 m. Very little shear is seen at other frequencies. M_2 is noticeably quiet in shear, as expected, given the large vertical scales of the semidiurnal tide.

The vertical strain rate η_z (Fig. 2.8b) measures the dilation of layers between isopycnal surfaces. Some strain variance is visible around $\frac{1}{2}M_2$. As with shear, the energetic M_2 motions associated with the low-mode tide create very little strain. This is consistent with *YTB08*'s near-inertial PSI model, in which the near-inertial waves are associated with horizontal Reynolds stresses rather than

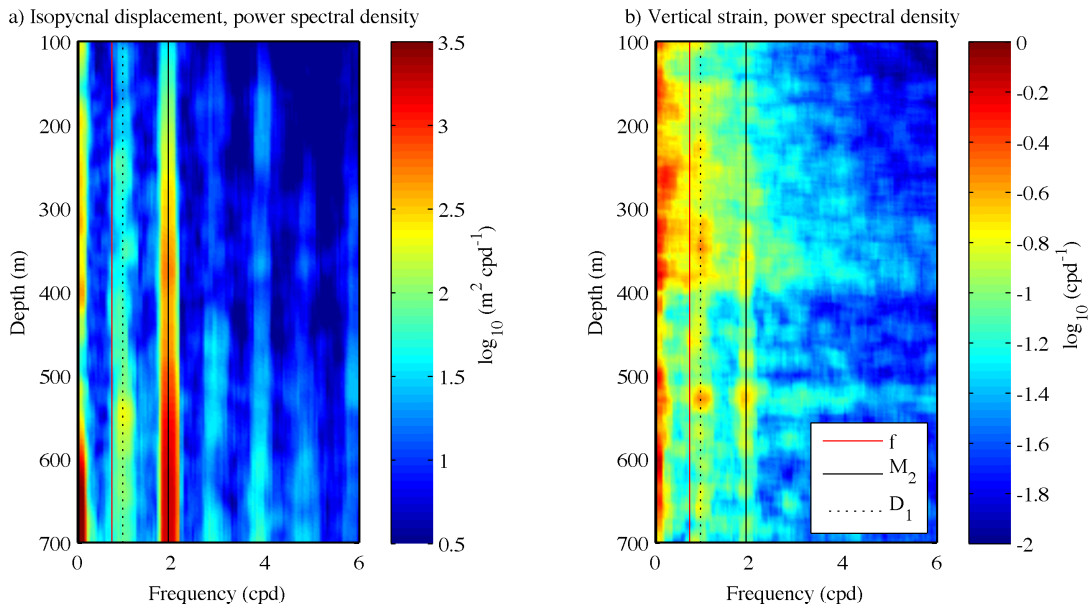

Figure 2.8: Power Spectral Estimate, Displacement and Strain (Semi-Lagrangian). a) Isopycnal Displacement. Semidiurnal motions at M_2 frequency are accompanied by a subharmonic at $\frac{1}{2}M_2$ that is clearly distinct from the local inertial frequency f. b) Vertical Strain. Some variance is visible around $\frac{1}{2}M_2$. As with shear, the energetic M_2 motions associated with the low-mode tide create very little strain.

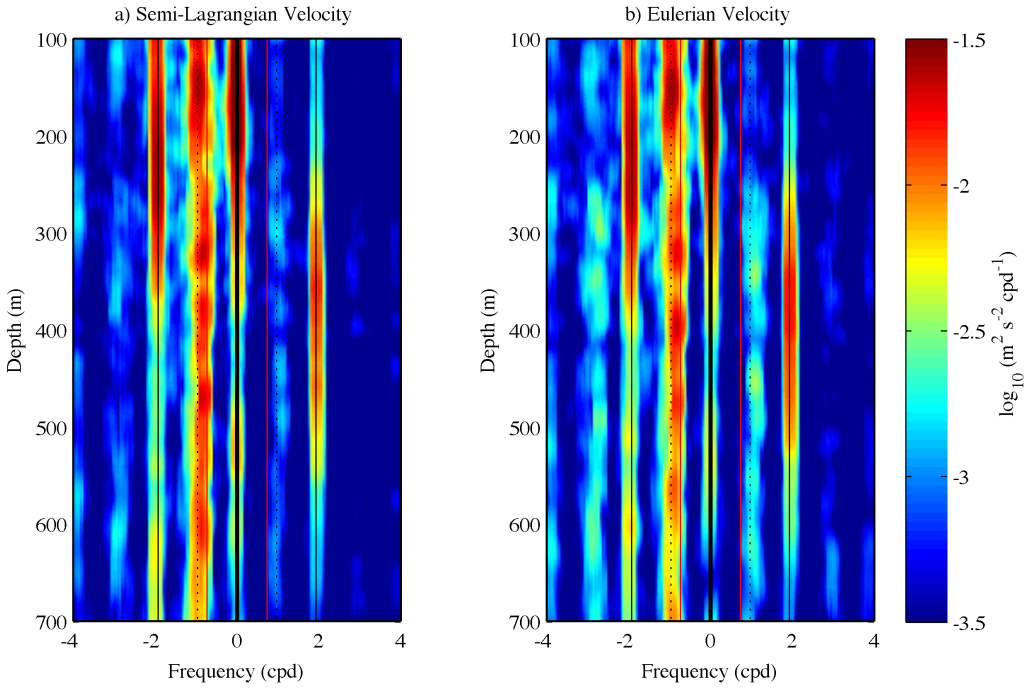

Figure 2.9: Two-Sided Power Spectral Estimates of Complex Velocity $\mathcal{U} = (u + iv)$, a) Semi-Lagrangian and b) Eulerian Coordinates. Semidiurnal motions at M_2 frequency are accompanied by large variances near its half-frequency. The subharmonic is more $\frac{1}{2}M_2$-like than f-like in both coordinate systems. Lines at the sum frequencies $-2D_2$, $-(D_2+D_1)$, and (D_2-D_1) are caused by mutual advection and are visible in the Eulerian frame (b), but not in the semi-Lagrangian frame (a).

local modulation of the buoyancy frequency N^2.

2.5 Bispectra

2.5.1 Definitions

Higher-order spectra are useful for identifying phase coupling between waves in a multiple-scale, broadband wavefield. The estimator for detecting triad (three-wave) resonances is the bispectrum, defined as the Fourier transform of the triple covariance of the signal $z(\mathbf{x})$,

$$R_3(\mathbf{x}_1, \mathbf{x}_2) = \int_{\mathbb{C}_N} z^*(\mathbf{x}) z(\mathbf{x}+\mathbf{x}_1) z(\mathbf{x}+\mathbf{x}_2) d\mathbf{x}. \tag{2.10}$$

For time series data it is usually practical to compute the covariance over time shifts $(\mathbf{x}_1, \mathbf{x}_2) = (\tau_1, \tau_2)$. The Fourier transform of this covariance is the frequency bispectrum (Kim and Powers 1979):

$$B(\omega_1, \omega_2; \omega_1+\omega_2) = E\big[A(\omega_1)A(\omega_2)A^*(\omega_1+\omega_2)\big], \tag{2.11}$$

where the $A(\omega_i)$ are the Fourier coefficients of ϕ at frequencies ω_i, and $E[\cdot]$ indicates the expected value.

If the wavefield is Gaussian, the bispectrum will be zero for all combinations of frequencies. Conversely, a nonzero bispectrum at some triple $(\omega_k, \omega_l, \omega_k+\omega_l)$ implies a fixed phase relationship between the frequencies ω_1, ω_2, and the bifrequency $\omega_1+\omega_2$.

A sample estimate for (2.11), computed over a finite record will have a nonzero value even if the wavefield is Gaussian. Therefore it is useful to establish a statistical lower bound for significant nonzero values.

The bicoherence is the bispectrum normalized by the variances,

$$b(\omega_k, \omega_l; \omega_k+\omega_l) = \left\{ \frac{|B(\omega_k, \omega_l)|^2}{E\big[|A(\omega_k)A(\omega_l)|^2\big] E\big[|A(\omega_{k+l})|^2\big]} \right\}^{1/2}. \tag{2.12}$$

This choice of normalization assures $0 \le b \le 1$. The bicoherence is χ^2 distributed for large degrees of freedom, with confidence intervals around zero bicoherence

given by $b^2_{99\%} = 9.2/n_{\text{dof}}$, $b^2_{95\%} = 6.0/n_{\text{dof}}$, $b^2_{90\%} = 4.6/n_{\text{dof}}$ [Elgar and Guza, 1988]. A discussion of effective degrees of freedom in bispectral measurements of PSI is undertaken in Appendix A.

A related quantity is the biphase, or the argument of the bispectrum (2.11),

$$\phi(\omega_1, \omega_2; \omega_1 + \omega_2) = \arctan\left[\frac{\Im\{B(\omega_1, \omega_2; \omega_1 + \omega_2)\}}{\Re\{B(\omega_1, \omega_2; \omega_1 + \omega_2)\}}\right], \tag{2.13}$$

from which the direction of the energy transfer can be inferred.

2.5.2 Bispectral Estimation

Bispectral estimates are computed at each semi-Lagrangian (isopycnal) depth, using time series up to the break on Day 280 (record 8099). Prior to taking Fourier transforms, data are divided into 3-day, 50%-overlapping subrecords and tapered with a Kaiser window. Expected values in (2.11) are approximated by taking a sample mean by frequency over a depth range and convolving with a 3×3 averaging window. The data are split into two overlapping depth ranges: an upper range of 100–500 m and a lower range 300–700 m, chosen wide enough to allow averaging over several vertical wavelengths.

Cross-bispectral variables

Frequency bispectra are computed in the cross-bispectral form

$$B(\omega_1, \omega_2) = B\left[\mathcal{U}_z(\omega_1), \mathcal{U}_z(\omega_2), W^*(\omega_1 + \omega_2)\right]. \tag{2.14}$$

Frequencies ω_1, ω_2 correspond to the appropriate Fourier coefficients of $\mathcal{U}_z$, while the bifrequency $\omega_1 + \omega_2$ corresponds to W. $\mathcal{U} = u + iv$ is defined such that u is across-ridge, pointing away, so that v is along-ridge pointing east-southeast. Time domain and Fourier representations of random variables are here used interchangeably, with the dependent variable signifying the appropriate version.

These cross-bispectral variables are chosen to maximize the signals of potential interaction partners relative to the variance of motions that are not expected to participate in the interaction. Vertical velocity W gives the clearest picture of the low-mode D_2 tides which can supply energy via PSI. Meanwhile, vertical shear, $\mathcal{U}_z$, emphasizes high-wavenumber D_1 band waves which may receive energy.

2.5.3 Bispectra, 300–700 m depth average

Figure 2.10 shows the real and imaginary parts of the bispectral estimate for the 300–700 m depth range. Large bispectral variances are seen in both the real and imaginary part of the bispectrum, near the (D_1, D_1) frequencies, with the real part several times larger (this is more easily seen in the Biphase, Fig. 2.11).

Bicoherences, in Figure 2.11, are larger than 0.6 for the same combination of frequencies, indicating that the large bispectral values in Fig. 2.10 are statistically significant. The corresponding biphase is slightly negative, between $-\pi/4$ and $-\pi/6$.

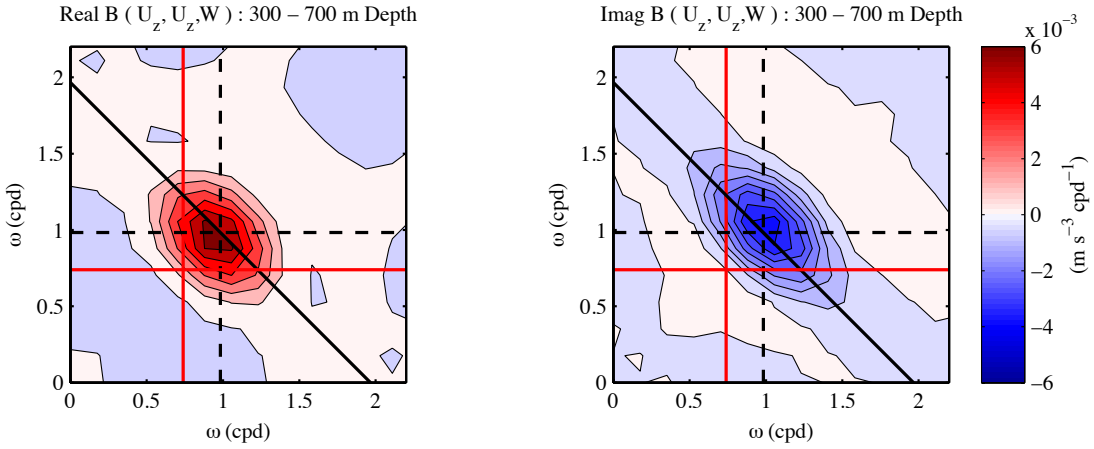

Figure 2.10: Cross-Bispectral Estimate, 300–700 m Depth. Units of the bispectra are (m s^{-3} cpd^{-1}). The axes show negative (anticyclonic) frequencies only for ω_1 and ω_2 in cycles per day. The value of the bispectrum, $B(\omega_1, \omega_2; \omega_1 + \omega_2) = B\,[\mathcal{U}_z(\omega_1), \mathcal{U}_z(\omega_2), W^*(\omega_1 + \omega_2)]$, is plotted at coordinates (ω_1, ω_2). $\mathcal{U}_z(\omega)$ is the Fourier transform of complex horizontal velocity, with u pointing across-ridge/away. $W^*(\omega)$ is the conjugate of the Fourier transform of vertical velocity. The frequencies ω correspond to negative (cyclonic) frequencies in the two-sided spectra of (Fig. 2.9). The local inertial frequency f is indicated by the red line, while the diurnal D_1 is marked by the black dotted line. The black solid line indicates the semidiurnal bifrequency (sum frequency D_2). Large bivariances are seen in both real and imaginary parts of $B(\omega_1, \omega_2)$, with the real part 2–3 times larger.

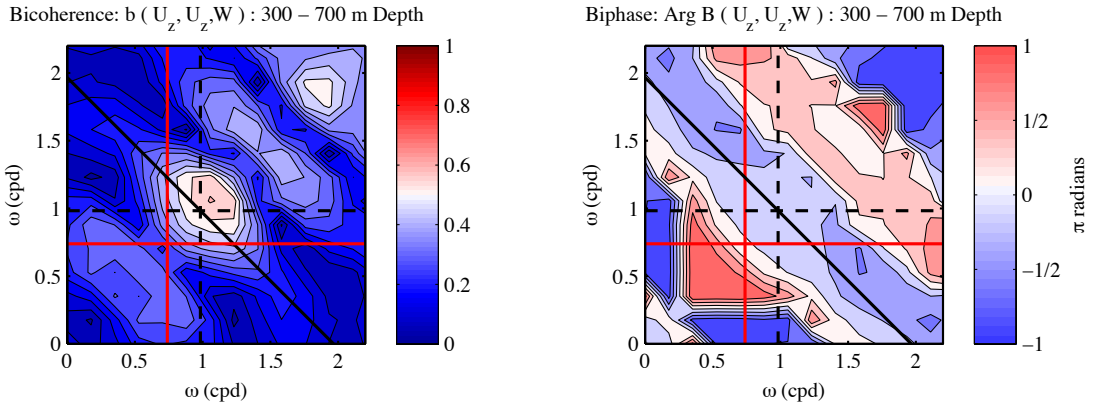

Figure 2.11: Bicoherence and Biphase, 300–700 m Depth. The axes show frequencies of ω_1 and ω_2 in cycles per day. The bicoherence $b(\omega_1, \omega_2)$, the normalized bispectrum, represents the phase coherence between triads of waves $(\omega_1, \omega_2, \omega_1 + \omega_2)$, with the result plotted at position (ω_2, ω_1). $0 \leq b \leq 1$. The local inertial f and diurnal D_1 frequencies are indicated by red and black dotted lines, respectively. The semidiurnal bifrequency D_2 is marked by the solid black line. The strong bicoherences around $(D_1, D_1; D_2)$ confirm that the large bispectral values in Fig. 2.10 are statistically significant. The corresponding biphase $\phi(\omega_1, \omega_2)$ is slightly negative, with $-\pi/4 < \phi < -\pi/6$.

2.5.4 Bispectra, 100–500 m depth average

At shallower depths, both the real and imaginary bispectra also display variance near (D_1, D_1). The biphase in Figure 2.13 is similar to that of the lower depth range (Fig. 2.11). However, the low bicoherence shows that this bispectral result is not significant.

2.6 Vertical propagation prefiltering

The canonical PSI interaction involves three waves: a parent wave along with one upward- and one downward-propagating subharmonic. The predicted relationship can be tested by computing cross-bispectra using wave fields which have been separated by direction of vertical propagation. Significant bicoherences in the lower 300–700 m depth range are expected only when bispectra (2.14) are computed using shear fields with opposite-sign vertical propagation.

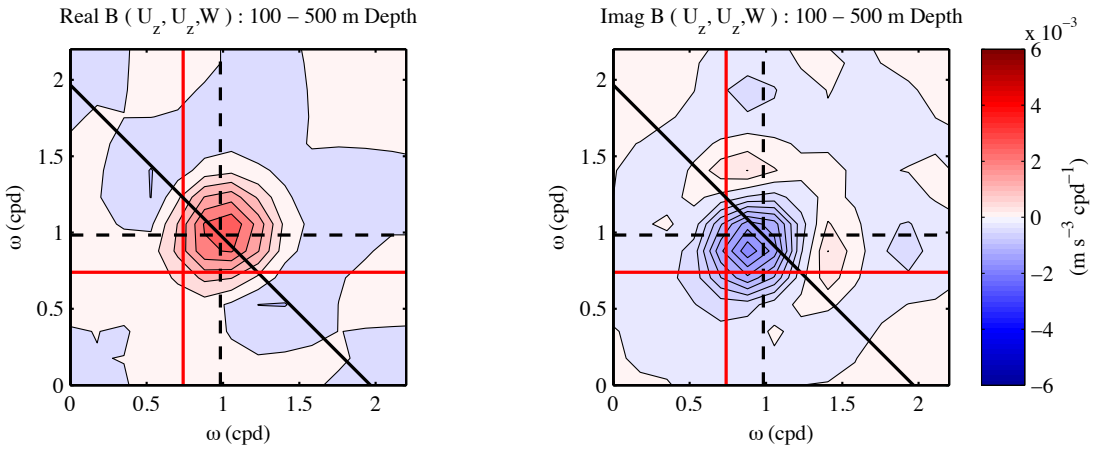

Figure 2.12: Cross-Bispectral Estimate, 100–500 m Depth. As in Fig. 2.10, but for the shallower depth range. Units of the bispectra are (m s^{-3} cpd^{-1}). The axes show frequencies of ω_1 and ω_2 in cycles per day. The value of the bispectrum, $B(\omega_1, \omega_2)$, is plotted at position (ω_2, ω_1). Some variance is seen in both the real and imaginary parts of $B(\omega_1, \omega_2)$ near (D_1, D_1), but the interaction is not significant (see Fig. 2.13).

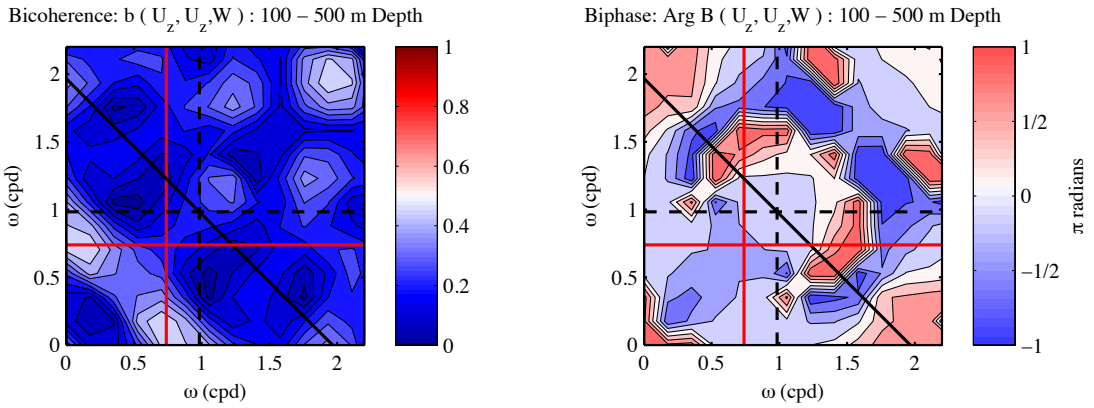

Figure 2.13: Bicoherence and Biphase, 100–500 m Depth. As in Fig. 2.11, but for the shallower depth range. The biphase is similar to that in the lower depth range (Fig. 2.11), but the nearly null bicoherence around (D_1, D_1) shows that the interaction between semidiurnal and diurnal frequencies is not statistically significant over this depth range.

Modified bispectral estimates take the form

$$B(\omega_1, \omega_2) = B\left[\mathcal{U}_z^+(\omega_1), \mathcal{U}_z^-(\omega_2), W^*(\omega_1 + \omega_2)\right], \tag{2.15}$$

where $\mathcal{U}_z^+$ and $\mathcal{U}_z^-$ contain only upward- and downward-propagating energy, respectively. To obtain this separation, the complex shears are 2-d Fourier transformed. Opposite quadrants in (ω, k)-space, containing anticyclonic and cyclonic wave components with the same sense of vertical propagation, are collected and inverse Fourier transformed to recover $\mathcal{U}_z^+$ and $\mathcal{U}_z^-$.

Prefiltering by upward/downward wave propagation reveals some asymmetry in the interacting wavefields, as shown in Figure 2.14. The bispectral variance is centered around a frequency slightly higher than D_1 in upward-propagating energy and a slightly lower frequency, between D_1 and f, in the downward field . Bivariances are somewhat smaller, at about 0.4 times the variance in the full field result, but they have similar relative magnitude and sign. Figure 2.15 shows that the peak in the bicoherence is again larger than 0.6 and is centered at the same location as the real part of the bispectrum. The biphase is slightly closer to zero than in the unfiltered case, with $\phi \approx -\pi/6$ at the peak.

By contrast, the bicoherences disappear when the computation is made using shear frequencies which have the same-sign vertical propagation. Figure 2.16 shows the results for k_z-non-resonant combinations which have two upward-propagating shears in one instance and two downward-propagating shears in the other. The bicoherence shows a clear preference for k_z-resonant combinations which can sum to the (small) vertical wavenumber of the low-mode tide.

2.7 The resonant triad in the depth-time domain

To examine the spatial structure and time evolution of the significant (D_1, D_1, M_2) interaction, the respective records are bandpassed around the interacting frequencies. The triple product is then formed in depth and time. This is the dual of the cross-bispectral estimate for selected frequencies

$$B\left[\mathcal{U}_z\left(D_1\right), \mathcal{U}_z\left(D_1\right), W^*\left(D_2\right)\right]. \tag{2.16}$$

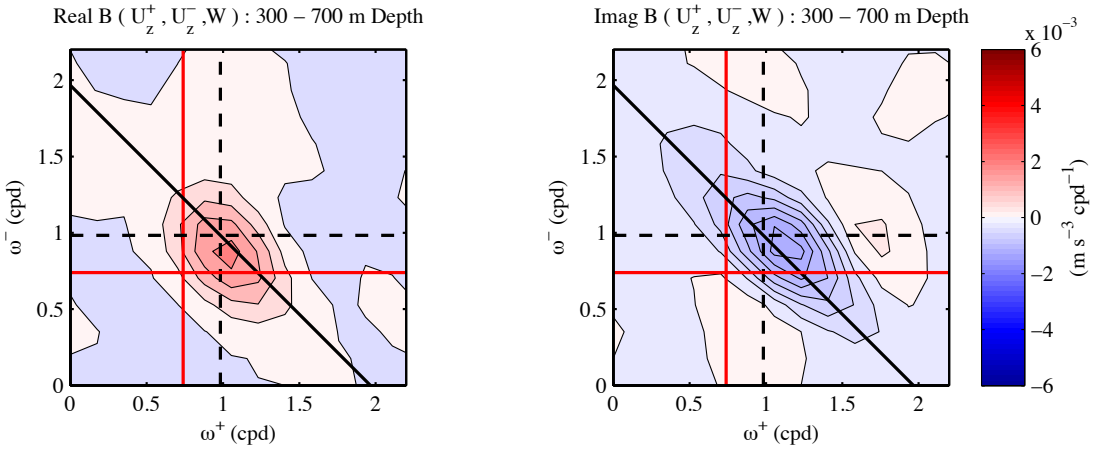

Figure 2.14: Prefiltered Cross-Bispectral Estimate, 300–700 m Depth. Units of the bispectra are (m s^{-3} cpd^{-1}). The axes indicate frequencies ω^+ and ω^-, which contain only wave energy traveling upward and downward, respectively. The value of the bispectrum, $B(\omega^+, \omega^-; \omega^+ + \omega^-) = B\left[\mathcal{U}_z(\omega^+), \mathcal{U}_z(\omega^-), W^*(\omega^+ + \omega^-)\right]$, is plotted at position (ω^+, ω^-). Compared to the bispectral estimates computed from full shear fields, an asymetry can be seen in $B(\omega^+, \omega^-)$ which favors a slightly higher frequency ω^+ in upward propagating D_1 energy and lower frequency ω^+ in downward propagating D_1 waves. Bivariances are about 0.4 that of the unfiltered version.

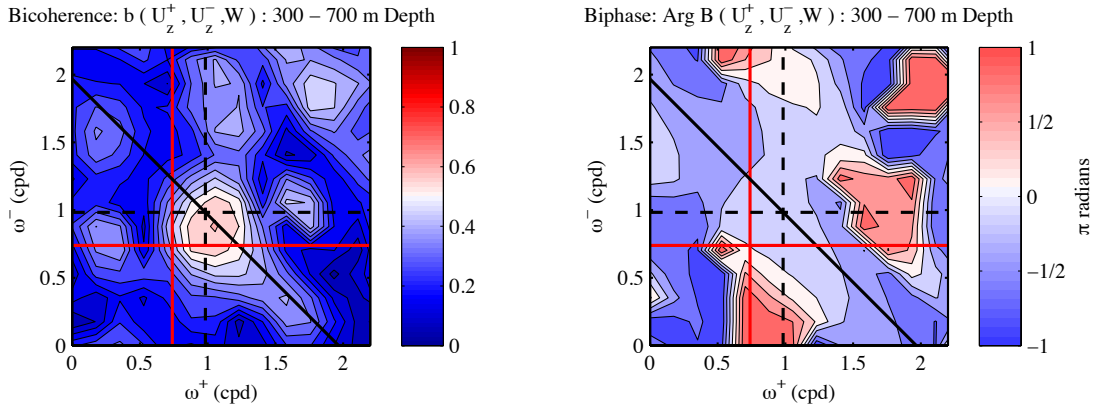

Figure 2.15: Prefiltered Bicoherence and Biphase, 300–700 m Depth. As in Fig. 2.11, but for prefiltered shear fields. The axes show frequencies ω^+ and ω^-, which contain only wave energy traveling upward and downward, respectively. The bicoherence $b(\omega^+, \omega^-; \omega^+ + \omega^-)$ is plotted at position (ω^+, ω^-). $0 \leq b \leq 1$. The local inertial f and diurnal D_1 frequencies are indicated by red and black dotted lines, respectively. The semidiurnal bifrequency D_2 is marked by the solid black line. Strong bicoherences around $(D_1, D_1; D_2)$ show that the large bispectral values in Fig. 2.10 are statistically significant. The near-zero biphase ($\phi \approx -\pi/6$) confirms that the direction of energy transfer is from D_2 waves to pairs of D_1 waves.

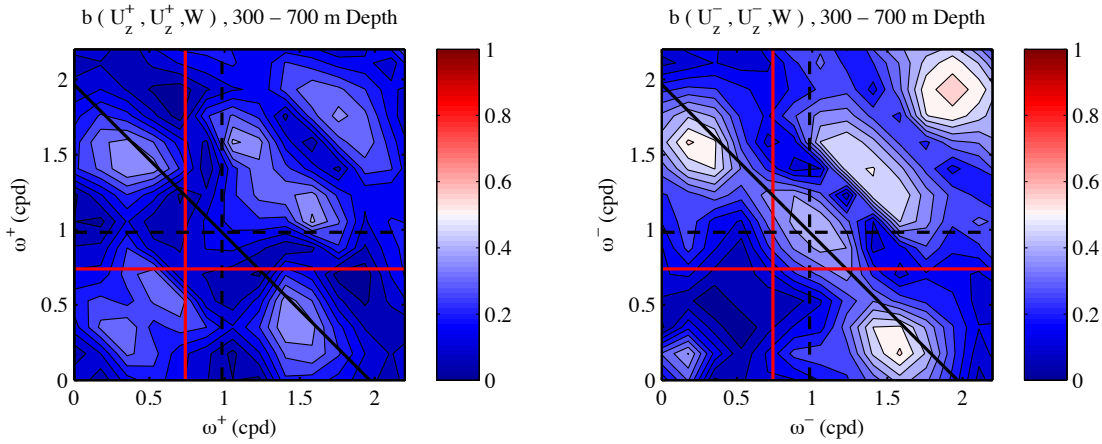

Figure 2.16: Defiltered Bicoherences, 300–700 m Depth. As in Fig. 2.15, but for non-resonant wave pairs. The axes show frequencies (ω^+, ω^+) and (ω^-, ω^-), corresponding to pairs of waves which are both upward-traveling or both downward-traveling and hence cannot satisfy the wavenumber resonance condition. The significant $(D_1, D_1; D_2)$ bicoherence seen in Fig. 2.15 is not seen in either "defiltered" version.

and inverse Fourier transforming to recover the depth-time signal.

Both unfiltered complex shear $\mathcal{U}$ and prefiltered shears $\mathcal{U}_z^+$ and $\mathcal{U}_z^-$ were bandpassed in a half-octave around the $\frac{1}{2}M_2 \approx D_1$ frequency ($\frac{1}{20}$ to $\frac{1}{28}$ cph), as shown in Fig. 2.17a and b. The product of the shears $\mathcal{U}_z^+ \cdot \mathcal{U}_z^-$ (Fig. 2.17c) shows nearly vertical crests and much longer vertical wavelength. This structure is remarkably similar to the semidiurnal tide.

Vertical velocity W was bandpassed in a full octave around D_2 ($\frac{1}{8}$ to $\frac{1}{16}$ cph). Normalized triple products $r_3(\mathcal{U}_z, \mathcal{U}_z, W)$ of the bandpassed signals were formed using both unfiltered (Fig. 2.18) and prefiltered shears (Fig. 2.19). Our notation $r_3(\cdot)$ indicates that the product has been normalized as in the definition of the bicoherence (2.12). The time-averaged $\langle r_3 \rangle$, shown to the right of each depth-time figure, is a signed estimator for the bicoherence b. A 20-m vertical averaging window has been applied to $\langle r_3 \rangle$.

The products in Fig. 2.18 are largest in the depths surrounding the tidal beam and wax and wane with a fortnightly cycle. Resonant "events" are visually identifiable during each peak spring tide, around days 264 and 279. The prefiltered interaction product (Fig. 2.18b) shows the effect most clearly, with long vertical coherence scales, indicating wavenumber resonance, and persistent sign along the time axis (shown by the monochromatic appearance).

Both Fig. 2.18a and b exhibit large $\langle r_3 \rangle$, although the magnitude is somewhat lower than the bicoherences computed by the method of Sec. 2.5.3. This may be attributed to the larger bandwidths used in computing r_3 in the time domain as opposed to the Fourier domain.

By contrast, the products involving wave pairs traveling in the same vertical direction (Fig. 2.19a and b) exhibit striped patterns which indicate non-resonance. The time average $\langle r_3 \rangle$ alternates in sign along the vertical due to the lack of wavenumber matching. As a result, the depth average will tend to zero.

The oscillatory character of the interaction product in the nonresonant case emphasizes the need for sufficient temporal and spatial coverage when estimating bispectra.

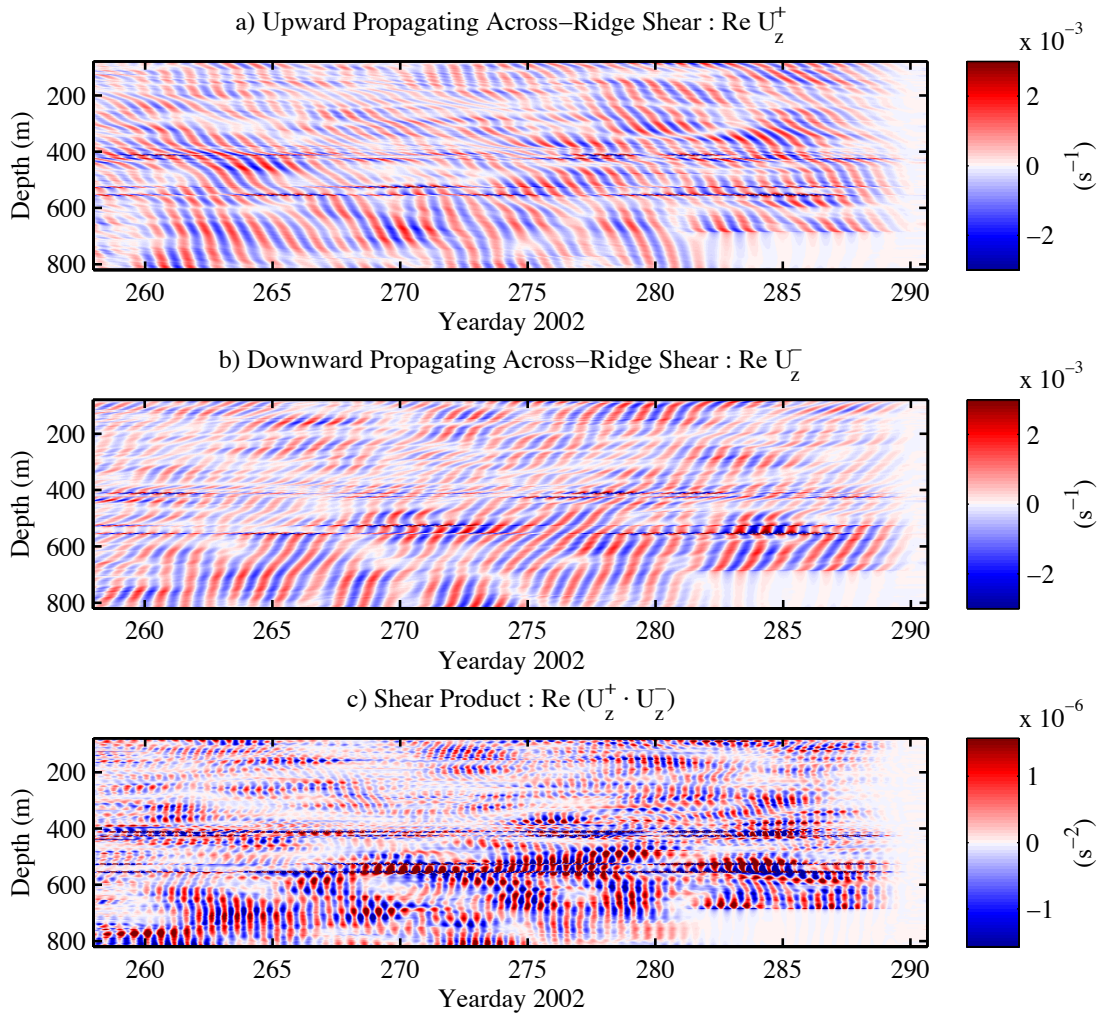

Figure 2.17: Prefiltered D_1 Shears and Shear Product. a) and b) Upward- and Downward-Propagating Vertical Shears. As in Fig. 2.7 but prefiltered for direction of vertical energy propagation. c) Product of D_1 Shears Shown in a) and b). The nearly vertical crests have a longer vertical wavelength than either D_1 field. The structure is remarkably similar to the D_2 tide. (cf. Fig. 2.18).

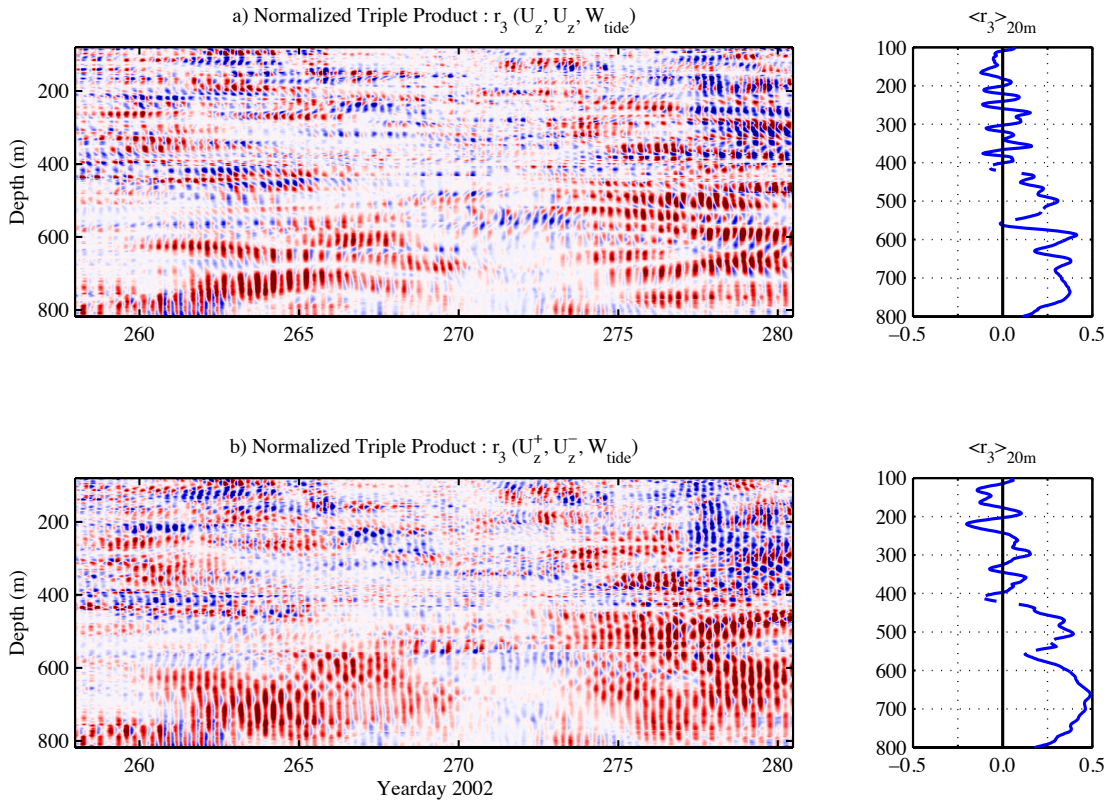

Figure 2.18: Interaction Product of Prefiltered D_1 Shears and D_2 Vertical Velocity, Showing Wavenumber-Frequency Resonance. The triple product is normalized as the bicoherence (2.12), with time means taken along isopycnals. The signed bicoherence b, shown to the right of each depth-time record, is computed from the time mean of the normalized bispectrum B, with a 20 m moving average applied in depth. a) Triple product of D_1 shears and tidal vertical velocity. b) Product of upward- and downward- filtered D_1 shears and tidal vertical velocity. Long vertical crests below 400 m indicate a shift to zero vertical wavenumber caused by the PSI triad resonance. The persistent sign of the triple correlation in time shows phase coherence of the waves.

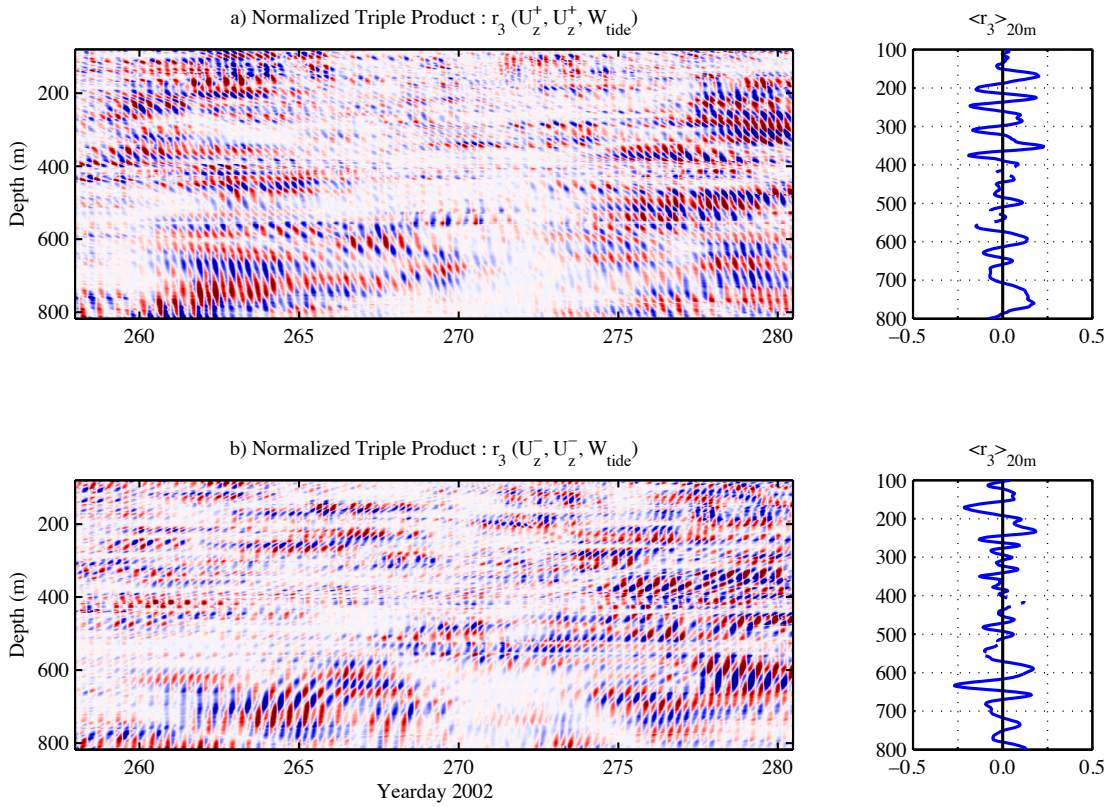

Figure 2.19: Interaction Product of Defiltered D_1 Shears and D_2 Vertical Velocity, Nonresonant Case. As in Fig. 2.18, but for shear fields which cannot satisfy the resonance conditions. Repeating striped patterns are visible in a) and b) because upward-upward and downward-downward D_1 pairs do not form a resonant triad with the dominant tide. The bicoherence b oscillates in sign, with net bicoherence near zero when the average is taken over a range of depths.

2.8 Interaction timescales and energy transfer

The near-inertial daughter waves in the theory of *YTB08* are pumped by resonant horizontal stresses in the tidal background field. The growth rate $\gamma_{\max}$ of the daughter waves is estimated using the observed semidiurnal wave amplitudes and equation (2.5) from *YTB08*. Parameters used in (2.5) are: $m = 2\pi/4000$ m, $f = 2\pi/32.48$ h, $\omega = M_2 = 2\pi/12.42$ h, $N_0 = 3.1 \times 10^{-3}$ s^{-1}.

The largest horizontal component of the tidal pump is observed in the across-ridge current, where the WKB-scaled peak velocity exceeds 0.07 m/s during the first spring tide and 0.12 m/s during the second. From the polarization relations for internal waves [Gill, 1982] we estimate a pump amplitude of 0.1278 m^2 s^{-2} and 0.2191 m^2 s^{-2}. Corresponding estimates for the growth timescale $1/\gamma_{\max}$ are 4.5 and 2.6 days. These are plausible numbers for near-inertial waves which must grow appreciably during each spring tide.

2.9 Summary

Using 30-day continuous depth and time records of displacement and velocity, bispectral estimates are calculated using vertical shears, which emphasize high-mode, subharmonic motions, and vertical velocities, emphasizing the low-mode semidiurnal tide. Semi-Lagrangian coordinates are used to reduce the effects of kinematic distortion. Depth-time averages are computed over several vertical wavelengths (3-4) and periods (3) of the subharmonic high mode wave to ensure statistical significance.

Significant bicoherences are found between vertical velocities near the M_2 frequency and the energetic shears of nearly diurnal period ($D_1 \approx \frac{1}{2}M_2$) and approximately 100 m vertical wavelength. Prefiltering the shears by direction of vertical energy propagation, bicoherences are recomputed. The interaction with the M_2 tide is shown to occur only between pairs of subharmonic waves traveling in opposite vertical directions. These results point to a Parametric Subharmonic Instability (PSI)-type interaction.

The maximum interaction product is observed during spring tides, with di-

urnal amplitudes peaking several days after the spring tide. *YTB09* would predict growth timescales of 2–4 days, given the tidal amplitudes at Kaena Ridge. Growth rates and phase lag of the bicoherent diurnal waves are consistent with the theory, although it is unclear whether the diurnal shears dissipate appreciably before propagating away between spring tides.

The depth-time interaction product of the tidal velocities and subharmonic shears reveals that the bicoherence is associated with clearly identifiable interaction "events" rather than a constant, smooth transfer of energy. The oscillatory character of non-resonant "interaction products" underscores the fact that the resonance conditions require both frequency and wavenumber matching for energy transfer to occur. Thus, there is a need for sufficient temporal and spatial averaging when forming bispectral estimates.

Data from the Fall 2001 HOME Farfield program may provide a point of comparison. The Farfield location, 430 km to the southwest of Kaena Ridge, also lies in the predicted path of a propagating M_2 tide [Rainville and Pinkel, 2006]. Profiles were also collected aboard *FLIP*, using the same complement of instruments as in the Nearfield the following year. Depth-time interaction products are computed using the Farfield data. Vertical velocity and across-ridge vertical shear are shown in Figure 2.20. The interaction product is shown in Figure 2.21.

Significant PSI bicoherences are not found in HOME Farfield. This suggests that a fairly coherent, propagating tidal beam alone is not sufficient to generate the strong PSI interactions seen in the Nearfield, where the tidal pump amplitude is both larger and much more coherent. Investigations near other baroclinic generation sites will required to test the generalizability of the results found here.

Appendix: Significance of bicoherence

Formal confidence intervals for zero bicoherence can be estimated by the method of McComas and Briscoe [1980]. They took the number of independent

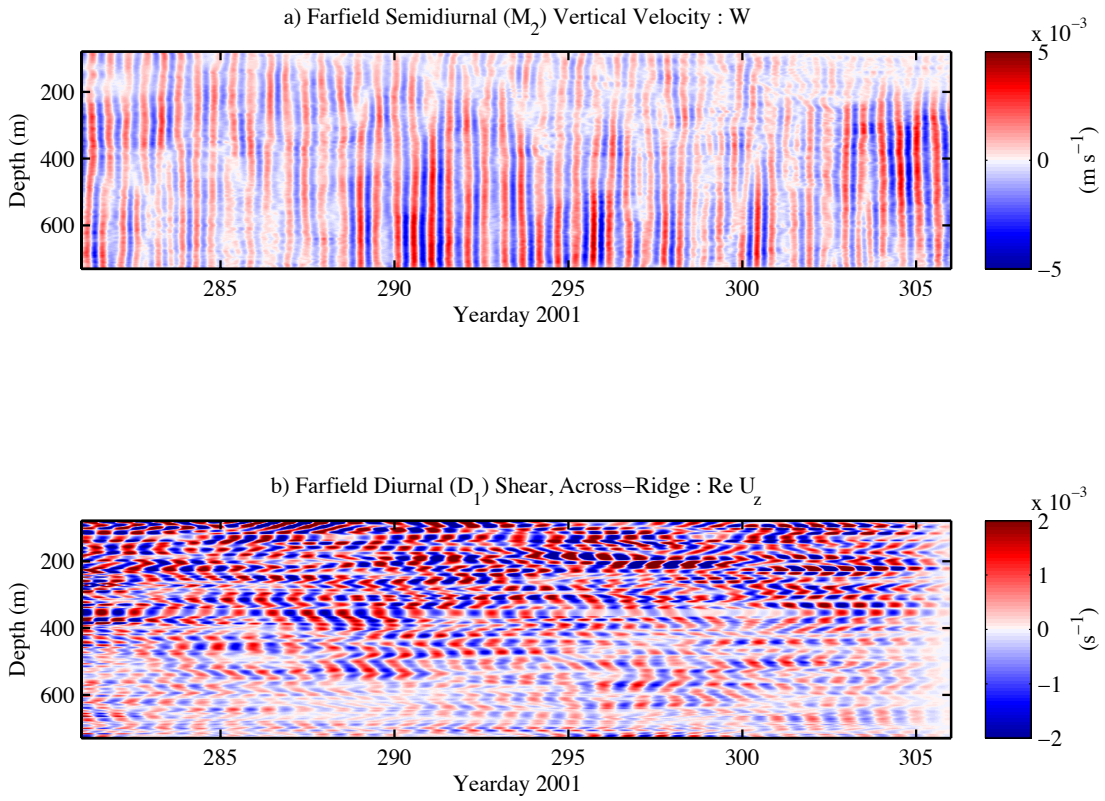

Figure 2.20: HOME Farfield: a) M_2 Vertical Velocity and b) D_1 Across-Ridge Shear.

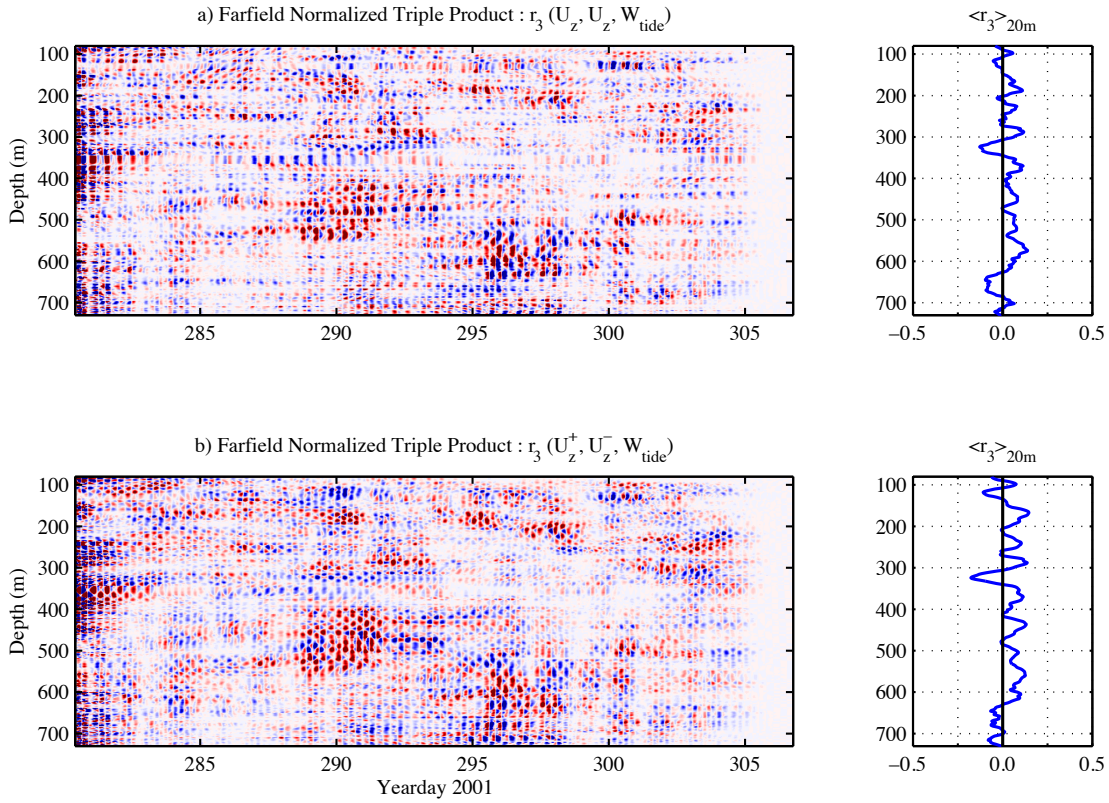

Figure 2.21: HOME Farfield: Triple Product of D_1 Shears and M_2 Vertical Velocity. a) Unfiltered D_1 Shears. b) Prefiltered Shears. As in Fig. 2.21 but repeated for the Farfield site, 430 km from Kaena Ridge. No significant resonant interactions are visible.

measurements of a Gaussian wavefield to be the same as the number of wave periods contained in a given record. The lowest frequency of interest sets the appropriate period.

The FLIP data span 43.5 M_2 tidal periods before the interruption on day 280 (63.2 tidal periods in total). Since the subharmonic waves have a period approximately twice as long as a tidal period, we might conclude that we have $n_{\mathrm{dof}} = 43$ (or 63) by time averaging alone.

By a similar argument, taking vertical averages would also increase the statistical stability. For subharmonic waves with characteristic vertical wavelength of $\mathcal{O}(100$ m), each depth range in our calculation contains 4 wavelengths for a factor of 4 in independent measurements (more in the upper range if WKB scaling for vertical wavelength holds). Using the thresholds given by Elgar and Guza [1988] and discussed following the definition of bicoherence (2.12), a cutoff for zero bicoherence at the 95% confidence level would be $b_{95\%} = \sqrt{6/(43 \cdot 4)} = 0.19$, with $b_{99\%} = \sqrt{9.2/(43 \cdot 4)} = 0.23$.

However, inspection of the shear record reveals that waves in the diurnal band exhibit clear group structure, reducing the independence of successive measurements (or simultaneous measurements at neighboring depths). A conservative estimate of the dominant group scales would be about 3 wavelengths in the vertical and 5 in time. This reduction in independence is partly offset by the 3×3 convolution applied to the bispectral and power spectral estimators. If the size of groups is used instead of the size of waves to determine the effective n_{dof}, then much stricter requirements for significant nonzero bicoherence are set at $b_{95\%} = \sqrt{6.4/(43/5 \cdot 4/3 \cdot 3)} = 0.42$ and $b_{99\%} = 0.52$.

We used a Monte Carlo method to compare these opposing views of statistical independence. Bicoherence estimates were recomputed for both prefiltered and unfiltered data in the lower depth range, 300–700 m, using the same methods as in Sections 2.5 and 2.6. Fourier coefficients at each frequency were multiplied by random phase-shifts $\exp(2\pi i \cdot \theta)$, where θ is uniformly distributed on $[0, 1)$. After 5000 trials, sample thresholds for zero bicoherence were determined for the 90%, 95%, and 99% levels at each frequency pair (ω_1, ω_2).

Figure 2.22 shows the results for prefiltered, random-phase data, plotted on the same color scale as previous bicoherence estimates. The largest (least-precise) threshold appears at a peak near the inertial frequency f in downgoing energy (ω^-) and between the subharmonic and inertial frequencies in upward (ω^+) energy. Maximum threshold values for prefiltered zero-bicoherence threshold are $b_{90\%} = 0.47$, $b_{95\%} = 0.51$ $b_{99\%} = 0.55$. The peaks do not overlap significantly with the "true" prefiltered bicoherence peak of Fig. 2.15, which exceeds 0.60 and thereby exceeds the 99% threshold for statistical significance.

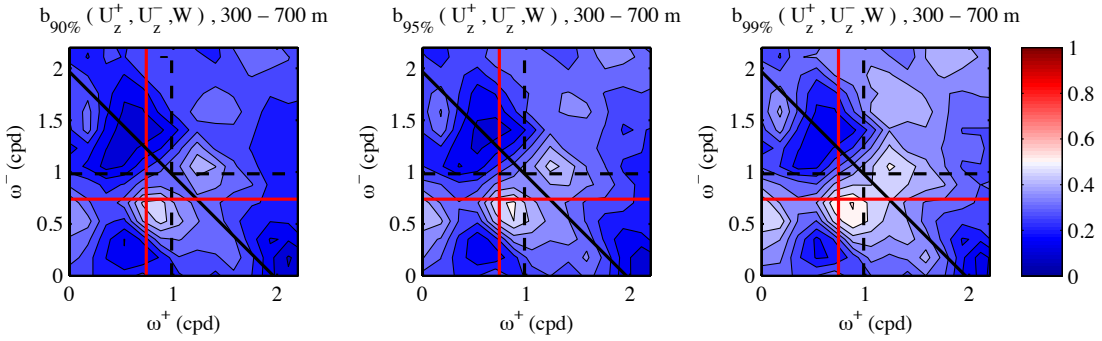

Figure 2.22: Prefiltered Zero-Bicoherence Thresholds at the 90%, 95%, and 99% Confidence Levels Estimated From 1000 Monte Carlo Trials. Thresholds are estimated using prefiltered data from the 300–700 m depth range. Fourier coefficients at each frequency have been multiplied by random phase shifts $\exp(2\pi i \cdot \theta)$, where θ is uniformly distributed on $[0, 1)$. The largest (least-precise) thresholds appear near the inertial frequency f in downgoing frequencies (ω^-) and between the subharmonic and inertial frequencies in upward (ω^+). This peak threshold does not overlap significantly with the "true" prefiltered bicoherence peak of Fig. 2.15. Maximum values are $b_{90\%} = 0.47$, $b_{95\%} = 0.51$ $b_{99\%} = 0.55$, suggesting that the effective degrees of freedom near these frequencies are relatively few and are set by the scales of diurnal and near-inertial wave groups rather than individual waves.

By contrast, the unfiltered random-phase bicoherence, shown in Figure 2.23, has an elevated threshold around around a pair of frequencies which are slightly higher than diurnal (D_1) and thus with bifrequency slightly higher than (M_2). Maximum threshold values are slightly higher than for the prefiltered case, at $b_{90\%} = 0.50$, $b_{95\%} = 0.52$ $b_{99\%} = 0.57$. The peak threshold area has noticeable overlap with the peak of the "true" unfiltered bicoherence of Figure 2.11. Thus only a narrow part of the bicoherence peak at (D_1, D_1, M_2) retains 99% significance.

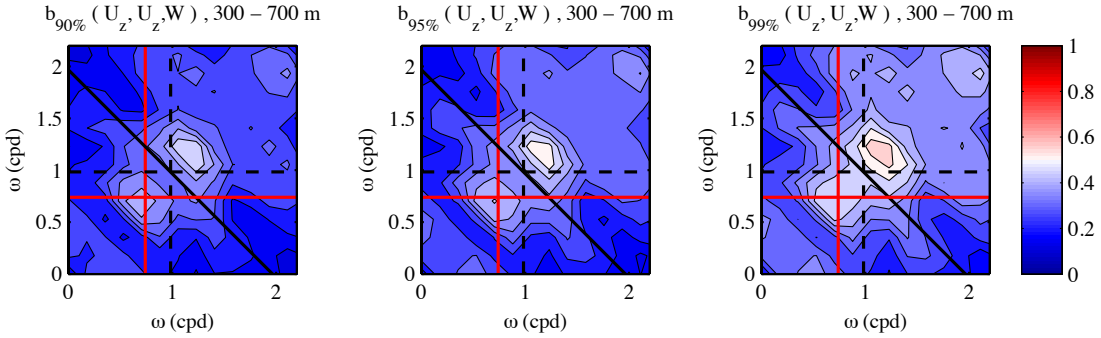

Figure 2.23: Unfiltered Zero-Bicoherence Thresholds at the 90%, 95%, and 99% Confidence Levels Estimated From 1000 Monte Carlo Trials. As in Fig. 2.22, but using unfiltered shear records. The largest (least-precise) thresholds appears around around a pair of frequencies which are slightly higher than diurnal (D_1) and which have bifrequency slightly higher than (M_2). There is significant overlap with the bicoherence peak of the "true" unfiltered bicoherence of Fig. 2.11. Maximum values are $b_{90\%} = 0.50$, $b_{95\%} = 0.52$ $b_{99\%} = 0.57$, suggesting that the effective degrees of freedom near these frequencies are relatively few and are set by the scales of diurnal wave groups rather than individual waves.

In both the filtered and unfiltered cases, the zero-bicoherence thresholds are elevated near pairs of frequencies which have strongly group-like structure. The peak values are well-predicted by estimating of degrees of freedom from the scales of the wave groups rather than the individual waves. This implies that the effective degrees of freedom are relatively few, even with a record spanning multiple vertical wavelengths and more than 20 subharmonic period. The prefiltering step thus becomes useful for enhancing the separation between true bicoherence and spurious signals (in addition to identifying interacting members).

Chapter 3

Energy Transfer from High Shear Low-Frequency Internal Waves to High Frequencies

3.1 Introduction

Internal wave energy in the open ocean tends to be concentrated near the inertial end of the spectrum, a fact represented by the well-known inertial cusp in the Garrett-Munk spectrum [Garrett and Munk, 1972]. As a consequence of their low aspect ratios due to the internal wave dispersion relationship, these frequencies are also associated with most of the shear in the ocean.

Although low-frequency internal waves are primarily associated with wind forcing, they are also generated by a variety of other mechanisms. These include, but are not restricted to, lee-wave generation, bottom scattering, and resonant wave-wave interactions. In particular, studies of nonlinear energy transfers in the internal wave continuum have suggested that Parametric Subharmonic Instability (PSI), a resonant interaction which transfers energy from waves with frequencies $2f$–$4f$ to approximately half their frequency, would support enhanced near-inertial energy even in the absence of wind forcing [Olbers, 1976, McComas and Bretherton, 1977, McComas and Müller, 1981b]. Several recent studies have specifically

considered PSI of the semidiurnal tide as a likely source of near-diurnal energy [Hibiya et al., 2002, MacKinnon and Winters, 2005, Carter and Gregg, 2006, Alford et al., 2007, Sun and Pinkel, 2011]. Thus in addition to wind energy, a significant amount of the tidal energy available for mixing may also pass through low frequencies before it reaches the rest of the internal wave spectrum.

Further nonlinear interactions may play a role in transferring energy away from these subtidal frequencies. Due to the lower limit imposed by the inertial frequency, the direction of energy transfer must be from low to high frequencies. Induced Diffusion (ID) is the canonical resonant interaction which connects the low- and high-frequency ends of the spectrum. As originally described by McComas and Bretherton [1977], ID is an interaction between two high-frequency, small-scale waves and a much-lower frequency, large-scale wave, as diagrammed in Figure 3.1. Numerical evaluation of interaction rates have found that the high frequency portion of the GM spectrum is nearly in equilibrium with respect to ID, with the most highly scale-separated interactions being the most active [Olbers, 1976, McComas and Müller, 1981a,b, Müller et al., 1986]. As the scale separation increases between the high frequency and low frequency waves, the interaction begins to resemble a random shift of wave action from one high frequency wave to a close neighbor in frequency-wavenumber space, with a net diffusive effect.

Resonant interaction theory is exact only in the weakly non-linear limit. As an alternative, eikonal methods [Henyey and Pomphrey, 1983, Henyey et al., 1986, Broutman and Young, 1986] avoid the amplitude restriction on the low-frequency shears. Small-scale "test" waves are sent through a "background" shear field which varies slowly on the scales of the test waves. The individual test waves retain their identity as they pass through the background field and are assumed not to interact with one another. In contrast to resonant interaction theory, the eikonal approach does not explicitly conserve energy and momentum. Instead, changes to the test waves are assumed to be balanced by small changes to the large scale wavefield.

The present study examines nonlinear energy transfers between low- and high-frequency waves using data collected aboard the Research Platform *FLIP* during 2001–2002 as part of the Hawaii Ocean Mixing Experiment (HOME). The

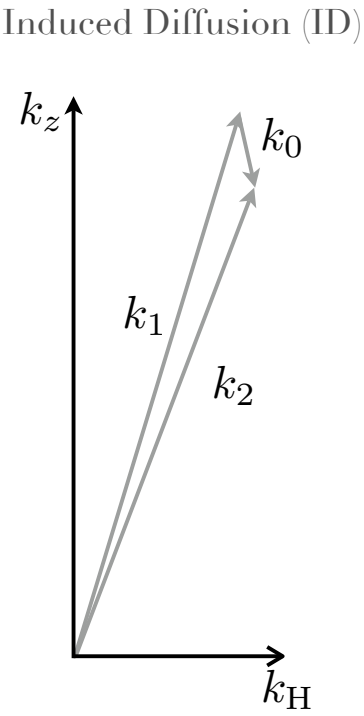

Figure 3.1: Resonant Triad for Induced Diffusion. The wave vectors represent a low-frequency wave $\mathbf{k_0}$ and a pair of high frequency waves $\mathbf{k_1}$ and $\mathbf{k_2}$. The triad of waves satisfies both a wavenumber resonance condition $\mathbf{k}_0 + \mathbf{k}_1 = \mathbf{k}_2$ and a frequency resonance condition $\omega(\mathbf{k}_0) + \omega(\mathbf{k}_1) = \omega(\mathbf{k}_2)$, so that energy is exchanged among the members of the triad. The high frequency waves in Induced Diffusion have much larger wavenumber, and hence much smaller spatial scales, than the low frequency wave. In the limit of large scale separation, the high frequency wavenumbers are nearly identical.

data from *FLIP* combine CTD profiles of density and temperature measured at 4-min intervals with Doppler sonar horizontal velocities with 2-m resolution. Energy transfers between regions of frequency-wavenumber space are identified and quantified by bispectral analysis. An attempt is made to determine which of the theoretical interactions between low- and high-frequency portions of the internal wave spectrum, if any, are supported by the observations. Net energy transfer rates to high frequency are found to be comparable in magnitude to measurements of kinetic energy dissipation by turbulence.

3.2 Instruments and Data

As part of the Hawaii Ocean Mixing Experiment (HOME) , the Research Platform *FLIP* was deployed near Kaena Ridge, one of the most energetic tidal conversion sites identified in HOME [Rudnick et al., 2003, Rainville and Pinkel, 2006]. Two locations, shown in Figure 3.2, were occupied in successive years. During the Fall 2001 Farfield component, *FLIP* was moored 430 km to the south-south-west of Kaena Ridge, in the approximate path of an M_2 tidal beam emanating from the Ridge. In the HOME Nearfield, 2002, *FLIP* was moored on the southwest shoulder of Kaena Ridge in 1100 m of water.

Data collection during each six-week deployment spanned roughly 30 days, enough to observe a pair of fortnightly cycles. Figure 3.3 shows a schematic view of the instrumentation. A pair of tandem profiling Seabird SBE11 CTDs recorded 9400 profiles of temperature and salinity in the Farfield, and more than 11000 profiles in the Nearfield, at 4-minute intervals. Depth coverage was approximately 80 to 800 m. Vertical velocities were inferred from the motion of isopycnals, as measured by the CTDs. Horizontal velocities were recorded by the up/down-looking *Deep-8* Doppler sonar, located at a depth of 400 m during both deployments. Vertical resolutions were 2 m for CTD data and 4 m for horizontal velocities. The reader is referred to Rainville and Pinkel [2006] for a more detailed discussion of the instruments and deployment.

A gap in sonar coverage exists in a 10 m range around the 400 m location

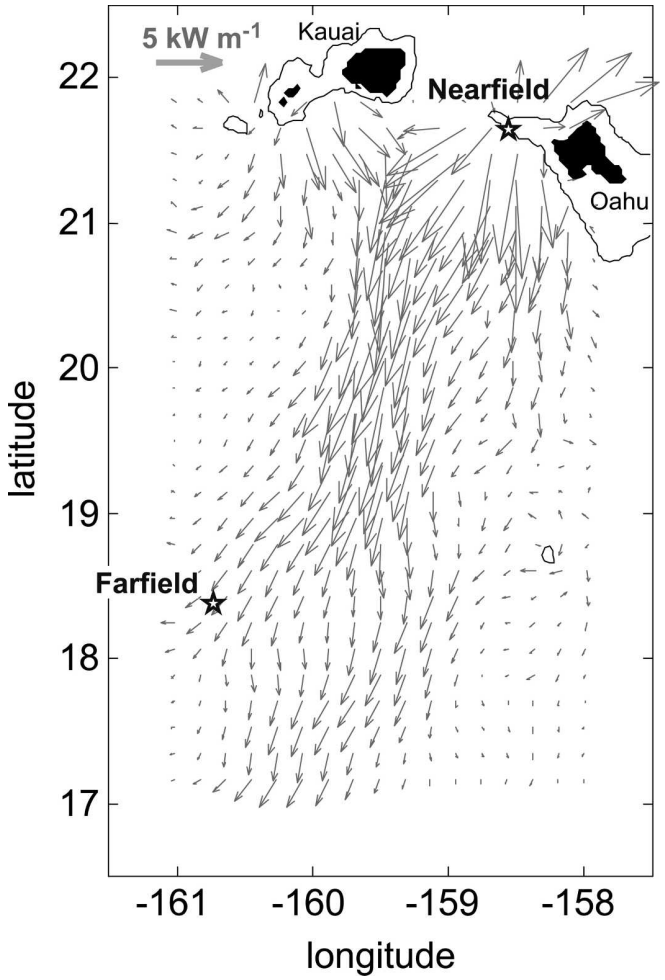

Figure 3.2: Deployment of the Research Platform *FLIP* in 2001–2002 [Rainville and Pinkel, 2006]. As part of the Hawaii Ocean Mixing Experiment, *FLIP* was moored at two locations near Kaena Ridge, Hawaii. During the 2002 Farfield component, the measurement location was approximately 430 km to the southwest of the the ridge crest, in the approximate path of an M_2 tidal beam (model fluxes are shown by the arrows). The 2002 Nearfield component placed *FLIP* on the shoulder of Kaena Ridge in approximately 1100 m of water, in a location intersecting the southward-propagating ray emanating from the north ridge.

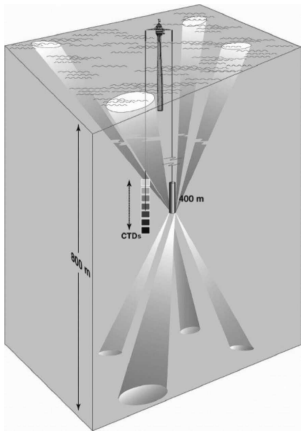

Figure 3.3: Schematic of R/P *FLIP* Instrumentation during HOME, 2001–2002. Tandem Seabird SBE11 CTDs profiled down to approximately 800 m once every 4 minutes with approximately 2 m resolution. The *Deep-8* Doppler sonar recorded horizontal velocities with approximately 4 m vertical resolution. Vertical velocities were inferred from the motion of isopycnals as measured by the CTDs. More than 11000 profiles were collected during the Nearfield and more than 9000 during the Farfield.

of the *Deep-8*. The resulting discontinuity is easily visible in the vertical shears. Data collection in the Nearfield was briefly interrupted around day 280, when a CTD collided with the *Deep-8*. Profiling was resumed with a reduced $\sim$ 700-m maximum depth.

Acoustic reflections from the sea surface and bottom contaminate the sonar record. To minimize the effect of these discontinuities, Eulerian coordinates are used throughout. This is different from the convention of Sun and Pinkel [2011], which uses semi-Lagrangian (isopycnal) coordinates to reduce the effects of vertical advection by the semidiurnal tide. Here, Eulerian coordinates are chosen to avoid spreading the scars in the sonar data to adjacent depths; this would occur if the Eulerian sonar data were transformed to semi-Lagrangian (isopycnal) coordinates and the isopycnals were to pass through the affected depths. Velocities are interpolated for visual presentation, but the affected depths are discarded whenever depth averages are formed.

The data are presented using a WKB-scaled vertical coordinate, which is defined using cruise-averaged profiles of relative background stratification $N(z)/N_0$.

The base stratification N_0 is chosen so that the new vertical coordinate, z_{WKB}, spans the same profiling range before and after stretching.

Velocity and shear are according to linear theory:

$$w = w_0\sqrt{\frac{N}{N_0}}, \quad (u,v) = (u_0,v_0)\sqrt{\frac{N_0}{N}}, \quad (u_z,v_z) = \left(\frac{N_0}{N}\right)^{3/2}(u_{z0},v_{z0}).$$

As an exception to this convention, the Nearfield shears vary nearly as N, so a scaling of $(N_0/N)^1$ is applied instead of the theoretical $(N_0/N)^{3/2}$.

For brevity, multiples of the diurnal frequency, D_1, are denoted by D_n, with n being the nth multiple. This convention is also used to refer to data which has been bandpassed around the indicated center frequency.

Nearfield

The HOME Nearfield site, at 21.68°N, 158.63°W, is on the south-west shoulder of the ridge and intersects a tidal beam emanating upward from the north-east edge [Rainville and Pinkel, 2006]. Semidiurnal and diurnal motions show distinct features related to the nearby tidal generation and subsequent nonlinear interactions. To highlight these differences, data are frequency bandpassed around the D_1 and D_2 frequencies, with remaining motions residing in a "high frequency" band (HF). The passband for D_1 is 0.6–1.2 cpd and includes the local inertial frequency; D_2 spans 1.6–3 cpd. HF only includes frequencies above 6 cpd, in order to avoid leakage from the semidiurnal tides in the D_2 band and their D_4 harmonics. A high-frequency cutoff at 48 cpd is also applied to reduce aliasing for visual presentation. All filters are a bidirectional (zero-phase), 8th-order Bessel-derived filter.

The D_2 and D_1 bands are presented in Figure 3.4. D_2 velocities exhibit the predominantly long vertical scale motions of the low-mode semidiurnal tide, as seen in vertical velocity W in the upper panel. Approximately two weeks of the total record are shown. A slight backward slant to the phase lines is associated with upward D_2 energy propagation from the ridge. One spring tide is just ending on day 265, at the beginning of the record; another reaches its peak near day 277.

Vertical shears emphasize the high mode waves found in the D_1 band, as shown in the lower panel of Fig. 3.4. D_1 sources include wind-driven near-inertial

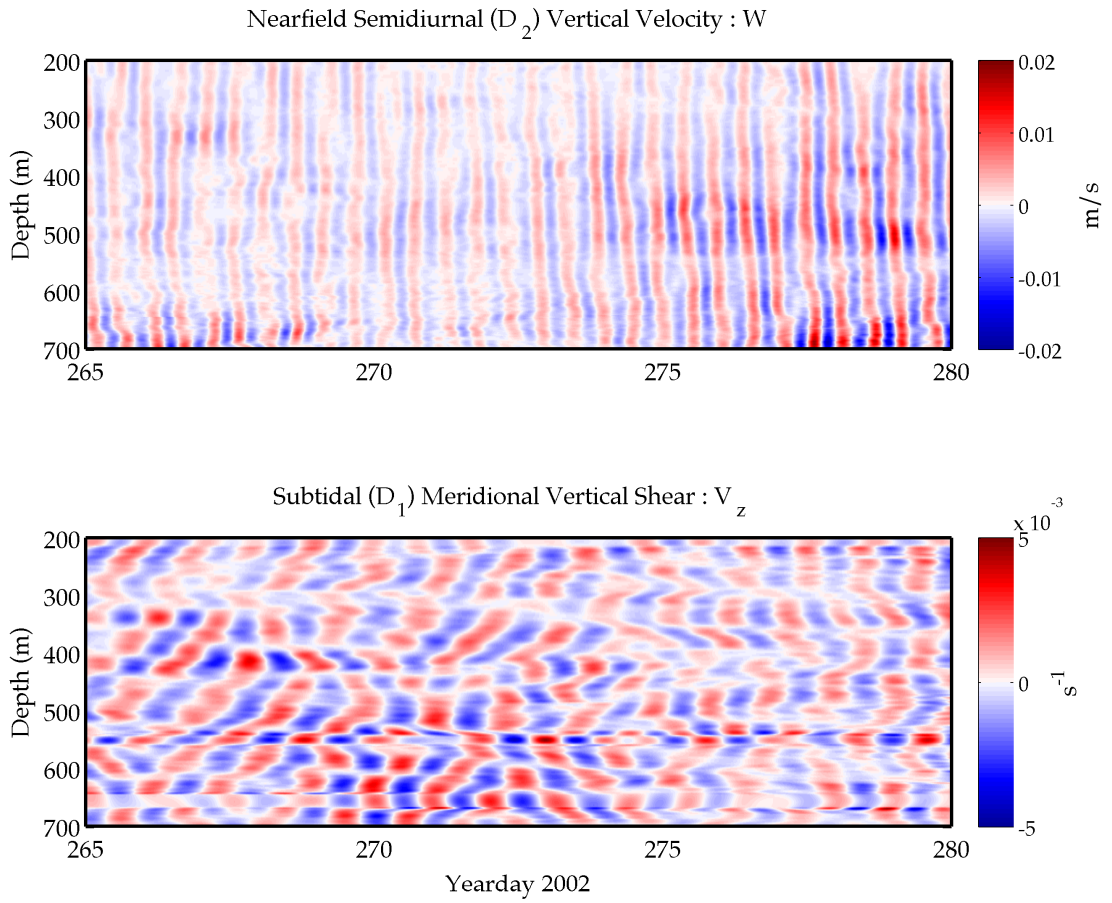

Figure 3.4: HOME Nearfield: Low Frequency Wavefields. Top) Semidiurnal (D_2) Vertical Velocity. Long vertical scales and predominantly downward phase propagation, associated with upward energy propagation, are the main features of the record. The end of one spring tide is visible around day 265, and a new one peaks around day 277. Bottom) Subtidal (D_1) Meridional Vertical Shear. The record is WKB-stretched to show the regular vertical scale, $\approx$ 100 m, which appears to dominate the shear. The near-diurnal frequency is prevalent. Both upward and downward phase propagation can be seen.

motions and the K_1 and O_1 tides. PSI-generated subharmonics of the semidiurnal internal tide are also found in the lower half of the water column, as reported by Carter and Gregg [2006] and Sun and Pinkel [2011]. The PSI waves have a characteristic vertical scale of about 100 m, and can seen propagating both upward and downward from mid depths, as indicated by the cross-hatched or 'X' pattern of wave crests seen below 400 m on days 270–275. A fortnightly cycle in the D_1 shears lags the D_2 spring tide by 4–7 days, consistent with PSI growth timescales predicted by Young et al. [2008].

HF motions above 6 cpd are presented in Figure 3.5. Moderate to long-wavelength motions are visible in both the vertical component w (upper panel) and in the horizontal component (v shown in the lower panel). Hints of grouplike structures are visible in both w and v. w emphasizes slightly higher frequencies and longer vertical scales than v. This can be explained by the increasing aspect ratio with frequency which results from the dispersion relationship for internal waves.

Farfield

As the semidiurnal internal tide propagates away from the generation site, it assumes a more "modal" structure. By the time they reach the Farfield site at 18.39°N, 160.70°W, the clear downward propagation of phase lines seen in the Nearfield is no longer evident. Figure 3.6 (top) shows a sample of vertical velocities. Meanwhile, in strong contrast to the "monochromatic" shear field in the Nearfield, the Farfield D_1 shears (Fig. 3.6, bottom) display a mix of vertical scales, resulting in an irregular vertical pattern rather than the regular 'X' pattern of the PSI subharmonic waves. The D_2 and D_1 wavefields in the Farfield may be taken as far more typical cases for the open ocean, as compared to the highly anisotropic semidiurnal and monochromatic diurnal fields in the Nearfield.

High frequency wavefields, shown in Fig. 3.7, emphasize very long vertical scales rather than the distinct grouplike patches seen in the Nearfield. Some group propagation is still visible in high-frequency w, but very little in high-frequency v. However, v displays a considerable amount of variance at very small vertical scales

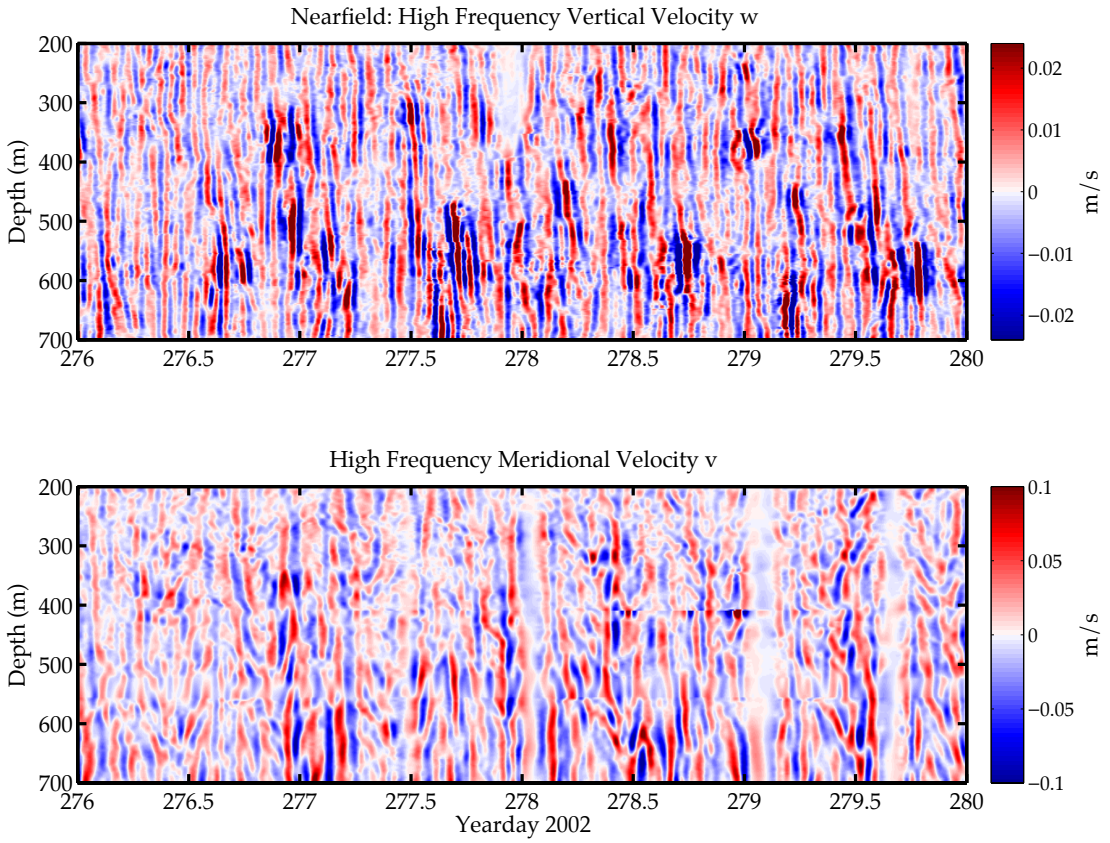

Figure 3.5: HOME Nearfield: High Frequency Wavefields. Top) High Frequency ($> D_6$) Vertical Velocity. Wave groups with long vertical scales and possibly upward group propagation are visible. Bottom) High Frequency Meridional Velocity. Somewhat lower frequencies and shorter wavelengths are emphasized by v, as compared to w. Grouplike structures are still visible.

as well as at the long scales.

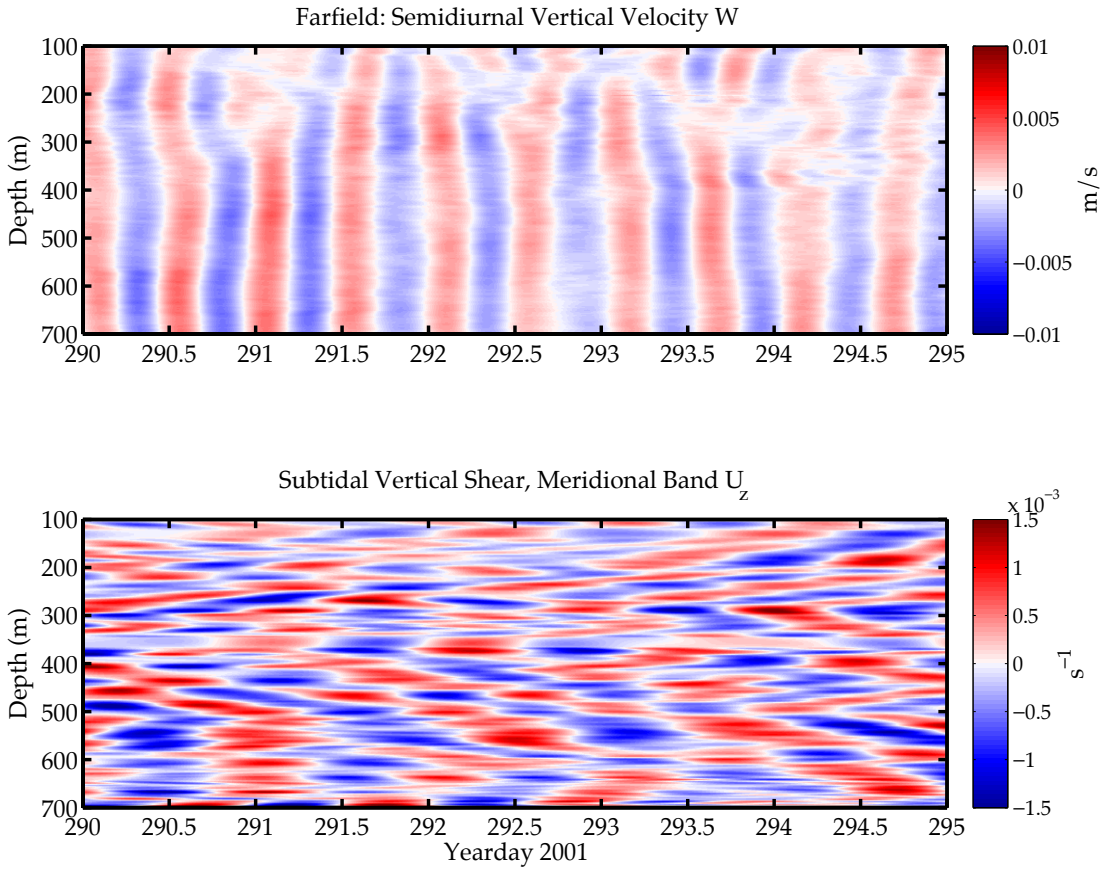

Figure 3.6: HOME Farfield: Low Frequency Wavefields. Top) Semidiurnal (D_2) Vertical Velocity. As in Fig. 3.4, but for the Farfield. Long vertical scales are still visible in W, but absent is the clear downward phase (upward energy) propagation seen in the Nearfield. Bottom) Subtidal (D_1) Meridional Vertical Shear. Short vertical scales are emphasized as before, but no single vertical length scale stands out even after WKB stretching.

3.3 Nonlinear energy transfers

The goal of this section is to investigate nonlinear interactions between low-frequency shears (Fig. 3.6, bottom) and high-frequency motions (Fig. 3.7). An effort is made to avoid attachment to any particular theory or expectation of those interactions. Instead, an attempt is made to identify the participating members of any interactions and quantify the nonlinear energy transfer rate.

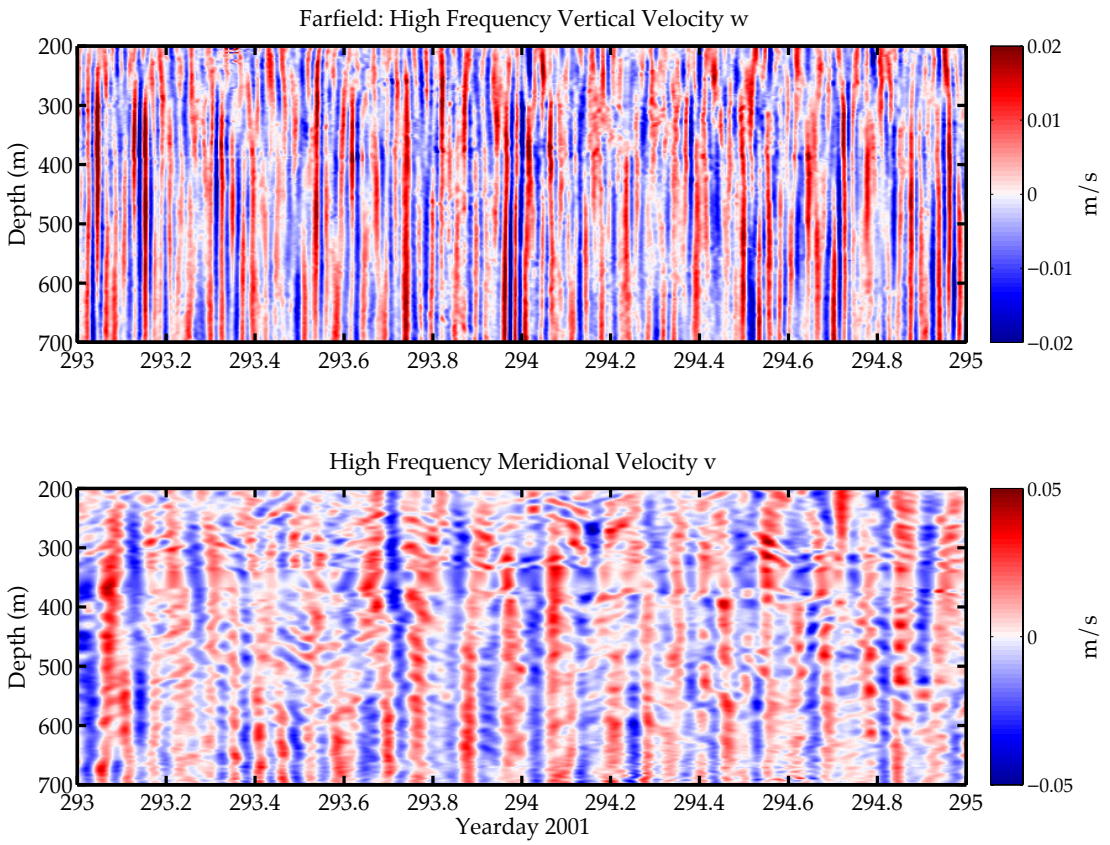

Figure 3.7: HOME Farfield: High Frequency Wavefields. Top) High Frequency ($> D_6$) Vertical Velocity. Wave groups with long vertical scales and possibly upward group propagation are visible. Bottom) High Frequency Meridional Velocity. Somewhat lower frequencies and shorter wavelengths are emphasized by v, as compared to w. Grouplike structures are still somewhat visible in w, less so in v.

3.3.1 Stress-shear triple products

A traditional approach from the theory of turbulent flows is to take a Reynolds decomposition [Tennekes and Lumley, 1972], separating velocities $\tilde{u}, \tilde{w}$ into a "mean flow" and "fluctuations,"

$$\tilde{u_i} = U_i + u_i, \quad i = 1, 2, 3, \tag{3.1}$$

where $\bar{U_i} \equiv 0$.

For wave fields, a modified approach has been taken which associates wave energy with the "mean flow" and turbulent motions with the "fluctuations" [Osborn, 1980]. Gargett and Holloway [1984] point out, however, that it may not be clear how to make such a scale-separation of the velocity field. Following their approach, an energy transfer expression for mixed wave/turbulence motions is derived with making an explicit separation.

The kinetic energy equation is used under the Boussinesq approximation,

$$\frac{\partial}{\partial t}\left(\frac{1}{2}u_i^2\right) + u_i u_j \frac{\partial u_i}{\partial x_j} = -\frac{1}{\rho_0} u_i \frac{\partial p}{\partial x_i} + \nu \frac{\partial}{\partial x_j}\left(u_i\left(\frac{\partial u_i}{\partial x_j} + \frac{\partial u_j}{\partial x_i}\right)\right) - \frac{g}{\rho_0}\rho' w - \frac{\nu}{2}\left(\frac{\partial u_i}{\partial x_j} + \frac{\partial u_j}{\partial x_i}\right)^2, \tag{3.2}$$

where $i = 1, 2, 3$ and $u_3 = w$, ν is the kinematic viscosity, and ρ' is the perturbation density.

Assuming a quasi-steady-state, the time averaged equation is

$$\left\langle u_i u_j \frac{\partial u_i}{\partial x_j} \right\rangle = -\frac{1}{\rho_0}\frac{\partial}{\partial x_i}\left\langle u_i p \right\rangle + \nu \frac{\partial}{\partial x_j}\left\langle u_i \left(\frac{\partial u_i}{\partial x_j} + \frac{\partial u_j}{\partial x_i}\right)\right\rangle - \frac{g}{\rho_0}\left\langle \rho' w \right\rangle - \varepsilon, \tag{3.3}$$

$$\varepsilon = \frac{\nu}{2}\left\langle \left(\frac{\partial u_i}{\partial x_j} + \frac{\partial u_j}{\partial x_i}\right)^2 \right\rangle.$$

Gargett and Holloway [1984] suggest on prior observational grounds that the first term, the divergence of the pressure-velocity correlation, and the third term, the pressure work, are small. The second term is a viscous transport term, which is ordinarily negligible compared to ε, the transport due to Reynolds stresses Tennekes and Lumley [1972]. Finally, since the horizontal stress-shear terms in ε

are unknown, they are omitted (equivalent to an assumption of horizontal homogeneity in the internal wavefield). Thus Gargett and Holloway [1984] find a leading order balance between dissipation ε and stress-shear triple products

$$\varepsilon \approx -\left\langle u_i w \frac{du_i}{dz} \right\rangle, \quad i = 1, 2. \tag{3.4}$$

The present study focuses primarily on triple correlations between D_1 shears, indicated by the capital dU_i/dz, and fluctuations in u_i, w with significantly higher frequency. Thus a new symbol, ε_*, is introduced and defined as the energy transfer rate from low-frequency shears due to high frequency fluctuations,

$$\varepsilon_* \approx -\left\langle u_i w \frac{dU_i}{dz} \right\rangle, \quad i = 1, 2. \tag{3.5}$$

Nearly all the shear variance in the observations is captured by taking only D_1. A clear separation between low and high frequencies is justified by excluding the D_2 band, since D_2 is already involved in a nonlinear energy transfer, via PSI, to D_1. Unlike the discussion of Duda and Jacobs [1998], which also investigates wave-wave interactions using shear-shear correlations, an explicit scale separation in wavenumber (where the fluctuations are assumed to have "turbulent" scales) is not also assumed.

As a measurement of the relative coupling of the three components in (3.5), a triple correlation r_3 is also defined. The energy transfers are normalized by the rms magnitudes of the multiplicands,

$$r_3(D_m, D_n) = \frac{\varepsilon_*(D_m, D_n)}{\left\{u^2(D_m) w^2(D_n) U_z^2(D_1)\right\}^{1/2}}. \tag{3.6}$$

3.3.2 Bispectral analysis

Wave frequencies which participate in resonant energy transfers may be identified using bispectral methods. Bispectra have been used to demonstrate nonlinear coupling in a variety of settings, including turbulent flows, [Kim and Powers, 1979] and surface gravity waves [Elgar and Guza, 1988]. Resonant internal wave interactions, in the form of parametric subharmonic instability of the semidiurnal internal tide [Carter and Gregg, 2006, Sun and Pinkel, 2011], have also been observed using a bispectral approach.

Here, the energy transfer term $-\langle uwU_z\rangle$ in (3.5) is expressed as a bispectral density, $B(\omega_u, \omega_w)$. This function quantifies the contribution of each pair of frequencies in u, w, respectively, to the energy transfer out of the low frequency shears.

To define the energy bispectrum, it is necessary to first define the Fourier series:

$$\begin{aligned} u(t) = \sum_{n=-N}^{N} U_n e^{i\omega_n t}, w(t) = \sum_{n=-N}^{N} W_n e^{i\omega_n t}, \\ U_z(t) = \sum_{n=-N}^{N} Z_n e^{i\omega_n t}, \quad \omega_n = 2\pi n/N. \end{aligned} \tag{3.7}$$

Then the triple product involving u in the brackets may be written in the form

$$uwU_z = \sum_m U_m e^{i\omega_m t} \sum_n W_n e^{i\omega_n t} \sum_p Z_p e^{i\omega_p t} \tag{3.8}$$

$$= \sum_m \sum_n \sum_p U_m W_n Z_p e^{i(\omega_m+\omega_n+\omega_p)t}. \tag{3.9}$$

Taking ensemble averages causes all terms to vanish except those fulfilling the frequency resonance condition $\omega_m + \omega_n + \omega_p = 0$, and thus the exponentials may be replaced by Kronecker deltas,

$$\langle uwU_z\rangle = \sum_m U_m e^{i\omega_m t} \sum_n W_n e^{i\omega_n t} \sum_p Z_p e^{i\omega_p t} \tag{3.10}$$

$$= \sum_m \sum_n \sum_p U_m W_n Z_p \delta(\omega_m + \omega_n + \omega_p). \tag{3.11}$$

For U_z containing only low frequency shears and u, w representing high frequency fluctuations, a pair of positive frequencies (ω_m, ω_n) can participate in one of two resonances

$$\omega_m < \omega_n : \quad \omega_m + \omega_p = \omega_n, \tag{3.12}$$

$$\omega_m > \omega_n : \quad \omega_m - \omega_p = \omega_n. \tag{3.13}$$

If ω_p is allowed to take on both positive and negative values, then the contribution to the energy transfer involving (ω_m, ω_n) can be written as the product of Fourier

coefficients $U_m Z_{m-n} W_n^*$, where the property that $W_{-n} = W_n^*$ has been used. The real-valued energy bispectrum can thus be defined as a function of positive frequencies (ω_m, ω_n) by taking the sum of contributions from (ω_m, ω_n) and $(-\omega_m, -\omega_n)$, and taking the negative of the expected value,

$$B(\omega_m, \omega_n) = -E\left[2 \cdot \Re(U_m W_n^* Z_{m-n})\right]. \tag{3.14}$$

As defined, the bispectral density represents resonant energy transfers from the low frequency shears to each pair of frequencies (ω_m, ω_n). In practice, the expected values are estimated by averaging over many realizations of U, W, Z.

The energy bispectrum will tend to have large values if the moduli of the Fourier coefficients are large. A normalized version, called the bicoherence, measures only the phase locking between wave frequencies and is useful for assessing the significance of bispectral estimates. Following Kim and Powers (1979) and Elgar and Guza (1980), the bicoherence is defined

$$b = \left\{ \frac{|B(\omega_m, \omega_n)|^2}{E\left[|U_m Z_{m-n}|^2\right] E\left[|W_n^*|^2\right]} \right\}^{1/2}, \tag{3.15}$$

with the property that $0 \leq b \leq 1$. The bicoherence only has meaning for bispectral estimates formed across multiple realizations; the bicoherence for a single realization is identically 1. Just as the energy bispectrum (3.14) is the bispectral representation of the triple covariance (3.5), the bicoherence is the counterpart to the triple correlation r_3 (3.6).

3.3.3 Nearfield energy transfers

The bispectral method is illustrated for the HOME Nearfield data. Time series for U, W, and U_z are divided into 10%-overlapping subrecords of length $1024 = 68.3$ hrs. A separate bispectral realization (3.14) is computed for each subrecord. Estimates from all Eulerian depths between 200 and 600 m are averaged together to form a depth-averaged bispectral estimate and a bicoherence.

Nearfield bispectral estimates are shown in Figure 3.8. Bispectral densities appear in the top panel, with bicoherence estimates shown below. Coordinate

axes (ω_u, ω_w) correspond to Fourier frequencies in U and W, respectively. The third frequency in each bispectral triad, corresponding to U_z, is implied for each coordinate pair according to (3.12)–(3.13). To improve statistical stability, a 5×5 gaussian filter has been applied to both the bispectrum and bicoherence.

Positive bispectral variance, shown in red in Fig. 3.8 (top), is concentrated near the line of symmetry ($\omega_u = \omega_w$). Upon closer inspection, it can be seen that bispectral peaks actually occur along two ridges closely paralleling ($\omega_u = \omega_w$). Bispectral variance decays rapidly with distance from the symmetry line. The locations of the peaks suggest that a multitude of resonant interactions are moving energy from low-frequencies to slightly-offset pairs of high frequencies.

Negative variance is also seen at low frequencies, particularly along a line $\omega_u = 2$. This is a result of the large semidiurnal horizontal velocities in the Nearfield. The sign of the bicoherence suggests that low frequency shear field may receive energy from low- frequency waves. However, the energy bispectrum near D_2 is not strictly valid, as the energy transfer expression (3.5) assumes a frequency separation between the shear field and interacting waves. Thus energy transfers implied in this region of the bispectrum should be taken cautiously.

The energy transfers roll off at very high frequencies. This may be explained by the Vaisala cutoff, which is near 68 cpd at mid-depth and gradually excludes more depths from the averaging process with increasing frequency.

After normalization to form the bicoherence, Fig. 3.8 (bottom), only the double ridge of peaks near ($\omega_u = \omega_w$) remains. This suggests that the positive energy transfers from low frequency shears to high frequency waves are a significant bispectral feature and not merely an statistical artifact of high spectral levels near the respective frequencies. By contrast, the negative bispectral values near $\omega_u = 2$ are not bicoherent and are not discussed further.

Energy transfer rate ε_* by frequency octave

To gain a more quantitative picture of the Nearfield energy transfers detected in Fig. 3.8, the bispectral densities are aggregated by frequency band. Bispectral densities are binned over boxed subdomains in the bispectral plane, shown

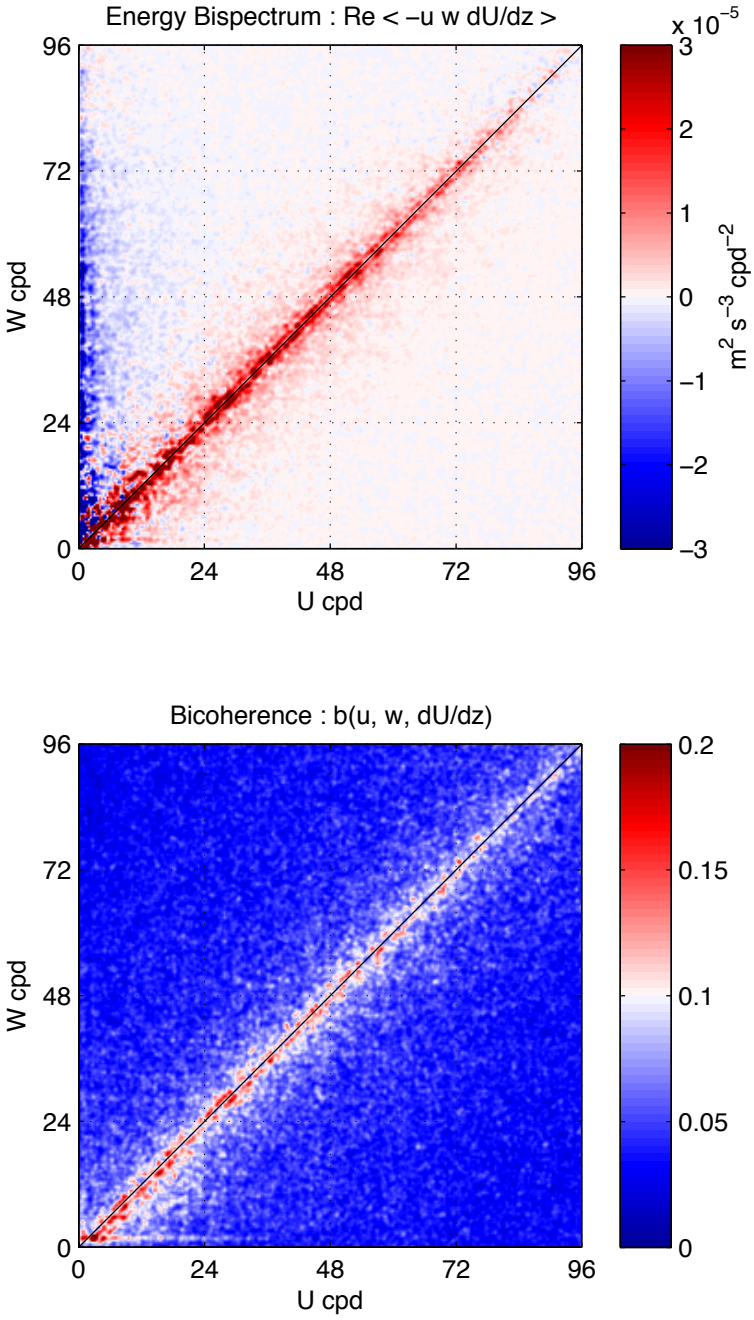

Figure 3.8: Nearfield: Bispectral estimates. Top) Bispectral density, $B(u, w, dU/dz)$. Coordinates are (ω_u, ω_w), corresponding to frequencies in u and w, respectively. The third frequency, corresponding to dU/dz, is implied. Positive bispectral variance is concentrated in a double ridge straddling the diagonal where $\omega_u = \omega_w$, implying positive energy transfers from dU/dz to u, w pairs which differ by a small frequency. Negative variance in the low-ω_u region, suggests that energy transfers may also work in the opposite direction. Right) Bicoherence estimate. After normalization it appears that only the positive energy transfers in the bispectral estimate are statistically significant.

on the left in Figure 3.9. The subdomains are centered on pairs of frequencies (D_m, D_n), and span one-octave intervals along each axis.

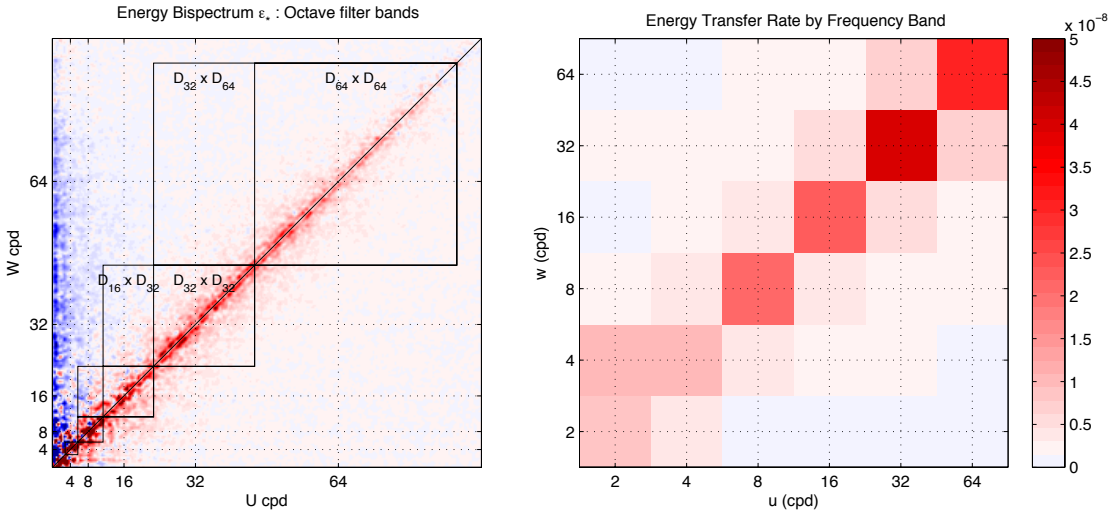

Figure 3.9: Nearfield: Bispectral energy transfers by octave. Left) Bispectral octave filter bands. Energy transfers are binned by the indicated boxes in bispectral space. Each region spans a single octave along each axis. Right) Energy transfer rate by frequency bands corresponding to the bins in the left figure. Units are W kg^{-1}. Axes are scaled by octave. Transfer rates are additive, with a total energy transfer of order 1×10^{-7} W kg^{-1}.

Figure 3.9 (right) shows the integrated energy transfer rates for each frequency subdomain, denoted by $\varepsilon_*(D_m, D_n)$. Note that the frequency axes are now scaled by octave. Rather than compute area integrals in bispectral space, the values for ε_* shown here are obtained by an equivalent time-domain algorithm. Both horizontal components in $-\langle uwU_z + vwV_z \rangle$ are included. (u, v) and w are bandpassed in octave bands around each center frequency, using a bidirectional 4th-order Butterworth filter (zero-phase, 8th-order equivalent). The passband for U_z is centered on 0.85 cpd to retain both D_1 and local f. The energy transfer rate

$$\varepsilon_*(D_m, D_n) = -\big\langle u(D_m)w(D_n)U_z(D_1) + v(D_m)w(D_n)V_z(D_1) \big\rangle \tag{3.16}$$

is then computed using the frequency-filtered versions of the multiplicands.

As before, energy transfers are concentrated in frequency bins along the main diagonal of Figure 3.9 (right); subsequent discussion will focus on these frequency bins only. The time-domain procedure allows the energy transfers to be

watched as they unfold in depth and time, with time-averaged profiles of the energy transfer rate shown in Figure 3.10 as a function of depth . Correlations, $r_3(z)$, are shown below. All profiles are vertically smoothed by a 60 m rectangular window.

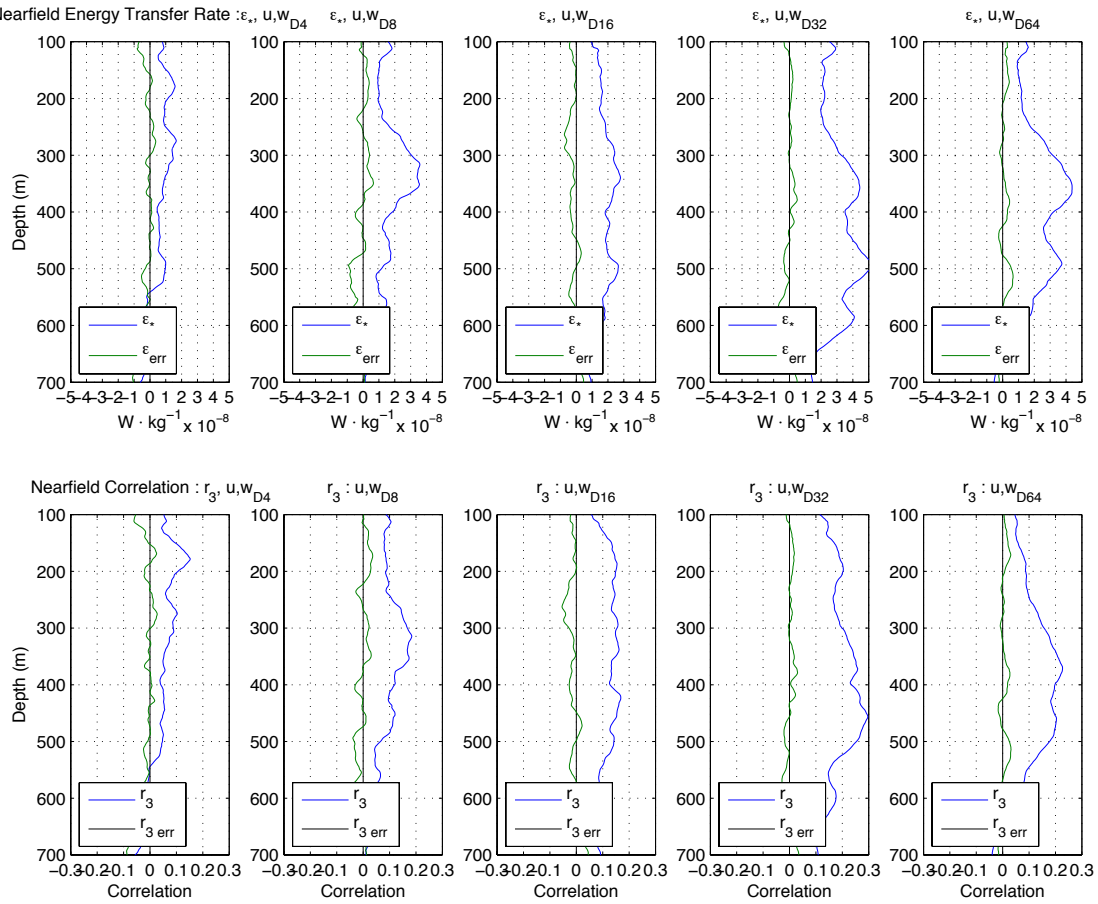

Figure 3.10: Nearfield: Energy Transfer Profiles. Above) Energy transfer rates $\varepsilon_* = -\langle uwU_z + vwV_z \rangle$ by frequency octave bin, as functions of depth. Error estimates (3.17) are plotted in green for reference. Significant energy transfers are found across a range of bands from D_8 to D_{64}. Maximum values of ε_* are found between 300 and 600 m in the D_{32} band, peaking at 6×10^{-8} W kg^{-1}. Below) Stress-shear correlations $r_3(z)$ (3.6), as functions of depth. In all cases, $r_3(z)$ appears to closely resemble $\varepsilon_*(z)$, up to a scaling factor. As before, error estimates are plotted in green.

ε_* and r_3 appear qualitatively similar in all bands. The largest energy transfers and correlations are found in the D_{32} band, where ε_* is exhibits a broad plateau between 300 and 620 m. ε_* peaking at 6×10^{-8} W kg^{-1} near 500 m, which is

also near the level where the biocoherent D_1 shears are largest. The corresponding peak correlation r_3 is 0.3. D_{64} also peaks broadly betwen 300 and 500 m depth. Dips in both bands near 430 m are due to the gap in the record near the position of the *Deep-8* sonar. A smaller peak is also observed in the D_8 band near 330 m depth. Total energy transfers in the D_{16} band are similar to the total D_8 transfers but are spread over a range of depths, with weak peaks at 330 and 500 m where strong peaks are observed in the neighboring bands.

An additional method of estimating measurement error in ε_* can be obtained from (3.16). Whereas $\langle uwU_z \rangle$ and $\langle vwV_z \rangle$ represent energy transfers in the equations of motion, $\langle uwV_z \rangle$ and $\langle vwU_z \rangle$ are not physically meaningful quantities but contain the same random noise. The resulting error estimate is defined as

$$\varepsilon_{\rm err}(D_m, D_n) = -\big\langle u(D_m)w(D_n)V_z(D_1) + v(D_m)w(D_n)U_z(D_1) \big\rangle. \tag{3.17}$$

Normalization by the convention of (3.6) yields a correlation error estimate, $r_{3\,\rm err}$. Both $\varepsilon_{\rm err}$ and $r_{3\,\rm err}$ are included in Fig. (3.9) for comparison. The reported estimates for ε_* and r_3 are significantly larger than the error estimates at nearly all depths for all frequency bands considered here.

The frequency rolloff seen in Fig. 3.8 is more clearly seen after depth averaging. Figure 3.11 shows the distribution of the energy transfers by frequency octave. The dashed lines pass through a set of small dots which correspond to the bands in the previous figure, as well as a set of intermediate points corresponding to octave bands with center frequencies falling between those of the indicated dots. Energy transfer rates, shown in the upper panel of Figure 3.11, increase nearly linearly with octave until a peak at about 4×10^{-8} W kg^{-1}, between the D_{32} and D_{64} bands. Above this peak frequency, the energy transfer rate rolls off steeply. Correlations, shown below, exhibit a similar trend, although the peak correlation is already reached in D_{32} and holds steady for a half-octave before rolling off.

Energy transfer rate ε_* by wavenumber octave

The waves which interact to produce the energy transfers seen in Fig. 3.8 are compatible with the frequency resonance condition for Induced Diffusion: a pair

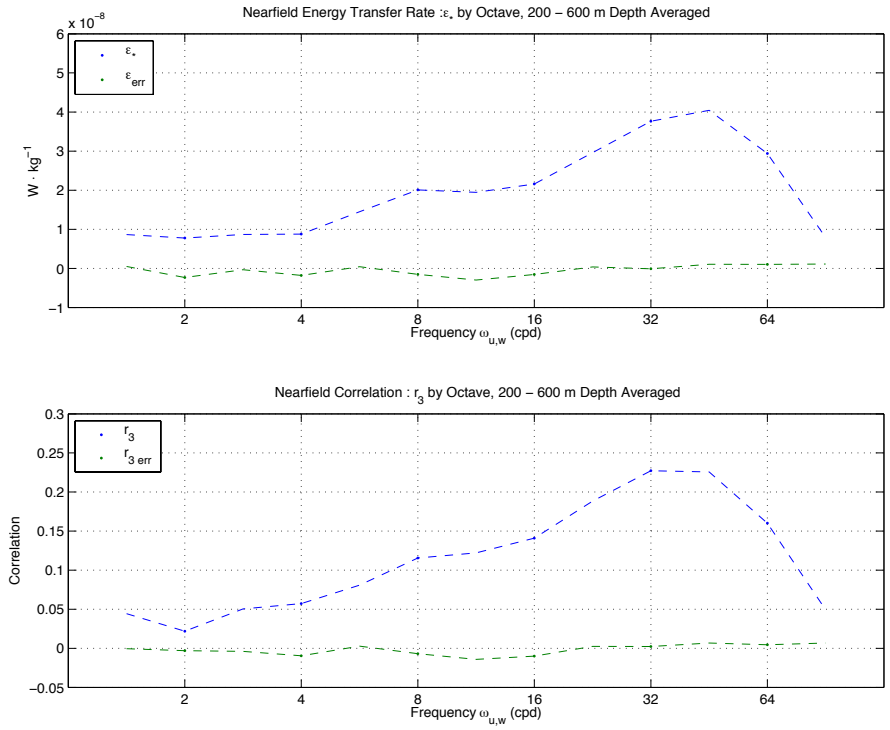

Figure 3.11: Nearfield: Depth-Averaged Energy Transfers by Octave. Above) Energy transfer rates $\varepsilon_* = -\langle uwU_z + vwV_z \rangle$ by frequency octave bin, depth-averaged. Plotted points are depth averages of the energy transfer profiles shown in Fig. 3.10. Dotted lines also pass through a set of points computed for intermediate octave bands. Error estimates (3.17) are plotted in green. Below) Stress-shear correlations $r_3(z)$ (3.6) by octave, depth-averaged. As before, error estimates are plotted in green.

of high frequency waves of similar, but not identical, frequency interact resonantly with a low frequency wave. The significant depth averages obtained in Fig. 3.11 also suggest that the waves are resonant in vertical wavenumber.

However, classical ID prescribes a specific arrangement for the wavenumber resonance: the high frequency waves have much larger wavenumbers, and hence much smaller spatial scales than the low frequency wave. This scale separation underlies the use of eikonal models of ID. As a corollary, the wave vectors for the high frequency waves are nearly identical in the limit of large scale separation.

Wavenumber resonances are examined using a bispectral approach analogous to the octave band method which was previously used to investigate frequency resonances. Energy transfer rates within each frequency band are computed as functions of u and w wavenumber. The wavenumber bands are, as before, arranged by octave. Here, the bands are centered on vertical wavelengths: 400 m, 200 m, 100 m, 50 m, 25 m, and 12.5 m in u and w.

Figure 3.12 plots the Nearfield ε_* per frequency band, as functions of u and v vertical wavelength.. The largest values of ε_* are seen in the D_{32} band, as previously observed. Common to all frequency bands which include significant energy transfers is an apparent resonance between the 400 m wavelength band in w and the 100 m wavelength in u. These are waves with the longest vertical wavelengths that can be resolved in w interacting with waves of significantly shorter wavelength in u, with scales similar to the dominant D_1 shear scale. There is also appreciable interaction between the immediately adjacent wavelength bands, so that 200 m w and 50 m u, for example, show relatively strong energy transfers as well. As before, the pattern of correlations closely mirrors the pattern of energy transfers.

The wavenumber-frequency analysis can be extended a step further. An attempt is made to distinguish between motions associated with wave energy going up (wave crests moving downward) and wave energy going down (phase lines moving upward). To accomplish this, the wavefields are 2-d Fourier transformed, and alternating quadrants in frequency-wavenumber space are collected to retain only motions with either downward or upward phase propagation, respectively.

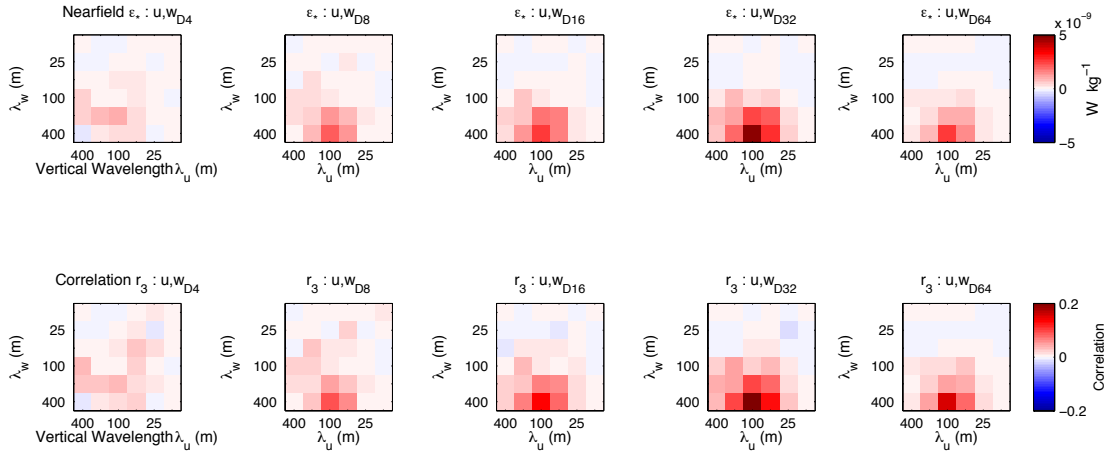

Figure 3.12: Nearfield: Energy transfer rate ε_* by wavenumber octave. As in Fig. 3.9 (right), but here the axes represent wavelengths. One map of wavenumber resonances is computed for each frequency band.

The up-down separated wavefields are then inverse transformed before frequency and wavenumber octave filtering.

By convention, waves with upward-propagating energy are denoted by positive vertical wavenumbers, while negative wavenumbers represent downward wave energy. Because each interaction involves a triad of waves, the up-down separation divides each wavenumber combination in Fig. 3.12 into 8 possible combinations of positive and negative wavenumbers.

Figure 3.13 shows ε_* separated for upward- and downward- propagating waves. Signed wavenumbers corresponding to u, w, respectively, are represented in the four distinct quadrants of each plot. The upper row of plots shows energy transfers involving upward-propagating shears U_z^+, while the lower row shows energy transfers for U_z^-.

Much greater variety in wavenumber triads is revealed in Fig. 3.13, relative to the unsigned versions of Fig. 3.12. As before, the 100-m u and 400-m w waves are generally most active when averaged over all quadrants of each plot. However, other interactions stand out in specific quadrants: e.g, the $(+50, +200)$ triad in the D_{32}, U_z^+ panel; the $(+200, +100)$ triad in D_{32}, U_z^-; and $(-100, +200)$ in D_{16}, U_z^+. It is noteworthy that some interactions appear in quadrants where u and w have opposite sign — this is a point that will be returned to.

The energy transfers seem to be biased toward upward-travelling w waves in the lower frequency panels D_4–D_{16}, gradually becoming more symmetric by D_{32}. The imbalance can explained by the predominance of upward-traveling energy, associated with the tidal generation at the ridge, in the semidiurnal frequency and its first several harmonics. Interactions involving downward shears U_z^- appear to be somewhat larger than those involving U_z^+ across all frequencies. This is consistent with the usual picture of generally more low frequency shear propagating downward in the oceans.

The wavenumber resonances implied in Figures 3.12–3.13 are unexpected in light of the theoretical predictions. Interactions found here seem to involve triads of waves with identifiable frequencies and wavenumbers. However, unlike classical Induced Diffusion, the high frequency members of the interactions remain distinct from one another even at the highest frequencies observed; Fig. 3.13 shows that some of the interacting high frequency waves have opposite signs of vertical propagation. Even more puzzling, the energy transfers involve high frequency waves which are not scale-separated from the background shears at all: u has vertical scales similar to U_z, and w has noticeably longer vertical scales noticeably than either u or U_z. This is incompatible with both the ID triad structure and the eikonal view of small test waves passing through a slowly varying background.

3.3.4 Farfield energy transfers

It is worth considering whether the surprising wavenumber resonances observed in the Nearfield of Kaena Ridge are representative of "typical" nonlinear interactions between low frequency shears and the high frequency portion of the internal wave spectrum. The HOME Farfield location provides a point of comparison, as a possibly more "typical" open ocean environment. While the Farfield site was chosen to coincide with the path of a propagating M_2 tidal beam, the tide is markedly less coherent at this location [Rainville and Pinkel, 2006], and shears are not strongly bicoherent subharmonics as found in the Nearfield. The key points of the analysis in the previous section are repeated using the HOME Farfield data, beginning with the separation of energy transfers by frequency-octave.

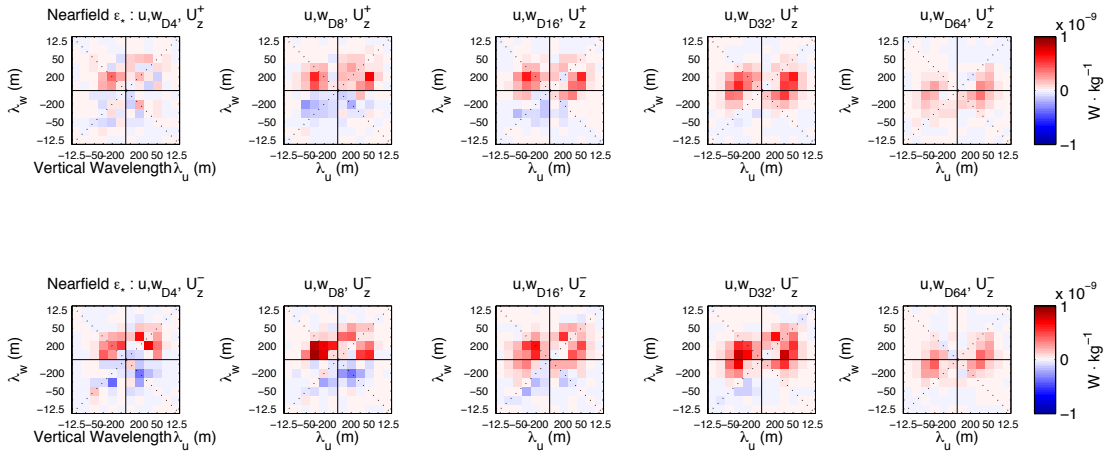

Figure 3.13: Nearfield: Energy transfer rate ε_* by wavenumber octave. As in Fig. 3.12, but here the distinction is made between wave energy propagating upward and downward. Signed wavenumbers indicate upward and downward propagating u, w, respectively. The upper row shows energy transfers involving upward propagating shear U_z^+, while the lower row corresponds to U_z^-. A wider variety of wavenumber triads can be seen, relative to the unsigned version of Fig. 3.12. Some energy transfers involve u, w with opposite-sign propagation.

Energy transfer rate ε_* by frequency octave

As before, the Farfield time series are divided into octave frequency bands and the triple products corresponding to the energy transfer rate ε_* and the correlation r_3 are computed. Profiles of energy transfers in the Farfield are presented in Figure 3.14, along with error estimates (3.17). These should be compared with the Nearfield profiles in Figure 3.10.

Farfield energy transfers are generally weighted toward the surface, presumably where wind-generated D_1 waves are largest. This contrasts with the Nearfield, where ε_* is largest at depths where PSI-generated D_1 shears are large, below 500 m. However, a large peak is seen near 280 m depth in the Farfield D_{64} band. This region of elevated energy transfer represents the largest values of ϵ_* observed in the Farfield. Peak transfer rates are near 2×10^{-8} W kg^{-1}, or about 3 times smaller than in the Nearfield. As before, energy transfers grow steadily with frequency, but in the Farfield, ε_* does not stand out from $\varepsilon_{\rm err}$ until the D_{16} frequency band, whereas in the Nearfield, ε_* appears significant in all bands.

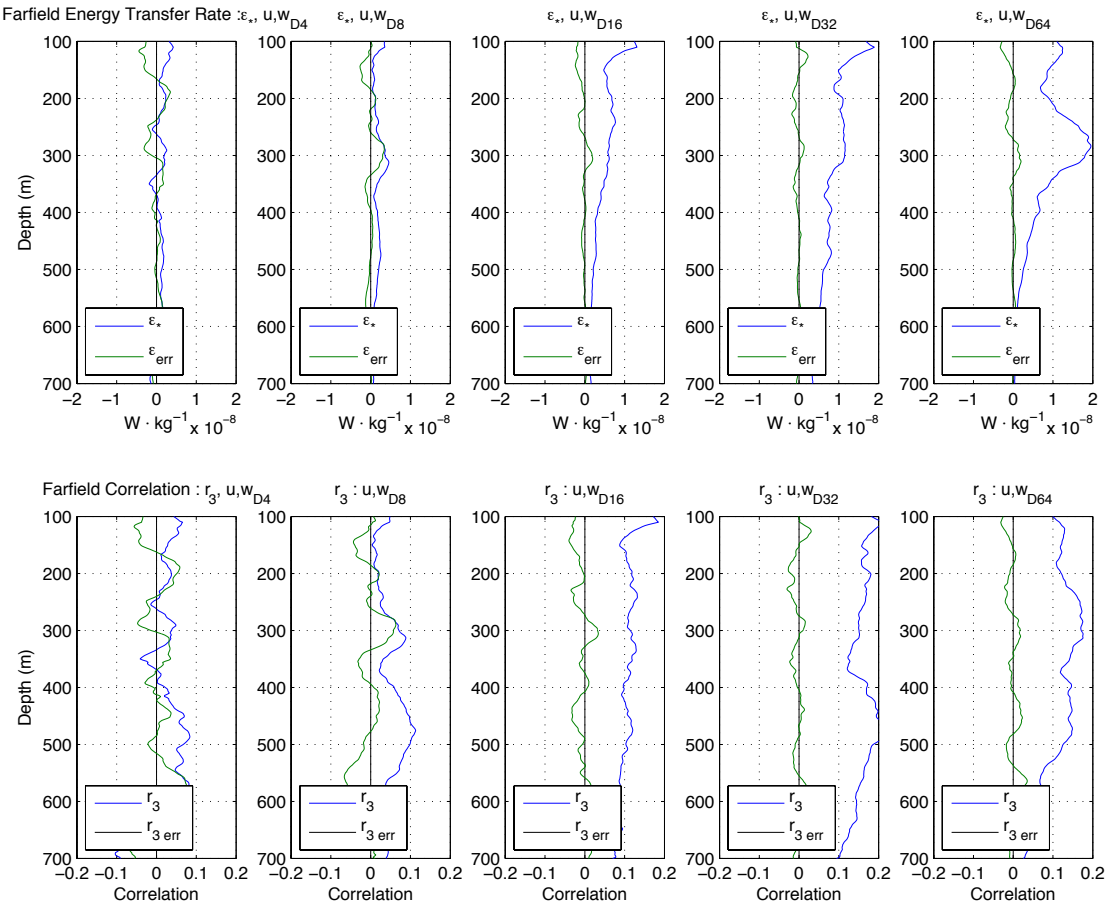

Figure 3.14: Farfield: Energy Transfer Profiles. As in Fig. 3.14, but for the Farfield. Above) Energy transfer rates $\varepsilon_* = -\langle uwU_z + vwV_z \rangle$ by frequency octave bin, as functions of depth. Error estimates (3.17) are plotted in green for reference. Energy transfers appear significant in bands from D_{16} to D_{64}. Maximum values of ε_* are biased toward the surface, expect for a peak near 280 m in the D_{64} band. Peak values are near 2×10^{-8} W kg^{-1}, or about 3 times smaller than in the Nearfield. Below) Stress-shear correlations $r_3(z)$ (3.6), as functions of depth. Unlike the Nearfield case, $r_3(z)$ does not resemble ϵ_*, and holds relatively steady through a broad range of depths. As before, error estimates are plotted in green.

Also unlike the Nearfield case, correlations in the Farfield do not mirror the energy transfer rate. Instead, $r_3(z)$ holds relatively steady through a broad range of depths. A possible explanation for this difference is that the Farfield is relatively "quiet" with respect to other nonlinear processes, while the interaction is only detectable above other nonlinear processes in the Nearfield when the energy transfer rate is large.

Depth-averaged energy transfer rates by octave, shown in 3.15, are 3–4 times smaller in the Farfield and are slightly more skewed toward high frequencies than in the Nearfield. ε_* nearly doubles with each octave, suggesting that the energy transfer density is nearly constant with linear frequency. A cutoff is reached between D_{32} and D_{64} as in the Nearfield.

Although the profiles of r_3 and ε_* in Fig 3.14 appear quite different, their distributions by frequency are remarkably similar, as seen in the lower panel of Figure 3.15.

Energy transfer rate ε_* by wavenumber octave

In the frequency domain, the energy transfers in the Nearfield and Farfield locations appear relatively similar. It remains to show whether the widely separated spatial scales of high frequency w and u seen in the Nearfield are also seen in the Farfield. Energy transfers by wavenumber octave are shown in Figure 3.16. As in the Nearfield (Fig. 3.12), the longest-wavelength w waves are the most strongly interacting. However, the u-wavelengths which interact with the long w waves are even shorter, at about 50 m, than in the Nearfield. The suggestion is that shorter u waves are involved simply because the shear scales in the Farfield include shorter wavelengths than the dominant 100 m scale found in the Nearfield.

Farfield energy transfers are also separated for upward-downward propagation. The signed wavenumber estimates are presented in Figure 3.17. Less new information is gained here than in the Nearfield. As before, a somewhat wider spread of resonant frequencies are apparent in isolated quadrants, and energy transfers are seen involving u, w pairs with opposite-sign vertical propagation. However, no significant biases in upward vs. downward propagation of u, w or U_z are apparent.

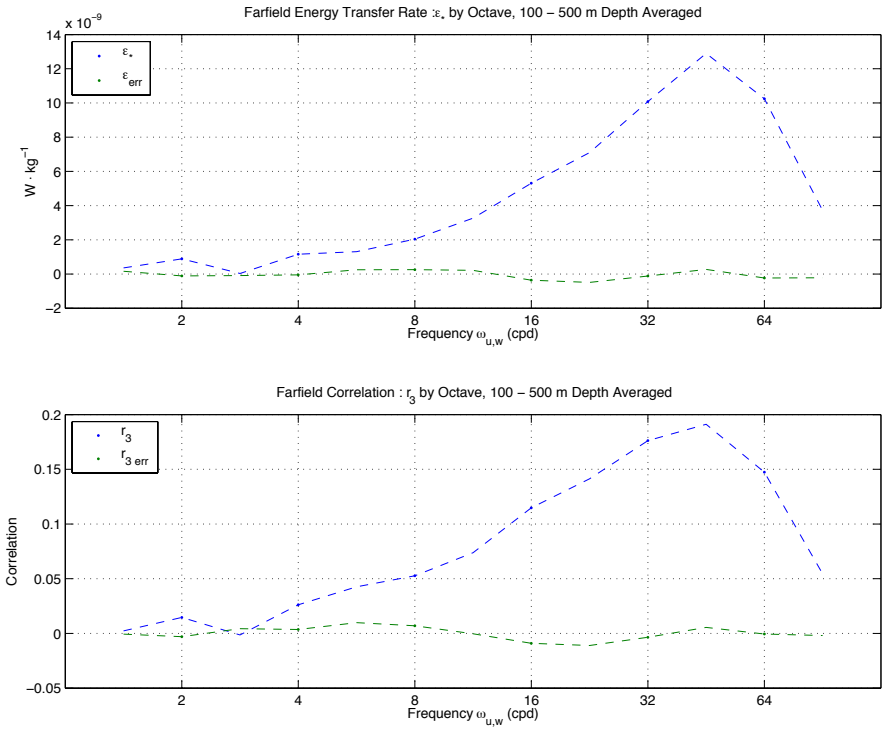

Figure 3.15: Farfield: Depth-Averaged Energy Transfers by Octave. As in Fig. 3.15, but in the Farfield. Above) Energy transfer rates $\varepsilon_* = -\langle uwU_z + vwV_z \rangle$ by frequency octave bin, depth-averaged. Plotted points are depth averages of the energy transfer profiles shown in Fig. 3.14. Dotted lines also pass through a set of points computed for intermediate octave bands. Error estimates (3.17) are plotted in green. Below) Stress-shear correlations $r_3(z)$ (3.6) by octave, depth-averaged. Although profiles of $r_3(z)$ do not resemble $\varepsilon_*(z)$ (Fig. 3.15), their depth averages have a similar frequency distribution.

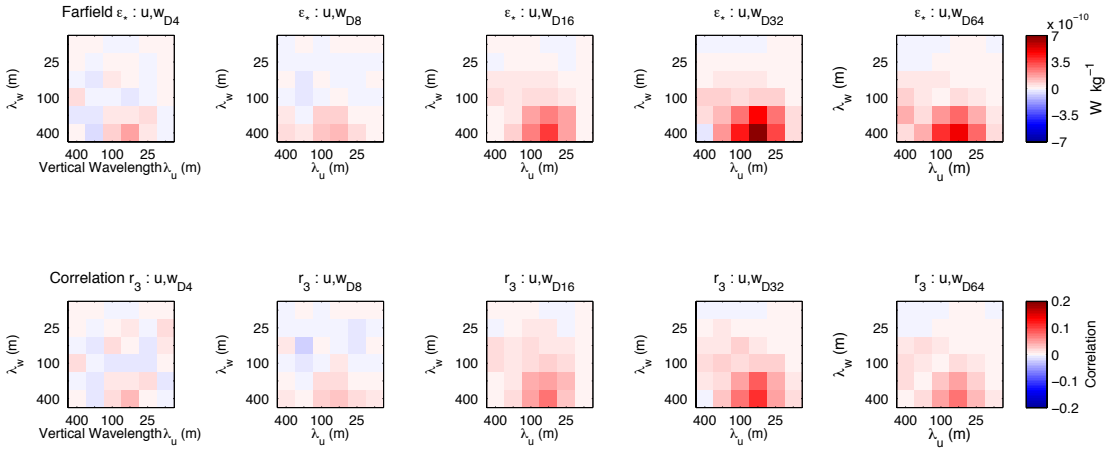

Figure 3.16: Farfield: Energy transfer rate ε_* by wavenumber octave. As in Fig. 3.12, but for the Farfield. As in the Nearfield, the wavenumber resonance is concentrated around the longest wavelengths in w, but a somewhat shorter-wavelength u of about 50 m interacts with the long w waves.

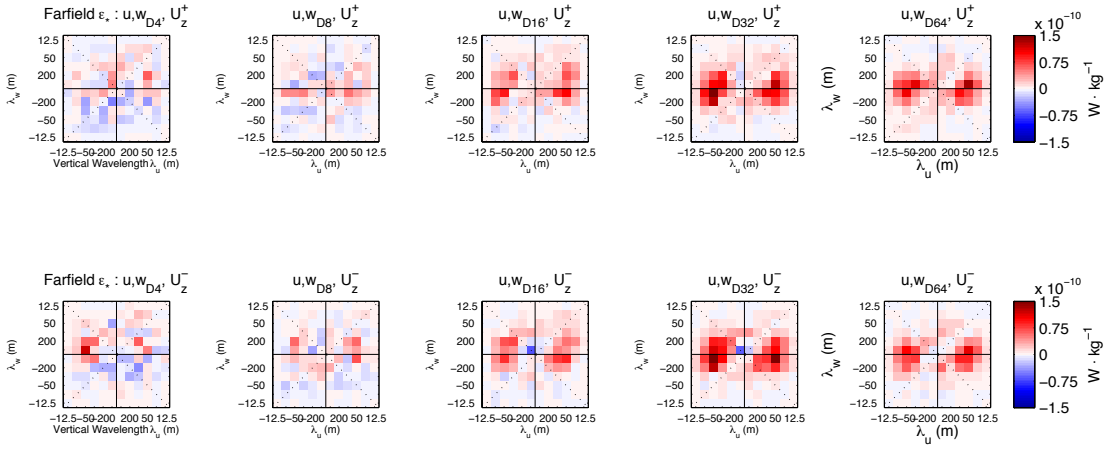

Figure 3.17: Farfield: Energy transfer rate ε_* by wavenumber octave. As in Fig. 3.13, but for the Farfield. Signed wavenumbers indicate upward and downward propagating u, w, respectively. The upper row shows energy transfers involving upward propagating shear U_z^+, while the lower row corresponds to U_z^-.

The frequency and wavenumber resonances seem to show a similar interaction occurring in the Farfield as in the Nearfield. Both involve pairs of u, w waves with similar frequency but dissimilar vertical scales interacting with the low frequency shear field. The scale difference between the long w and the shorter u is even more pronounced in the Farfield than in the Nearfield. In both settings, the interaction seems clearly different from classical Induced Diffusion. The observations also do not support the eikonal model of small-scale test waves being refracted in a background shear field.

3.4 Discussion

If the interaction is neither Induced Diffusion nor eikonal, then what is it? An interesting question is whether weakly nonlinear interactions are needed at all to explain the energy transfers observed in the upper water column in the Nearfield. Klymak et al. [2008] attributed much of the Nearfield dissipation below 400 m due to immediate breaking of the internal tide rather than to internal wave cascade processes. Perhaps a strongly nonlinear mechanism, such as shear instability in the D_1 band, is associated with the apparent energy transfers above 400 m as well.

To examine the shear instability hypothesis, a gradient Richardson number $\mathrm{Ri}_6 = \langle N^2 \rangle / S_6^2$ is calculated using the D_1 shears down to 6 m scale and a cruise-averaged stratification $\bar{N}(z)$. This method amounts to a rescaling of the D_1 shear fields (Figs. 3.4, 3.6). The results, presented in Figure 3.18, are presented on a $\log_2$ scale which is centered around a canonical Richardson number of 1/4. In the Nearfield, shears often reach a Richardson number of unity but are rarely seen to approach 1/4, except at the peaks of the large PSI inertial packets around days 270 and 284. However, the largest energy transfers in the Nearfield are not observed at peak shear, but during the overlap between the fading spring tide and the growing PSI shears. Depth-time correlations between ϵ_* and critical Ri_6 (not shown) find no significant statistical relationship between the two.

In the Farfield, the Ri tend to be about 4 times larger, hence almost never reach 1/4. However, a similar pattern of energy transfers is observed at both

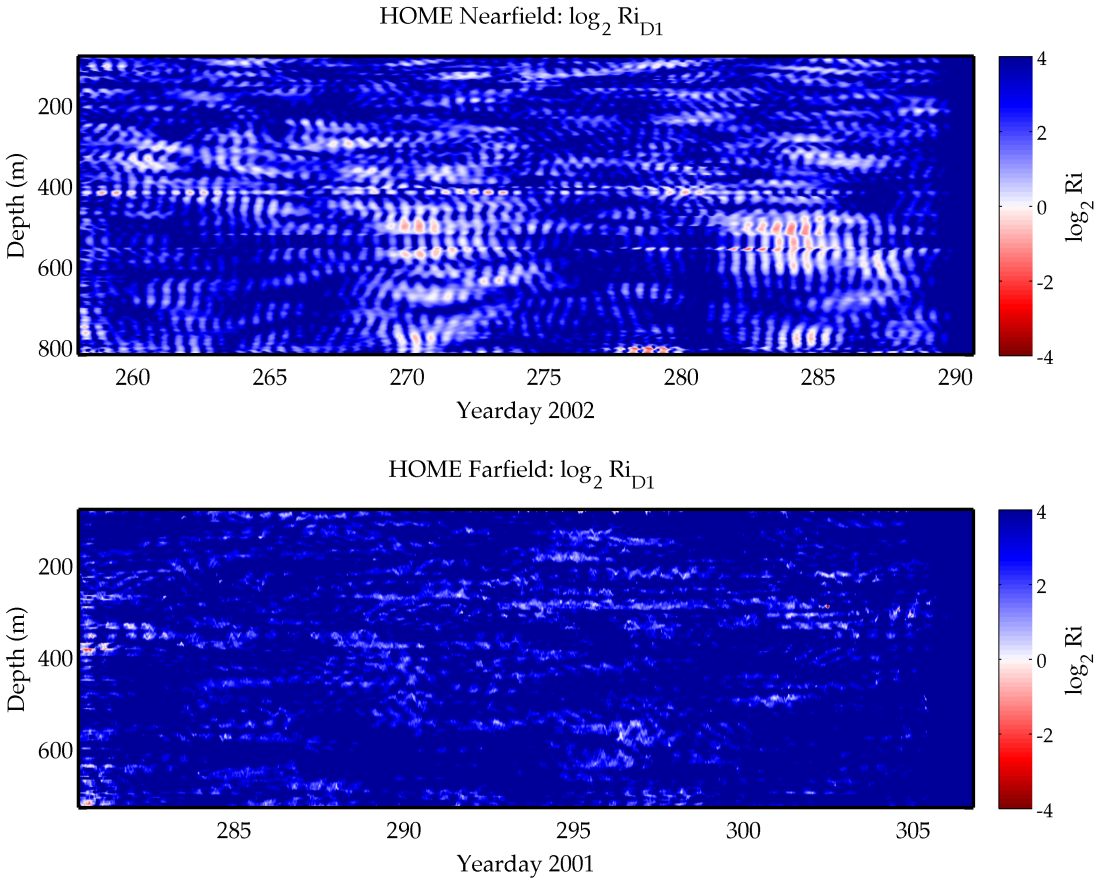

Figure 3.18: Richardson number associated with D_1 shears. Results are presented on a $\log_2$ scale, so that the critical Ri cutoff of 1/4 appears as -2 on this scale. In the Nearfield (top), the shears are potentially unstable only at the peak of the PSI subharmonics near days 270 and 294 and around 500–550 m. This contrasts with the peak times and depths of ε_*, which peaks between the spring tide and the maximum of the PSI shears around a depth of 300 m. In the Farfield (bottom), the shears are essentially stable.

locations. The presence of energy transfers in the Farfield, combined with the lack of time correlation in the Nearfield make it unlikely that shear instabilities explain the observations.

Resonant triads of interacting waves remain a viable explanation, so long as they are not Induced Diffusion. The wavenumber-frequency analysis of Section 2.5 show that the energy transfers take place between distinct frequencies and vertical wavelengths. Energy transfer rates also reflect features of the internal wave field, e.g., the assymmetry of w with respect to upward-downward propagation at low frequencies. Finally, distributions of ε_* by frequency octave, Figs. 3.11, 3.15, show a distinct Vaïsala cutoff in both the Nearfield and Farfield. These findings support a picture of interacting waves.

3.4.1 Energy transfers compared to turbulent dissipation

Aside from a qualitative description of the energy transfers captured by ε_*, a separate and potentially more important question is whether the energy transfers are likely to be a significant source, relative to energy removal, for the internal wave field. To address this question, ε_* is compared to independent estimates of the turbulent dissipation rate ε.

Dissipation estimates are available from several sites in HOME, as measured by a combination of tethered profilers and towed instruments. Directly over the ridge, Klymak et al. [2006] found a mean vertical diffusivity $K_\rho > 10^{-3}$ m^2 s^{-1}. The magnitude of the energy transfers ε_* in the Nearfield are of order 1×10^{-7} W kg^{-1}, which can be converted to a diffusivity using the relationship due to Osborn [1980],

$$K_\rho = \Gamma \frac{\varepsilon_*}{\langle N^2 \rangle}, \tag{3.18}$$

where $\Gamma \approx 0.2$ and a reference value of $(0.0031 \text{ s}^{-1})^2$ is used for $\langle N^2 \rangle$. This yields a value for $K_\rho \sim 2 \times 10^{-3}$ m^2 s^{-1}, provided that all of the energy which is transferred to high frequencies subsequently breaks.

The agreement in magnitude between ε_* and ε is encouraging. However, estimates of ε are known to vary by several orders of magnitude with increasing distance from the ridge crest. To gain a better estimate of the true dissipation rate

near the *FLIP* locations, an attempt is made to estimate the turbulent dissipation rate by an overturns analysis of the *FLIP* CTD data.

The method used is described in Dillon [1982]: a Thorpe displacement d' is assigned to each sample in the density profile, where d' is defined as the difference of the sample's position in a sorted density profile from the position at which it was measured. Where the water column is already statically stable, L_{T} is identically zero. The rms displacement defines the Thorpe scale $L_{\mathrm{T}} = \langle d' \rangle$. L_{T}, in turn, is a proxy for the Ozmidov scale $L_{\mathrm{O}} = (\varepsilon/N^3)^{1/2} \approx L_{\mathrm{T}}$.

Profiles of the Nearfield time-averaged dissipation rate ε inferred from Thorpe scales are plotted together with the energy transfer rate ε_* in Figure 3.19. ε_* and ε have the order of magnitude, but ε_* is relatively steady with depth, while ε increases steadily with depth, matching and eventually surpassing ε_* between 500 and 600 m depth. It is unknown why the energy transfer rate is larger than the dissipation rate. Much of the turbulent mixing in the Nearfield has been attributed to an apparently unrelated process, that of direct breaking of the internal tide near the sloping bottom [Klymak et al., 2008]. Depth-time correlations between ε_* and ε show no significant link, so it seems likely that high frequency motions associated with the energy transfers propagate away before contributing to breaking and mixing.

A speculative hypothesis for explaining for the excess in ε_* is that low frequency shears near the generation site are unusually out-of-balance with respect to the high frequency region of the internal wave spectrum. This might be a result of local generation of D_1 shears by PSI. In this scenario, the Nearfield represents a net source for high frequency internal waves in a broader region surrounding the ridge.

The picture is somewhat different in the Farfield, as shown in Figure 3.20. Throughout the water column, the profiles agree closely, within a factor of about 3. The dissipation estimate has a step discontinuity around 400 m, near the depths of best agreement in the upper water column, due to a mismatch between the upper and lower CTDs. The lower CTD does not appear to be resolving all the overturns in the Farfield, but due to substantial changes in the T-S relationship during

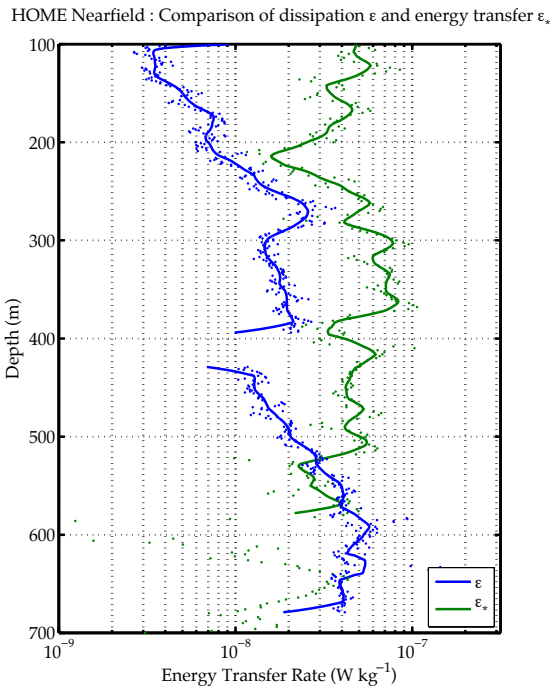

Figure 3.19: Nearfield: Comparison of turbulent dissipation rate ε and energy transfer rate ε_*. The turbulent dissipation rate ε is estimated from density overturns using Thorpe scales. The profiles generally agree within an order of magnitude, but the energy transfer rate ε_* holds relatively steady, while ε increases with depth until it surpasses ε_* between 500 and 600 m depth. The large ε values in the lower several hundred meters are associated with strongly nonlinear wave breaking.

the cruise, a conservative approach is taken here to identifying "true" overturns. Nevertheless, the closeness of the profiles is remarkable, especially since the Farfield is taken to be the more typical of the two sites.

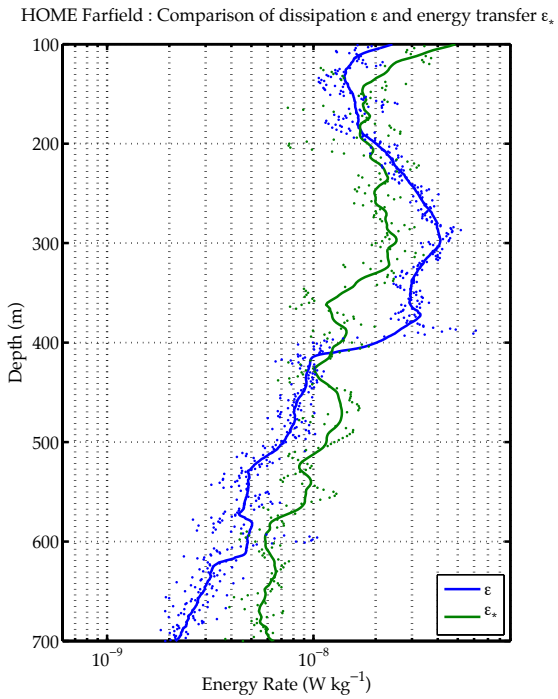

Figure 3.20: Farfield: Comparison of turbulent dissipation rate ε and energy transfer rate ε_*. As in Fig. 3.19 but for the Farfield. The turbulent dissipation rate ε is estimated from density overturns using Thorpe scales. The profiles agree within a factor of 3 in the upper 400 m. The lower CTD (below 400 m) does not seem to resolve all the overturns, resulting in a discontinuity at the switchover depth near 400 m.

3.5 Summary

Observations taken from both the HOME Nearfield and Farfield components find shears concentrated at low frequencies along with horizontal and vertical velocities spanning a broad range of frequencies up to the Vaïsala cutoff. In the Nearfield, the low frequency shears, which are associated with PSI of the semidiurnal tide, have a well-defined dominant vertical scale of about 100 m. Peak amplitudes appear in the lower half of the profiling column. A fortnightly cycle is

apparent and lags the semidiurnal fortnightly cycle by several days. Meanwhile, the high frequencies have largest amplitudes during spring tides. The Farfield shears are more typical, showing a range of vertical scales. High frequency motions are also observed, but have no obvious fortnightly cycle.

A modified stress-shear correlation, in which the shears are allowed to vary slowly at low frequency, finds that energy is transferred from the low frequency shear background to high frequencies. Energy transfer rates are of order 1×10^{-7} W kg^{-1} in the Nearfield and are about 3 times smaller in the Farfield.

The interacting frequencies are identified using energy bispectra, which express the stress-shear correlation a function of paired frequencies (ω_u, ω_w). Bicoherences suggest that significant energy transfers are confined to u, w high frequencies which differ by a small frequency contained in the D_1 band. Analysis of total energy transfers by frequency octave bands finds that the interaction remains positive and relatively steady with increasing frequency, up to a cutoff near the Vaïsala frequency.

While the frequency resonances are compatible with a classical Induced Diffusion triad, the wavenumber resonances are not. Energy transfers are detected involving distinct high frequency pairs, in which w typically has very long vertical scales of about 400 m, while u has much shorter scales of about 100 m in the Nearfield and 50 m in the Farfield. The difference in u scales may be a result of shorter shear scales available for interaction in the Farfield. In both cases, the w scales are much longer than the shear scales, contradicting the scale separation assumed by eikonal models of high-frequency–low-frequency interaction.

The energy transfer rates found here are placed in perspective by comparing them to estimates of the true turbulence dissipation rate ε. Surprising agreement is found between the energy transfers to high frequency ε_* and dissipation ε inferred from Thorpe scale analysis of overturns. The suggestion is that ε_* may be a significant source of energy to waves which eventually break and trigger turbulent mixing in the ocean.

If the energy transfers identified in this study can be demonstrated in other data sets, then one might imagine a scheme for estimating the decay of low-

frequency shears, whether due to PSI or more generally by wind generation, by modeling the interaction as a "wave diffusivity" for the background shears. At the same time, energy transfer rate may also prove valuable as an additional proxy for turbulent mixing, based on the close agreement, especially in the Farfield, between ε_* and ε estimated from overturns.

A future goal is to gain a better understanding of the dynamics behind the nonlinear interaction. A major unanswered question is why this specific configuration of waves, particularly involving the very long-wavelength w waves, are preferred (or detected) in a nonlinear energy transfer. The assumptions behind the triple correlation method should also be carefully examined. Further analysis of the HOME dataset, particularly with refined spectral techniques, may yield insight into these problems.

Chapter 4

Summary

Observations were made from the Research Platform (R/P) *FLIP* at two locations in 2001–2002, during the Hawaii Ocean Mixing Experiment (HOME). In the HOME Nearfield component, *FLIP* was moored on the southwest shoulder of Kaena Ridge, one of the most active internal tidal generation sites identified during HOME. Semidiurnal tidal energy emanating upward from the ridge and energetic diurnal shears propagating both upward and downward were observed. During the Farfield deployment, *FLIP* was positioned approximately 430 km to the southwest of the Ridge, in the approximate path of a propagating semidiurnal tidal beam .

A combination of profiling CTDs and the *Deep-8* sonar recorded density information and horizontal velocities down to approximately 800 m depth during both deployments. More than 9000 profiles were taken at 4-minute intervals during the six-week Farfield component, and more than 11000 profiles were recorded in the Nearfield. The 2-d data gathered aboard *FLIP* provided a unique opportunity to apply wavenumber-frequency analysis.

PSI of the semidiurnal internal tide

The first investigation attempted to observe Parametric Subharmonic Instability (PSI) of the internal tide. Bispectral analysis was introduced as a method for demonstrating and establishing the significance of phase coupling between the low mode internal tide and diurnal waves observed near the ridge. Here a cross-

bispectrum was used to maximize the signal-to-noise of the measurement: the diurnal waves were most clearly detected in the shears, while the low-mode tide was emphasized by vertical velocities. Due to the prediction of PSI that an interaction could take place between pairs of diurnal waves and the tide, cross-bispectra were computed between two shear signals and one vertical velocity.

To further test the wavenumber resonance predicted by PSI, upward-propagating and downward-propagating diurnal waves were separated using a 2-d Fourier transform method. Bicoherences involving one upward-propagating shear frequency and one downward-propagating shear frequency were significantly greater than those for the unseparated fields. Configurations with two upward or two downward shears, which could not fulfill the vertical wavenumber resonance condition, were not statistically distinguishable from zero bicoherence.

Depth-time correlations were computed, corresponding to the bicoherences between the semidiurnal and diurnal bands only. Regions of uniformly positive correlation indicated times and locations of active energy transfer. The PSI subharmonics were shown to be strongest between 500 and 600 m, with a peak amplitude lagging the spring tide by about 4–7 days as predicted by theory.

Due to the apparent group structure of subharmonic packets, two interpretations of significant bicoherence were compared: one using the characteristic time and space scales of the subharmonic groups, and the other using the more traditional scales of individual subharmonic wavelengths and periods. The group scales predicted a much stricter threshold for significance. Monte Carlo simulations showed that group scales were a good predictor of empirical bicoherence distributions, while wave scales drastically underpredicted thresholds associated with significant bicoherences. Unseparated cross-bicoherences were only marginally significant under the stricter requirement, but the up-down separated bicoherences remained clearly significant. The bicoherence measurements, combined with the implied relationship between the wavevectors and subharmonic growth rates, strongly supported the hypothesis that PSI of the internal tide was transferring energy to the subharmonic waves in the Nearfield of Kaena Ridge.

Energy transfer from low to high frequencies

In the second part of the thesis, energy transfers from low-frequency waves due to high frequency fluctuations were investigated in both the HOME Nearfield and Farfield data. The monochromatic PSI waves in the Nearfield provided a clearly identifiable starting point for the investigation; meanwhile, the Farfield was taken as an example of a much more "typical" open-ocean environment.

The stress-shear triple correlation $-\left\langle u_i w \frac{dU_i}{dz} \right\rangle$, analogous to the production term in turbulence theory, was developed as a method for quantifying energy transfers in the (assumed) quasi-steady wavefield. To identify interacting frequencies, the correlation was expressed in energy bispectral form. Significant interactions were found only near the main frequency diagonal in bispectral space, implying that energy transfers were confined to high frequency waves with similar frequency. Further frequency analysis found significant energy transfers involved a broad range of frequencies, reaching to an approximate Vaïsala cutoff before rolling off.

While the frequency resonances were compatible with both the Induced Diffusion and eikonal models of nonlinear interaction, wavenumber analysis showed that neither model was supported. While a variety of resonant triads were found in signed wavenumber space, three findings conflicted with the expectations of the theory: 1) interactions tended to favor very long scales in w, in contradiction to the scale separation assumption; 2) interacting u_i and w waves remained distinct in the limit of high frequency rather than collapsing; and 3) wave triads involving two upward or two downward propagating high frequency waves were observed.

Nevertheless, energy transfer rates of order 1×10^{-7} W kg^{-1} in the Nearfield and about 30% that in the Farfield, appeared significant from a measurement standpoint. To place those numbers in perspective in terms of significance to the internal wave field and mixing, a set of turbulence dissipation estimates were also computed for both locations. These estimates were formed by an analysis of overturns to determine Thorpe scales. While the energy transfer found in the Nearfield was somewhat higher than the turbulence measurement, they still agreed to within an order of magnitude throughout the water column. A possible explanation for

this discrepancy may be that the excess of subharmonic waves generated by PSI in the Nearfield lead to unusually high energy transfers relative to other locations, but that the high frequency waves carry some the energy away to "leaner" regions before breaking. In the Farfield, the agreement between energy transfer rate and dissipation was much better, within a factor of 3 at all depths.

Similar analyses should be carried out with other data sets to verify that these relationships hold. If they do, these high frequency transfers may prove useful as a proxy for internal wave energy available to turbulent mixing. However, it remains an open question: what selects these triads for energy transfer? A priority for future research should be to investigate the dynamical picture behind the energy transfers found in this investigation.

References

M. Alford, J. MacKinnon, Z. Zhao, R. Pinkel, J. Klymak, and T. Peacock. Internal waves across the Pacific. *Geophys Res Lett*, 34(24):L24601, Jan 2007. doi: 10.1029/2007GL031566.

D. Benney and P. Saffman. Nonlinear interactions of random waves in a dispersive medium. *Proceedings of the Royal Society of London. Series A, Mathematical and Physical Sciences*, pages 301–320, 1966.

F. Bretherton. Resonant interactions between waves - the case of discrete oscillations. *J Fluid Mech*, 20(3):457–479, Jan 1964.

W. S. Broecker. The biggest chill. *Nat. Hist. Mag.*, 97:74–82, 1987.

W. S. Broecker. The great ocean conveyor. *Oceanography*, 4(2):79–89, 1991.

D. Broutman and W. Young. On the interaction of small-scale oceanic internal waves with near-inertial waves. *Journal of Fluid Mechanics*, 166:341–58, 1986.

G. Carter and M. Gregg. Persistent near-diurnal internal waves observed above a site of M2 barotropic-to-baroclinic conversion. *Journal of Physical Oceanography*, 36(6):1136–1147, 2006.

T. M. Dillon. Vertical overturns: a comparison of thorpe and ozmidov length scales. *Journal of Geophysical Research*, 87(C12):9601–9613, November 1982.

T. Duda and D. Jacobs. Stress/shear correlation: Internal wave/wave interaction and energy flux in the upper ocean. *Geophys Res Lett*, 25(11):1919–1922, Jan 1998.

G. Egbert and R. Ray. Significant dissipation of tidal energy in the deep ocean inferred from satellite altimeter data. *Nature*, 405(6788):775–778, 2000.

G. Egbert and R. Ray. Estimates of M2 tidal energy dissipation from TOPEX/Poseidon altimeter data. *Journal of Geophysical Research*, 106(22): 475–22, 2001.

G. D. Egbert. Tidal data inversion: interpolation and inference. *Progress In Oceanography*, 40(1-4):53–80, 1997.

S. Elgar and R. Guza. Shoaling gravity waves: Comparisons between field observations, linear theory, and a nonlinear model. *Journal of Fluid Mechanics*, 158: 47–70, 1985a.

S. Elgar and R. Guza. Observations of bispectra of shoaling surface gravity waves. *Journal of Fluid Mechanics*, 161:425–48, 1985b.

S. Elgar and R. Guza. Statistics of bicoherence. *IEEE T Acoust Speech*, 36(10): 1667–1668, October 1988.

S. Elgar, T. Herbers, V. Chandran, and R. Guza. Higher-order spectral-analysis of nonlinear ocean surface gravity-waves. *J Geophys Res-Oceans*, 100(C3):4977–4983, Jan 1995.

E. E. Frajka-Williams, E. L. Kunze, and J. A. MacKinnon. Bispectra of internal tides and parametric subharmonic instability. Master's thesis, University of Washington, Nov 2006.

A. Gargett and G. Holloway. Dissipation and diffusion by internal wave breaking. *Journal of Marine Research*, 42(1):15–27, 1984.

C. Garrett and W. Munk. Oceanic mixing by breaking internal waves. *Deep Sea Research and Oceanographic Abstracts*, Jan 1972.

A. E. Gill. *Atmosphere-ocean dynamics*. Academic Press, New York, 1982.

M. C. Gregg. Diapycnal mixing in the thermocline – a review. *Journal of Geophysical Research-Oceans*, 92(C5):5249–5286, May 1987.

K. Hasselmann. On the non-linear energy transfer in a gravity-wave spectrum .1. general theory. *J Fluid Mech*, 12(4):481–500, Jan 1962.

K. Hasselmann. On the non-linear energy transfer in a gravity wave spectrum .2. conservation theorems - wave-particle analogy - irreversibility. *J Fluid Mech*, 15 (2):273–281, Jan 1963a.

K. Hasselmann. On the non-linear energy transfer in a gravity-wave spectrum .3. evaluation of the energy flux and swell-sea interaction for a neumann spectrum. *J Fluid Mech*, 15(3):385–398, Jan 1963b.

K. Hasselmann. Feynman diagrams and interaction rules of wave-wave scattering processes. *Rev Geophys*, 4(1):1–&, Jan 1966.

F. Henyey and N. Pomphrey. Eikonal description of internal wave interactions - a non-diffusive picture of induced diffusion. *Dynam Atmos Oceans*, 7(4):189–219, Jan 1983.

F. Henyey, J. Wright, and S. Flatté. Energy and action flow through the internal wave field - an eikonal approach. *J Geophys Res-Oceans*, 91(C7):8487–8495, Jan 1986.

T. Hibiya, Y. Niwa, and K. Fujiwara. Numerical experiments of nonlinear energy transfer within the oceanic internal wave spectrum. *J Geophys Res-Oceans*, 103 (C9):18715–18722, Jan 1998.

T. Hibiya, M. Nagasawa, and Y. Niwa. Nonlinear energy transfer within the oceanic internal wave spectrum at mid and high latitudes. *Journal of Geophysical Research-Oceans*, 107(C11):3207, 2002.

Y. Kim and E. Powers. Digital bispectral analysis and its applications to non-linear wave interactions. *IEEE T Plasma Sci*, 7(2):120–131, Jan 1979.

J. Klymak, J. Moum, J. Nash, E. Kunze, J. Girton, G. Carter, C. Lee, T. Sanford, and M. Gregg. An estimate of tidal energy lost to turbulence at the hawaiian ridge. *Journal of Physical Oceanography*, 36(6):1148–1164, 2006.

J. Klymak, R. Pinkel, and L. Rainville. Direct breaking of the internal tide near topography: Kaena ridge, hawaii. *Journal of Physical Oceanography*, 38(2): 380–399, 2008.

J. A. MacKinnon and K. B. Winters. Subtropical catastrophe: Significant loss of low-mode tidal energy at 28.9. *Geophysical Research Letters*, 32(15):L15605, 2005.

C. H. McComas and F. Bretherton. Resonant interaction of oceanic internal waves. *J Geophys Res-Oc Atm*, 82(9):1367–1412, Jan 1977.

C. H. McComas and M. Briscoe. Bispectra of internal waves. *J Fluid Mech*, 97: 205–213, Jan 1980.

C. H. McComas and P. Müller. Time scales of resonant interactions among oceanic internal waves. *Journal of Physical Oceanography*, 11(2):139–147, 1981a.

C. H. McComas and P. Müller. The dynamic balance of internal waves. *Journal of Physical Oceanography*, 11(7):970–986, 1981b.

P. Müller and D. Olbers. On the dynamics of internal waves in the deep ocean. *J Geophys Res-Oc Atm*, 80(27):3848–3860, Jan 1975.

P. Müller, G. Holloway, and F. Henyey. Nonlinear interactions among internal gravity waves (paper 6r0117). *Reviews of Geophysics*, 24(3):493–536, August 1986.

W. Munk. Abyssal recipes. *Deep Sea Research and Oceanographic Abstracts*, Jan 1966.

W. Munk. Internal wave spectra at the buoyant and inertial frequencies. *Journal of Physical Oceanography*, 10(11):1718–1728, 1980.

W. Munk and C. Wunsch. Abyssal recipes II: energetics of tidal and wind mixing. *Deep-Sea Research Part I*, 45(12):1977–2010, 1998.

S. Neshyba and E. J. C. Sobey. Vertical cross coherence and cross bispectra between internal waves measured in a multiple-layered ocean. *Journal of Geophysical Research*, 80(9):1152–1162, March 1975.

D. Olbers. Nonlinear energy transfer and the energy balance of the internal wave field in the deep ocean. *J. Fluid Mech*, 74:375–399, 1976.

D. Olbers and N. Pomphrey. Disqualifying two candidates for the energy balance of the oceanic internal wave field. *Journal of Physical Oceanography*, 11:1423–1425, Oct 1981.

T. R. Osborn. Estimates of the local rate of vertical diffusion from dissipation measurements. *Journal of Physical Oceanography*, 10(1):83–89, 1980.

O. M. Phillips. On the dynamics of unsteady gravity waves of finite amplitude. *Journal of Fluid Mechanics*, 9:193–217, 1960.

O. M. Phillips. On the dynamics of unsteady gravity waves of finite amplitude. part 2. local properties of a random wave field. *Journal of Fluid Mechanics*, 11: 143–155, 1961.

R. Pinkel. Advection, phase distortion, and the frequency spectrum of finescale fields in the sea. *Journal of Physical Oceanography*, 38(2):291–313, Jan 2008. doi: 10.1175/2007JP03559.1.

R. Pinkel, L. Rainville, and J. M. Klymak. Gravity wave momentum fluxes in the HOME Nearfield experiment. 2010.

K. Polzin, J. Toole, J. Ledwell, and R. Schmitt. Spatial variability of turbulent mixing in the abyssal ocean. *Science*, 276(5309):93, 1997.

S. Rahmstorf. Thermohaline circulation: the current climate. *Nature*, 421:699, Feb 2003.

L. Rainville and R. Pinkel. Baroclinic energy flux at the Hawaiian Ridge: Observations from the R/P FLIP. *Journal of Physical Oceanography*, 36(6):1104–1122, 2006.

R. Ray and G. Mitchum. Surface manifestation of internal tides in the deep ocean: observations from altimetry and island gauges. *Progress in Oceanography*, 40 (1-4):135–162, 1997.

D. L. Rudnick, T. J. Boyd, R. E. Brainard, G. S. Carter, G. D. Egbert, M. C. Gregg, P. E. Holloway, J. M. Klymak, E. Kunze, C. M. Lee, M. D. Levine, D. S. Luther, J. P. Martin, M. A. Merrifield, J. N. Moum, J. D. Nash, R. Pinkel, L. Rainville, and T. B. Sanford. From tides to mixing along the Hawaiian Ridge. *Science*, 301(5631):355–357, 2003.

L. St. Laurent and C. Garrett. The role of internal tides in mixing the deep ocean. *Journal of Physical Oceanography*, 32(10):2882–2899, 2002.

O. M. Sun and R. Pinkel. Energy transfer from the semidiurnal internal tide to near-diurnal motions at Kaena Ridge, Hawaii. 2011.

H. Tennekes and J. L. Lumley. *A first course in turbulence.* The MIT Press, Cambridge, MA, 1972.

C. Wunsch. What is the thermohaline circulation? *Science*, 298:1179–1180, November 2002.

C. Wunsch and R. Ferrari. Vertical mixing, energy, and the general circulation of the oceans. *Annu. Rev. Fluid Mech.*, 36:281–314, 2004.

W. R. Young, Y.-K. Tsang, and N. J. Balmforth. Near-inertial parametric subharmonic instability. *J Fluid Mech*, 607:1–25, 2008.